The Design and Implementation of a Simulator for Multistatic Radar Systems

Marc Brooker
BSc (Eng) UCT

A thesis submitted to the Department of Electrical Engineering, University of Cape Town, in fulfilment of the requirements for the degree of

Doctor of Philosophy

at the

University of Cape Town

June 2008

"The purpose of computing is insight, not numbers."

Richard W. Hamming

Declaration

This report and the project on which it is based is entirely my own work.

I have used the IEEE convention for citation and referencing. Each contribution to, and quotation in, this report from the works of others has been attributed, cited and referenced.

I have not allowed, nor will allow, any other student to copy my work with the intention of passing it off as their own.

I acknowledge that plagiarism is wrong, and declare that this report, and the project on which it is based, is entirely my own work.

Marc Brooker

Abstract

This thesis presents the design and implementation of a signal level simulator supporting a wide variety of radar systems, and focusing on multistatic and netted radars. The simulator places few limits on the simulated system, and supports systems with arbitrary numbers of receivers, transmitters, and scatterers. Similarly, the simulator places no restrictions on the radar waveform to be simulated, and supports pulsed, continuous wave (CW) and carrier-free radar systems.

A flexible model is used to describe the radar system to be simulated, with the parameters of the radar hardware, the properties of scatterers and the layout of objects in the simulated environment specified in XML format. The development of the simulation model focused on balancing the requirements of flexibility and usability, ensuring that the model can be efficiently used to represent any type of radar system.

Oscillator phase noise is a limiting factor on the performance of some types of radar systems. The development of a model for the deterministic and static components of phase noise is presented. Based on this model, an algorithm for the efficient generation of synthetic phase noise sequences was developed, based on a multirate signal processing approach. This thesis presents this algorithm, and results of simulations of the effects of phase noise on synthetic aperture radar (SAR) and pulse-Doppler radar systems.

The FERS simulator, an implementation of the simulation model presented in this thesis, was developed in the C++ and Python programming languages. This simulator is able to perform real-time simulation of some common radar configurations on commodity PC hardware, taking advantage of multicore and multiprocessor machines. FERS has been released as open source software

under the GNU general public licence (GPL).

Validation of the simulator output was performed by comparison of simulation results with both theory and measurements. The simulator output was found to be accurate for a wide variety of radar systems, including netted pulse-Doppler, moving target indication (MTI) and synthetic aperture (SAR) radar systems.

Acknowledgements

I am extremely grateful for the advice and guidance of my supervisor, Professor Michael Inggs. Through sharing his expertise and extensive insight into the theory and practice of radar, Professor Inggs has earned my highest appreciation and made working on this project a extraordinarily fulfilling experience.

This work would not have been possible without the financial support of the SANDF, and the assistance of the CSIR Ledger program.

I would also like to thank the members of the Radar Remote Sensing Group (RRSG) for providing me with a stimulating and enjoyable research environment; Shaun Doughty, Stephan Sandenbergh and Sebastiaan Heunis for sharing some of the data that was used for the validation of FERS; and Regine Lord for protecting me from the university administration system. I am grateful for the advice provided to me by Professor Christopher Baker and Karl Woodbridge from University College London.

My parents, Chris and Elaine Brooker, have been especially supportive and patient.

Finally, I would like to thank Kate McWilliams for providing me with assistance, support, and inspiration.

Contents

List of Figures

List of Tables

List of Algorithms

Nomenclature

ADC Analogue to Digital Converter

AR Autoregressive

ARMA Autoregressive Moving Average

CW Continuous Wave

DAC Digital to Analogue Converter

DDS Direct Digital Synthesis

EW Electronic Warfare

FIR Finite Impulse Response

FM Frequency Modulation

GUI Graphical User Interface

IIR Infinite Impulse Response

ISLR Integrated Sidelobe Ratio

ISO International Organization for Standardization

LF Low Frequency

LNA Low Noise Amplifier

MTI Moving Target Indication

OCXO Oven Controlled Crystal Oscillator

PCL Passive Coherent Location

PCM Pulse Code Modulation

PM Phase Modulation

PRF Pulse Repetition Frequency

PRI Pulse Repetition Interval

PSD Power Spectral Density

PSL Peak Sidelobe Level

PSM Polarization Scattering Matrix

RCS Radar Cross Section

RF Radio Frequency

RRSG Radar Remote Sensing Group

SAR Synthetic Aperture Radar

SMP Symmetric Multiprocessing

STFT Short Time Fourier Transform

STP Standard Temperature and Pressure

T-R Transmit-Receive

TCXO Temperature Compensated Crystal Oscillator

TIE Time Interval Error

UCT University of Cape Town (South Africa)

Chapter 1

Introduction

1.1 Research Objectives

This thesis presents the development and validation of a simulator for netted and multistatic [11] radar systems. The key objectives of this research were to:

- Research and develop algorithms for the signal level simulation of radar systems. The algorithms required must support the simulation of systems with arbitrary numbers of receivers, transmitters and targets. Simulation algorithms must also efficiently support CW radar, wideband and carrier-free radar systems.
- Research and develop algorithms for the simulation of the effects of phase noise and jitter on radar systems, and the synthesis of phase noise matching measured oscillator parameters.
- Develop a complete simulator using the algorithms for radar simulation and clock simulation. Key requirements for the simulator include portability, ease of use, and applicability to a wide variety of radar simulation problems.
- Verify that the simulation results are accurate, within the bounds of the limitations of the simulation algorithms. Comparisons with both

measured data and theoretical expectations must be performed, and the differences between simulation results and expect results explained.

- Use the simulator to predict emergent behaviours not explicitly included in the simulation model.
- Demonstrate that large multistatic radar systems can be simulated, at the signal level, using low-cost computer hardware.

These objectives were identified as supporting the goal of developing an accurate and flexible signal level simulator for monostatic, multistatic and netted radar systems without restrictions on geometry, system design, bandwidth or any other key parameter. The key hypothesis of this work is that it is possible, with commodity computing hardware, to simulate the performance of radar systems at the signal level with no restrictions on the parameters of the systems to be simulated.

1.1.1 Radar Simulation

Radar simulators can be divided into a number of categories depending on the type of results they are intended the produce, and the expectations of the end user. Broadly defined, the categories of radar simulators are:

Result simulators produce a simulation of the results, after processing, which could be expected when a radar system is run in a particular environment. These types of simulators are useful for training both humans and machines in result interpretation, training humans on radar system operation, and simulating the effects of radar countermeasures and camouflage. These types of simulators can run extremely efficiently, as they do not need to model the actual operation of a radar system — only the expected results.

Figure 1.1 illustrates the results of the SAR image simulator, SARviz, developed by Balz, et. al. [1] The simulator has produced a simulation of how an E-3 Sentry aircraft would appear to a SAR system. Other

Figure 1.1: Simulated SAR image of E-3 sentry aircraft, created by SARviz (from [1])

.

examples of simulators of this type include those developed by Meyer-Hilberg [12], and Sevgi and Tanal [13].

Statistical simulators produce statistical models of the performance of a radar system in a given environment. The results of these types of simulators are performance data such as coverage maps, detection probabilities, and maximum detection ranges. Like result simulators, these types of simulators do not simulate the return signal — only the statistical properties of some parameters of that signal.

The results of statistical simulators rely heavily on the correctness of statistical performance models. While these predictions can be extremely accurate, their accuracy is restricted to the prediction of the performance of radar systems very similar to those for which the model was designed.

The first widely-used radar simulators were of this type, such as the one developed by Boothe [14] in 1964.

Signal level simulators produce the raw signals as would be received by the receiver in a radar system. These simulators model the the radar system and the propagation environment, in order to calculate the signal the system will receive. Unlike statistical simulators, the results

of a signal level simulator contain only a single sample of the statistical properties of the system, targets and environment.

Two radar simulators developed in 1997 and 1998 at the University of Cape Town, RadSim [15] and SARSIM II [2], are simulators of this type. Raw signal simulators have also been developed by Franceschetti et. al. [16, 17], Capsoni and D'Amicio [18], Xu and Jin [19], Nouvel et. al. [20], amongst others.

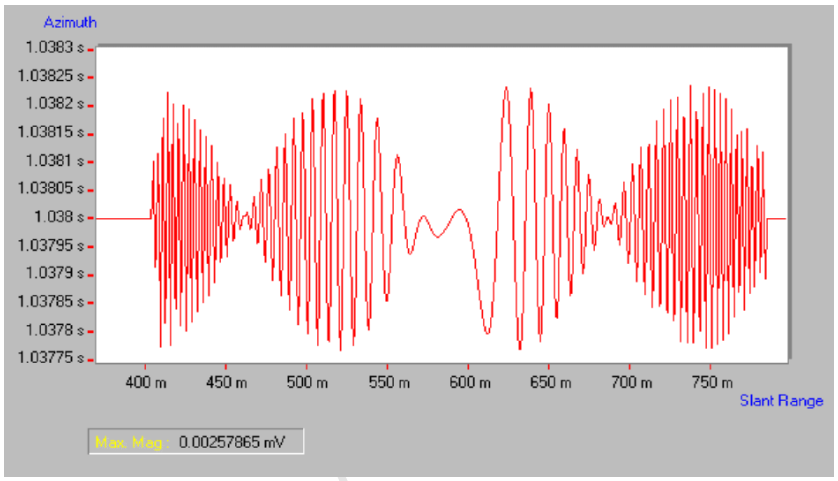

Figure 1.2: Result viewer from SARSIM II showing the raw signal results of simulation (from [2])

.

Electromagnetic Simulators simulate the physical laws of electromagnetic radiation, and produce results indicating the properties of the electromagnetic field at discrete points in space. This type of simulation is extremely useful in predicting the behaviour of individual parts of radar systems (such as antennas and targets), but is not suited to the simulation of complete systems.

1.1.2 Non-Functional Software Requirements

Flexibility

Figure 1.3 illustrates six possible radar configurations. In each of these configurations there are one or more transmitters of electromagnetic signals, one or more scatterers of those signals (targets), and one or more receivers which capture and record the signals. This selection represents only a tiny part of the diversity of radar systems, and clearly illustrates the need for a flexible simulator.

Flexibility refers to the simulators applicability to a wide variety of radar systems. Examples of supported systems include pulsed search radars (fig. 1.3(a)), netted radars (figs. 1.3(c) and 1.3(d)), airborne radars (figs. 1.3(b) and 1.3(e)), electronic warfare systems (figs. 1.3(e) and 1.3(f)) and continuous wave radar systems (fig. 1.3(d)).

The simulator was required to make no assumptions about waveforms; system geometry and arrangement; system bandwidth; and numbers of targets, transmitters and receivers. The simulator will not perform any signal processing on the output data, and makes no assumptions about the type of signal processing that will be performed on the data.

Flexibility is a large part of the contribution of this work to the field of signal-level radar simulation. Previous simulators have been typically focused on a single application domain (monostatic pulsed systems in [15] and [2], or SAR in [16] and [21], for example) or particular systems (the MARSIS radar in [20], for example). The simulator presented in this work is intended to be applicable to most radar application domains, and the majority of radar systems.

Accuracy

The simulator is required to produce results which are accurate and precise within a well described set of assumptions and bounding criteria. Limiting assumptions and limitations on simulation accuracy must be clearly documented and discussed to ensure that the user is aware of these before applying simulation results. Where tradeoffs require limitations on accuracy, the sim-

ulator must ensure that the maximum possible accuracy and precision in the parameters commonly used by radar signal processing algorithms are retained.

Extensibility

The simulator is required to easily accept extensions and modifications to allow for simulation of systems not included in the scope of the original simulator. The extensibility requirement is two-fold. The simulator must be able to accept extensions without modifying the base code, and the base code must be easily modifiable to aid inclusion of extensions if the external interfaces are inadequate.

Usability

ISO 9241-11 [22] defines usability in the context of software for office and technical work as:

> The extent to which a product can be used by specified users to achieve specified goals with effectiveness, efficiency and satisfaction in a specified context of use.

The simulator is required to maximize this property, ensuring that it is effective and efficient to use. In the context of this work, usability is focused on efficiency and effectiveness of use by an experienced user, not the ease of learning to use the software for the first time.

Maximizing usability requires clear, well defined and consistent interfaces; comprehensive documentation and predictable behaviour.

Portability

The simulator must not be restricted to any operating system or computer architecture. The software will be written in standard C++ [23], a programming language which is well supported on a variety of operating systems and architectures. The extension mechanism is implemented in Python, with interpreters available for all modern platforms and operating systems.

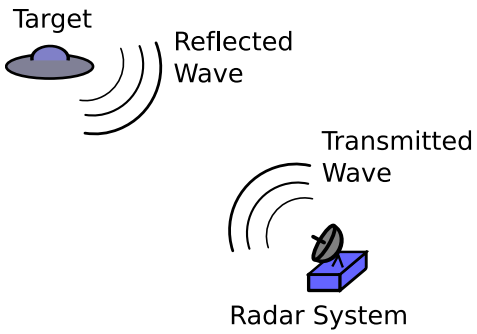

(a) Monostatic radar configuration with a single target

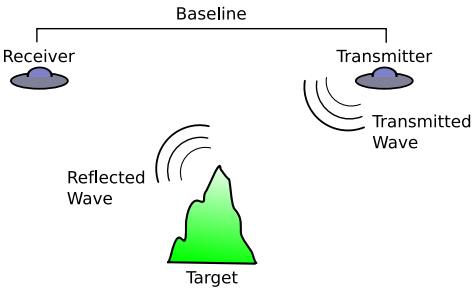

(b) Bistatic airborne radar configuration with a single complex target

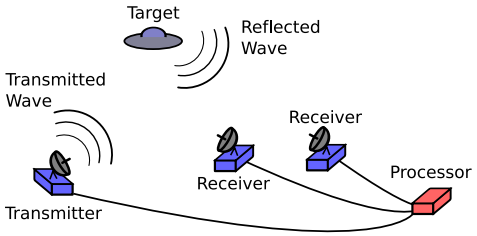

(c) Netted radar configuration with a single target, single transmitter and two receivers

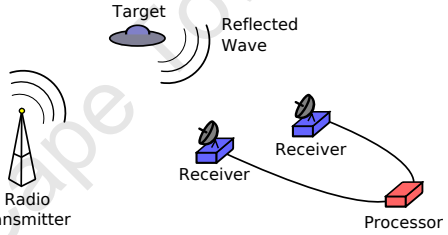

(d) Netted passive radar system, using a non-cooperating FM transmitter for illumination

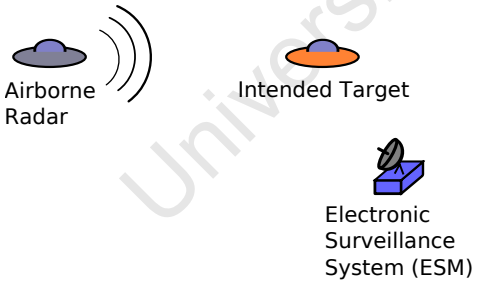

(e) Electronic surveillance system, detecting an airborne target using emissions from its own radar

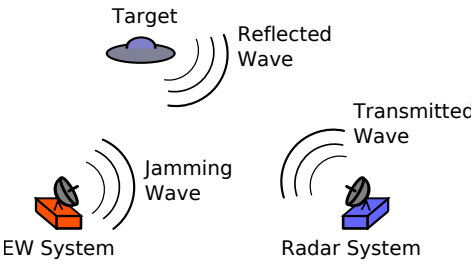

(f) Monostatic radar with a single target, and intentional jamming (EW)

Figure 1.3: Six widely used radar configurations, illustrating the diversity of radar systems — and the common elements present in every configuration.

1.2 Significance of Research

The exponential [24] rise of computing power available to engineers has lead to a similar rise in interest in the simulation of complex systems. Simultaneously, the rise of computing power and communications technology has lead to increasing interest in the application of the ideas of sensor networks to radar systems, greatly increasing the system level complexity, and hence difficulty of analysis, of radars. Simulation can provide an invaluable tool tool to radar researchers, engineers and operators.

The application of radar simulation in the research environment is to reduce the difficulty and costs associated with testing new radar technologies and approaches. Two traditional approaches are available to the researcher wishing to analyse the performance of a new technology — prototyping and closed form analysis. Simulation complements these two approaches by offering a third tool — one which is much cheaper and quicker than prototyping, but also easier and potentially more accurate than simplified analysis procedures. The simulation model presented in this work is sufficiently flexible to allow new technologies and hypotheses to be tested on a computer, reducing the need for the development and testing of prototypes.

Accurate simulation adds a useful tool to the design process followed by engineers working on the development of radar systems. The simulator reduces the amount of time required for the development of systems by allowing easy analysis of performance parameters of candidate designs. Similarly, the application of simulation can reduce the amount of money required for development by moving prototyping to a later stage in the design cycle — when fewer design changes are likely to be required.

Education and training of radar engineers and operators is another area where simulation can be used. The simulation can be used in the classroom to demonstrate to students the effects of system parameters on radar performance, and to allow students to freely experiment with these parameters. Combined with a suitable interface, the simulator can also be used to develop scenarios for the training of radar operators.

The application of radar simulation to research, development and education

provides a strong motivation for the development of a simulator which is useful in all three of these roles.

1.3 Structure of Thesis

This chapter, **Chapter 1**, discusses the objectives of the research which has been performed, the central hypothesis behind the research, and the approach used to meet the required objectives. The final part of the chapter examines the parts of the work which are believed to be novel contributions to the field of radar. A brief discussion of past approaches to radar simulation is included to support the objectives and approach. The key non-functional requirements for the completed simulator are explained, and the importance of each parameter examined.

Chapter 2 describes a flexible signal-level model for the simulation of multistatic radar systems. The description includes discussions of the modelling of the effects on radar signals of transmission, scattering, propagation and reception. The model is applicable to radar systems with arbitrary numbers of receivers and transmitters, and arbitrary numbers of scatterers in the simulated environment.

Chapter 3 examines the generation of pseudonoise with statistical properties matching those obtained from the characterisation of oscillators in radar hardware, and other sources of coloured noise in radar systems. An algorithm for the efficient generation of coloured pseudonoise samples for the purposes of radar simulation is described.

A model for clock generation in radar systems is presented, based on existing models of timing sources and oscillators. Key performance parameters for radar timing sources are discussed in the context of simulation of the effects of degradation of these parameters.

Chapter 4 examines the development of a radar simulator using the models and algorithms presented in Chapters 2 and 3. The design of the software is presented and discussed, and justification for the choices made during implementation is presented.

An overview of the software engineering design process is presented, with

an examination of the efficient implementation of the simulation model on parallel computers. The implementation of the simulator in C++ and the extension mechanism in Python is presented, with a discussion of the key performance parameters identified during implementation.

Chapter 5 presents the experimental validation and verification process which has been undertaken to ensure the accuracy of simulation results. The design of the equipment and experiments used for this verification process is presented, along with the design of simulation scenarios matching these experiments. Validation results from the NetRad netted radar system and from an experimental sonar system are presented. Comparisons of simulation and measurement results with theoretically expected values are presented and analysed.

Chapter 6 concludes the work, and presents a list of possible future extensions to the work presented here.

1.4 Statement of Originality

The candidate believes that the following parts of this work constitute original contributions to the field of radar:

- The flexible simulation model, presented in Chapter 2, which allows signal level simulations of radar systems with arbitrary number of transmitters and receivers and arbitrary waveforms. This model is applicable to a wide variety of types of radar systems, including multistatic, continuous wave, and carrier-free systems. The flexibility and completeness of this model exceeds that of the simulation models presented in existing literature.

- An algorithm for the efficient generation of coloured pseudonoise sequences matching the measured characteristics of oscillators, presented in Chapter 3.

- An algorithm for the efficient generation of sparse sequences of coloured pseudonoise, presented in Chapter 3. This algorithm efficiently generates

the pulsed sequences of coloured pseudonoise required for simulation of pulse radar systems, while preserving the long memory nature of the underlying noise generation process.

- The application of finite impulse response (FIR) subsample delay filters, generated at runtime, to the accurate simulation of delay effects, including both propagation delay and apparent delays caused by timing jitter, in a digital radar simulator. This development allows the simulator to accurately simulate the effects of these delays on any type of radar waveform.

- The application of FIR subsample delay filters, generated at runtime, to the accurate simulation of Doppler and phase effects in carrier-free and continuous wave (CW) radar systems.

- The development of a flexible, extensible and freely available simulator for multistatic and netted radar systems. The flexibility of the simulator described in this work exceeds that of other freely available and well described simulators. The simulator can be used to simulate radar systems with arbitrary waveforms and arbitrary numbers of receivers, transmitters and scatterers.

- The Monte Carlo simulation of the effects of phase noise on synthetic aperture radar (SAR) and pulse-Doppler systems, as presented in Appendix A, is novel in its use of a phase noise generator capable of generating realistic phase noise spectra.

Chapter 2

Discrete-Time Radar Simulation Model

2.1 Introduction

This chapter describes a model for the simulation of a diverse range of radar systems. The goal was to produce a model which is sufficiently generic to adequately describe a wide variety of radar systems, while being sufficiently specialised to allow efficient simulation. The simulation model is the most important component of simulator development — the limitations of the model are the limitations of the simulation, and the assumptions made during model development are reflected in the simulator output.

The simulation model utilizes the superposition property of multistatic radar systems, allowing the task of multistatic radar simulation to be decomposed into multiple bistatic radar simulations. Each of these bistatic radar simulations is performed using a two part bistatic radar simulation model. This chapter provides justification for the use of superposition, and describes the two parts of the radar simulation model in detail. In addition, the parameters used for adjusting the model to match a particular system are discussed, with emphasis on the relation of these parameters to physical radar systems.

The simulation model was developed with software implementation in

mind. A discussion of the implementation of this model in software is presented in Chapter 4.

2.1.1 Superposition of Radar Systems

The principle of superposition applies to many of the key effects on signals in radar systems. Expressed as a function $f(x)$, these effects meet the criteria of linearity — homogeneity:

$$f(\alpha x) = \alpha f(x), \tag{2.1}$$

and additivity:

$$f(x + y) = f(x) + f(y). \tag{2.2}$$

Justifications for this observation will be given for the relevant phenomena in this chapter. Based on the principle of superposition, a simple model for the signals captured by receivers in multistatic radar systems can be formed. The discrete-time signal $y_i[k]$ (where $y_i[k]$ is the kth sample of the bandlimited signal $y_i(t)$) received by receiver i, can be expressed as a sum of the modified transmitted signals:

$$y_i[n] = \sum_{j=0}^{N_T} f_{ij}(x_j[n]), \tag{2.3}$$

where N_T is the number of transmitters, x_j is the signal transmitted by transmitter j, and $f_{ij}(x)$ is some linear (but not necessarily time invariant) function which modifies the signal $x_j[n]$.

Considering the effects of transmission, propagation and reception separately, the received signal can be expressed as:

$$y_i[n] = R_i\Big(\sum_{j=0}^{N_T} E_{ij}(T_j(x_j[n]))\Big), \tag{2.4}$$

where R_i is the effect of reception by receiver i, E_{ij} is the environmental effect of propagation along the path from transmitter j to receiver i, and T_j is the effect of transmission by transmitter j. As these effects are not time invariant, it is more accurate to express them as $R_i(x, t)$, $T_j(x, t)$ and $E_{ij}(x, t)$

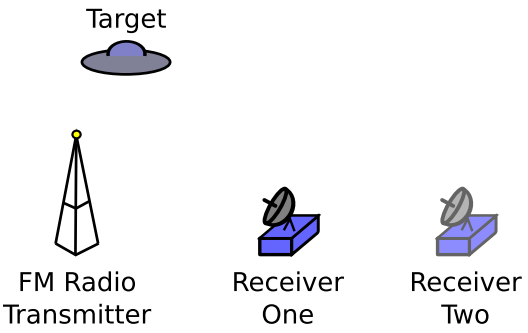

Figure 2.1: Bistatic passive receiver system

— functions of both the signal and time. The key challenge in simulation is to find the functions $R_i(x,t)$, $E_{ij}(x,t)$ and $T_j(x,t)$ which accurately model the behaviour of the system under simulation.

2.1.2 Validity of Superposition

Modelling radar systems using equation 2.3 requires several assumptions to be made about the behaviour of those systems. Theses assumptions are:

- No interaction between receivers. Each receiver in the radar system has no effect on the signal received by the other receivers in the system. This requires receivers to be passive listeners which do not emit or absorb energy from the environment.

  In the system illustrated in figure 2.1, under this assumption *receiver one* will receive exactly the same signal at its antenna irrespective of whether *receiver two* is present. This assumption is valid for most common types of radar systems.

- No interaction between targets. No multiscatter returns — reflections of energy from one target off another — are considered. The case of multipath propagation is considered separately. In the system illustrated in figure 2.2, three propagation paths via the targets exist: from the transmitter to the first target and to the receiver; from the transmitter to the second target and to the receiver; and from the transmitter to

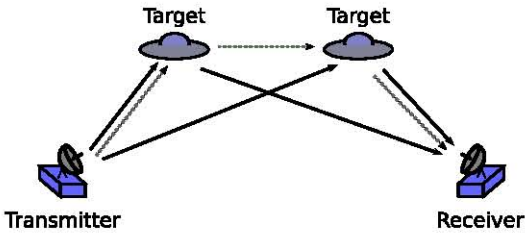

Figure 2.2: Bistatic radar system showing possible propagation paths.

the first target, to the second target then to the receiver. The third path (marked with a dashed line in figure 2.2) is not considered by the superposition model.

- No interaction between transmitters. Transmitters of electromagnetic waves into the environment are assumed not to interact with other transmitters — that is they do not absorb or otherwise modify the waves transmitted by other transmitters. Similarly, superposition is assumed to be valid for all interactions of electrodynamic waves and targets. This assumption holds exactly in a vacuum, due to the linearity of Maxwell's equations in that medium [25], and holds closely in air at all radar frequencies. These assumptions are examined in more detail in Appendix B.

2.1.3 The Discrete Signal Model

For computer simulation of an analogue system, a discrete representation of the analogue model is required. This representation is required to be both discrete-time, as the computer cannot handle infinite numbers of samples, and discrete in precision, as the computer cannot handle infinite precision.

The signals transmitted by radar systems can be separated logically into two categories: *lowpass* signals and *bandpass* signals. As illustrated by figure 2.3, the Fourier transform of lowpass signals is limited to the band $[-\Omega, \Omega]$. The Fourier transform of a bandpass signal is constrained to a band around the centre frequencies Ω_c and $-\Omega_c$ with bandwidth $B = \Omega_h - \Omega_l$. The majority of radar signals are bandpass signals — lowpass signals are only widely used

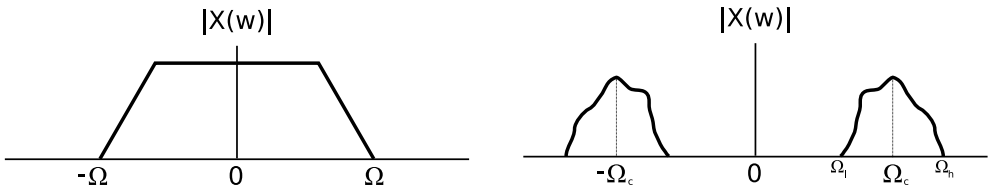

(a) Lowpass signal (b) Bandpass signal

Figure 2.3: Comparison of real valued lowpass and bandpass radar signals.

in carrier-free radar systems [26]. While the simulator supports both types of radar signals, a significant reduction in computational costs can be achieved through the use of a suitable model for bandpass signals.

The bandpass signal $x(t)$ can be expressed as:

$$x(t) = a(t)\cos\left(\Omega_c t + \theta(t)\right), \tag{2.5}$$

where $a(t)$ is the envelope and $\theta(t)$ the phase of $x(t)$. Equivalently, $x(t)$ can be expressed in terms of *inphase* and *quadrature* parts [27]:

$$x(t) = x_i(t)\cos(\Omega_c t) - x_q(t)\sin(\Omega_c t), \tag{2.6}$$

where $x_i(t)$ and $x_q(t)$ are real valued baseband signals and are referred to as the inphase and quadrature parts of $x(t)$. The complex envelope $x_l(t)$ is defined as:

$$x_l(t) = x_i(t) + jx_q(t). \tag{2.7}$$

$x_l(t)$ is complex, situated at baseband, and has bandwidth $\Omega_h - \Omega_l$. The Fourier transform of $x_l(t)$, $X_l(\omega)$ (Figure 2.4) is:

$$X_l(\omega) = X_i(\omega) + jX_q(\omega). \tag{2.8}$$

For simulation of radar systems transmitting bandpass signals, it is convenient to simulate using the complex envelope $x_l(t)$, and include phase effects relevant to the original carrier frequency $2\pi\Omega_c$.

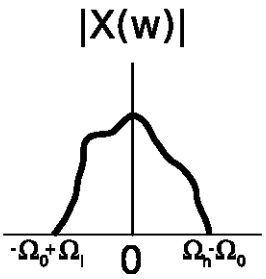

Figure 2.4: Magnitude of the Fourier transform of the complex envelope of the signal $x(t)$

Discrete-Time Representation of Analogue Signals

The discrete-time signal $x[n]$, equivalent to the continuous time signal $x(t)$ is defined as:

$$x[n] \equiv x\left(\frac{n}{f_s}\right), \tag{2.9}$$

where f_s is the system sampling frequency. Provided that the signal $x(t)$ is bandlimited to the range from 0Hz to $\frac{f_s}{2}$Hz [28, 29] and satisfies the Dirichlet conditions [30] then,

$$x(t) = \sum_{n=-\infty}^{\infty} x[n]\,\mathrm{sinc}\left(tf_s - n\right), \tag{2.10}$$

where $\mathrm{sinc}(x) = \sin(\pi x)/(\pi x)$. Performing the simulation using $x[n]$ is therefore equivalent to simulating using $x(t)$, provided that none of the simulated effects cause $x(t)$ to violate the criteria required for reconstruction. The sampling rate f_s must be chosen to ensure that the simulated $x(t)$ remains limited to the band $[0, \frac{f_s}{2}]$ when phase and frequency shift effects are considered.

Quantization Effects on the Signal Model

Computer simulation requires mapping of the samples $x[n]$ to a finite number of bits of precision, known as quantization. For the fixed point (or integer) case the quantization step, Δ, is defined [31] as:

$$\Delta = \frac{X_m}{2^B}, \tag{2.11}$$

where $x[n]$ is in the range $[-X_m, X_m]$ and B is the number of bits in the quantized representation. The quantization error:

$$e[n] = Q(x[n]) - x[n], \tag{2.12}$$

where $Q(x)$ is the quantization process, is bounded [29] to the range $-\Delta/2 < e[n] \leq \Delta/2$ where $(-X_m - \Delta/2) < x[n] \leq (X_m - \Delta/2)$. The mean square error of quantization, for sufficiently complex signals where no clipping occurs can be approximated [32, 33] by:

$$\overline{e[n]^2} \approxeq \frac{\Delta^2}{12} \tag{2.13}$$

For sufficiently complex signals, where the quantization step Δ is sufficiently small, it can be assumed that the quantization error $e[n]$ is uniformly distributed over the the error range, is a sample sequence of a white noise process [29, 34, 35], and is uncorrelated with $x[n]$. In order to achieve simulation accuracy, the number of bits must be selected so that these criteria hold, and the quantization noise power (equation 2.13) is sufficiently low. The ideal signal to noise ratio (SNR) for quantization to B bits is [29, 34]:

$$\text{SNR} = 10\log_{10}\left(12\frac{2^{2B-2}\sigma_x^2}{X_m^2}\right) = 6.02(B-1)+10.79-20\log_{10}\left(\frac{X_m}{\sigma_x}\right), \tag{2.14}$$

decibels, where σ_x is the RMS amplitude of $x[n]$.

Where quantization is performed using floating point numbers [36], estimating the quantization error is more complex [37, 38] than with integer quantization due to the effects of changing precision with changing exponent. The lower bound on the floating point quantization SNR is the SNR of integer quantization to the number of bits in the floating point mantissa [39]. IEEE754 [36] single precision has 24 mantissa bits, and double precision 52 bits. For double precision, the minimum SNR due to quantization noise is approximately 310dB, which is sufficiently high that quantization noise does not significantly contribute to the noise floor of signals in all physically realizable radar systems. In order to achieve this performance, the implementation

must take care to ensure that floating point arithmetic operations are done in the order which preserves maximum accuracy [39, 40].

Representation of Polarization

An important property of the signals used in radar systems is polarization, taken to refer to the orientation of the E field vector. While digital signals have no inherent notion of polarization, it is necessary to track the polarization of simulated signals for accurate modelling of target interactions, multipath effects and interaction with the receiving antenna.

The Stokes vector [41] is widely used in optics to represent the polarization of light, and can represent both polarized and depolarized signals. As radar signals are typically polarized, the conceptually simpler Jones vector [41] and associated Jones calculus [42, 43, 44] are ideal for the representation of the polarization of radar signals.

The Jones vector represents a polarized signal by the vector

$$\begin{bmatrix} E_x(t) \\ E_y(t) \end{bmatrix}, \tag{2.15}$$

where $E_x(t)$ and $E_y(t)$ are the orthogonal components of the electric field. For the representation of polarization only (and not magnitude), the components are normalized:

$$\Big(E_x(t)\Big)^2 + \Big(E_y(t)\Big)^2 = 1. \tag{2.16}$$

The Jones vectors for various polarization cases are listed in Table 2.1. The representation of polarization with the Jones vector allows the use of the polarization scattering matrix (PSM) to represent the polarization effects of target and surface interaction. These effects are detailed in Section 2.2.5.

2.1.4 Model Coordinate System

The co-ordinates of all objects in the radar simulation model are specified in $\mathbb{R}^3$ relative to an arbitrary datum point[1]. As illustrated in figure 2.5, these

[1]Where $\mathbb{R}$ is the field of real numbers

Table 2.1: Jones vectors corresponding to various polarization cases

Polarization	**Jones Vector**
x Linear	$\begin{bmatrix} 1 \\ 0 \end{bmatrix}$
y Linear	$\begin{bmatrix} 0 \\ 1 \end{bmatrix}$
Left circular	$\frac{1}{\sqrt{2}} \begin{bmatrix} 1 \\ j \end{bmatrix}$
Right circular	$\frac{1}{\sqrt{2}} \begin{bmatrix} 1 \\ j \end{bmatrix}$

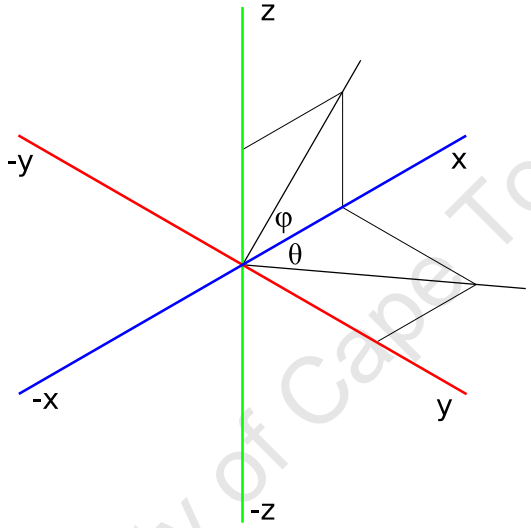

Figure 2.5: Axes of the model coordinate system

coordinates can be specified in terms of the Cartesian coordinates (x, y, z), or the spherical coordinates (r, φ, θ). In this document, to match common usage in radar literature, the zenith angle φ is referred to as elevation and is measured from the xy plane. The azimuthal plane angle θ is referred to as azimuth and is measured from the x axis.

The coordinate system is not referenced to any particular direction on the Earth — applications of the simulator model are free to choose any direction and datum point as a reference. The advantage of this system over the north referenced coordinate system commonly used in the radar field [45] is flexibility and applicability to a wide variety of radar configurations — not all terrestrial.

The conversion of geodesic coordinates to Cartesian coordinates relative to

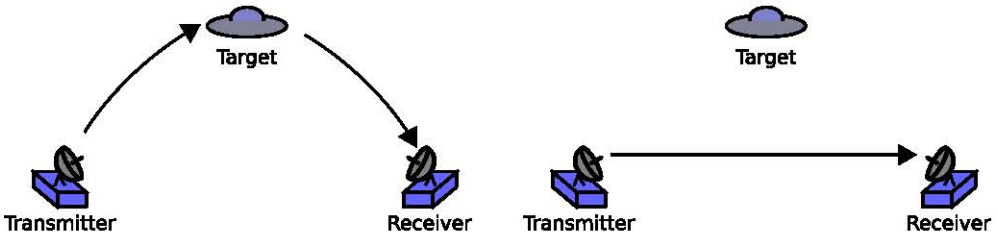

(a) Transmission path from transmitter to receiver via target

(b) Direct transmission from transmitter to receiver

Figure 2.6: Transmission paths for transmitted energy from transmitter to receiver.

an arbitrary datum point is a complex problem, and depends on the geodetic system (such as WGS84 [46]) used for the measurement of the coordinates. For even modest ranges care must be taken in ensuring that the conversion to Cartesian coordinates accounts for the assumptions of the geodetic system in use.

2.2 Environment Model

The environment model, $E_{ij}(x)$, predicts the effects of propagation of the signal x through the environment from transmitter j to receiver i. This model depends on the positions and relative velocities of the transmitter j, receiver i and all targets during the simulation period, as well as the properties of the transmitters, receivers and targets.

Through the application of the superposition principle (Section 2.1.1), the environment model is only concerned with a single transmitter-receiver pair — while the entire simulator can handle arbitrary numbers of such pairs.

Considering both the direct (Figure 2.6(b)) transmitter to receiver transmission path, and the paths via targets (Figure 2.6(a)), the environment model can be expressed as:

$$E_{ij}(x) = P_{ij}D_{ij}(x) + \sum_{k=1}^{S} P_{ijk}D_{ijk}(x), \tag{2.17}$$

where P_{ijk} and P_{ij} are the attenuation due to propagation, D_{ijk} and D_{ij} are

the phase and frequency (Doppler) effects due to range and relative motion of receiver i, transmitter j and target k, and S is the number of targets in the environment.

2.2.1 The Object Model

In order to calculate the effects of propagation through the environment, the model is required to keep track of the positions and properties of all the objects in the environment. This is achieved through the application of an hierarchical object model. The object model consists of six types of objects; two parent object types and four physically realizable object types.

Figure 2.7 illustrates the object model, with the four physical object types marked in grey. The six types of objects are:

Platform The platform parent object keeps track of the motion and rotation of its child objects. A platform object has a defined three dimensional path through the simulated world, and a defined rotation around an arbitrary axis. All other types of objects depend on a platform object, and can move without restriction through the simulated environment.

Radar The radar parent object embodies the common properties of radar transmitters and receivers. The modelling of time and frequency control, antenna behaviour and synchronisation behaviour is handled by the radar object. A radar object can contain either a single transmitter, single receiver, or both.

Target Targets represent any object in the environment which absorbs energy from the environment, then re-emits that energy. The target object models the RCS (including bistatic RCS and time dependent RCS) and other aspects of target behaviour. Target motion is modelled by the parent platform object.

Surface Surfaces represent planes in the environment with purely specular (as defined in [41]) reflection of radar energy. Surfaces are used to simulate the effects of multipath propagation.

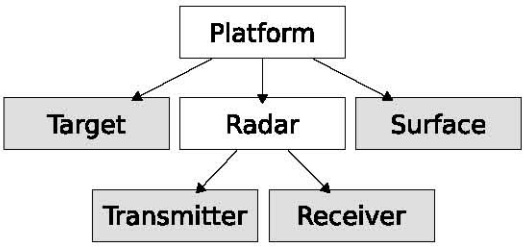

Figure 2.7: Heirarchy of objects in the object model

Transmitter Transmitters represent any object which transmits electromagnetic energy into the environment. The transmitter object models the transmission schedule, transmitted waveform and the properties of the transmitted signal. Antenna behaviour is modelled by the parent *Radar* object.

Receiver Receivers represent objects which receive electromagnetic energy from the environment, then capture a record of that energy. The receive object models the receive schedule (receive window) and the properties of the receiver hardware (such as gain, ADC precision, etc).

The object model keeps track of any number of each type of object. No restrictions are placed on the arrangement, movement or rotation of objects in the object model.

2.2.2 The Bistatic Radar Equation

The propagation attenuation for target paths is calculated using the bistatic radar equation [26, 47, 48]. The power radiated in the direction of receiver i by target k, illuminated by transmitter j is:

$$P_g = P_t \frac{G_t L_t L_{pt} \sigma_b}{4\pi R_{kj}^2}, \tag{2.18}$$

where P_t is the transmitted power, G_t the transmitter antenna gain in the direction of the target, L_t the loss in the transmitter, L_{pt} is the excess propagation loss, σ_b the bistatic radar cross section (RCS) for the transmitter and receiver angles, and R_{kj} the range between transmitter j and target k.

The power received by the antenna of receiver i from target k is:

$$P_r = P_g \frac{G_r L_r L_{pr} \lambda^2}{(4\pi)^2 R_{ik}^2}, \tag{2.19}$$

where G_r is the receiver antenna gain in the direction of the target, L_r the losses in the receiver system, L_{pt} is the excess propagation loss, λ is the wavelength at the centre frequency of the radar system, and R_{ik} the range between target k and receiver i. The total received power is therefore:

$$P_r = P_t \frac{G_t G_r L_t L_r L_{pr} L_{pt} \sigma_b \lambda^2}{(4\pi)^3 R_{kj}^2 R_{ik}^2}. \tag{2.20}$$

From a similar derivation, without including the target effects, the power received by receiver i directly from transmitter j is:

$$P_r = P_t \frac{G_t G_r L_t L_r \lambda^2}{(4\pi)^2 R_{ij}^2}, \tag{2.21}$$

where R_{ij} is the range from i to j.

2.2.3 Phase and Frequency Effects

The finite speed of propagation of electromagnetic energy through the environment introduces a delay on the arrival time of the transmitted signal at the receiver.

For bandpass signals, we can consider the propagation delay to have two separate effects on the signal — *phase* delay and *group* delay. From the definition of the complex baseband signal (equation 2.7), a delay by the propagation time τ can be expressed as:

$$x_{shift}[n] = x_i[n + \tau f_s] \cos(2\pi f_0 (t + \tau)) - x_q[n + \tau f_s] \sin(2\pi f_0 (t + \tau)), \tag{2.22}$$

where f_s is the system sample rate and $f_0 = \frac{\Omega_c}{2\pi}$. The delay on the complex baseband signal $x_l[n]$, τf_s samples, is the group delay, and the delay on the carrier signal, $2\pi f_0 \tau$ radians, is the phase delay. For lowpass signals, where

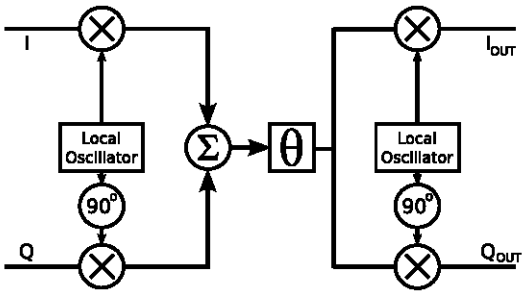

Figure 2.8: Block diagram of the effect of phase shift on quadrature reception. Upmixers include suitable low pass filters.

simulation is performed at the full system sample rate, only the group delay is considered.

Introducing a phase shift on the signal of a bandpass radar system, utilising a quadrature upmixer and downmixer, introduces mixing of the inphase and quadrature channels. For the system in figure 2.8, the signal after the carrier phase shift θ, equivalent to time delay by $\tau = \theta / (2\pi f_0)$ seconds, is:

$$x_{shift}[n] = I[n + \tau f_s] \cos(2\pi f_0 t + \theta) - Q[n + \tau f_s] \sin(2\pi f_0 t + \theta). \quad (2.23)$$

The output channel is therefore:

$$I_{out}[n] = x_{shift}[n] \cos(2\pi f_0 t), \quad \text{and} \quad (2.24)$$

$$Q_{out}[n] = x_{shift}[n] \sin(2\pi f_0 t) \quad (2.25)$$

which is equal to:

$$I_{out}[n] = I[n + \tau f_s] \cos(\theta) - Q[n + \tau f_s] \sin(\theta), \quad \text{and} \quad (2.26)$$

$$Q_{out}[n] = Q[n + \tau f_s] \cos(\theta) + I[n + \tau f_s] \sin(\theta). \quad (2.27)$$

Considering only the time shift τ (and hence carrier phase shift θ), and using the definition of the complex baseband signal in equation 2.7, the output of the system in figure 2.8 is:

$$y[n] = x_l[n + \tau f_s] e^{j\theta}. \quad (2.28)$$

Equivalently, for lowpass signals, the output of the system is:

$$y[n] = x_l[n + \tau f_s], \tag{2.29}$$

and lowpass signals can clearly be considered to be a special case of baseband signals where $f_0 = 0$ and $x_l[n]$ is purely real. Where $\tau f_s \notin \mathbb{Z}$, some interpolation[2] is required to meaningfully define $x_l[n + \tau f_s]$. The ideal definition is based on bandlimited interpolation (equation 2.10), and an implementation of this interpolation is presented in Section 4.3 on page 97.

The time delay τ is:

$$\tau = \frac{R_{jk} + R_{ik}}{c}, \tag{2.30}$$

where R_{jk} and R_{ik} are the transmitter-target and target-receiver ranges, and c is the propagation speed. For radar applications $c \approx c_0$, where c_0 is the speed of light in a vacuum (299792458ms^{-1}) [49]. For radar in air, $c = \frac{c_0}{n}$, where n is the refractive index of air, approximately $1 + 2.92 \times 10^{-4}$ at STP [41]. The propagation speed c in air is therefore ~ 299704746ms^{-1}. For sonar simulations, c is the speed of sound in the relevant medium.

In both narrowband and wideband cases, the group delay is equal to τ seconds. In the narrowband case, the phase delay experienced by the carrier is:

$$\theta = 2\pi f_0 \frac{R_{jk} + R_{ik}}{c} = 2\pi f_0 \tau. \tag{2.31}$$

The Doppler Effect

The Doppler effect for velocities much less than the speed of light is widely expressed in terms of frequency. For monostatic geometries, the Doppler shift [26, 50] is:

$$f_d = \frac{2v_r}{\lambda}, \tag{2.32}$$

where f_d is the Doppler shift, and v is the radial velocity of the target relative to the radar system and $v_r \ll c$. For bistatic systems:

$$f_d = \frac{v_r + v_t}{\lambda}, \tag{2.33}$$

[2]Where $\mathbb{Z}$ is the ring of integers

where v_t and v_r are the radial velocities of the target relative to the transmitter and receiver and $|v_t| + |v_r| \ll c$. While these equations do not take the relativistic Doppler effect into account, they match the relativistic Doppler prediction within 0.1% for total velocities less than $6 \times 10^5 \text{ms}^{-1}$. Expressed in terms of range, the instantaneous Doppler shift is:

$$f_d = \frac{f_0}{c}\left(\frac{dR_{ik}}{dt} + \frac{dR_{jk}}{dt}\right), \tag{2.34}$$

for propagation via a target. Substituting equation 2.30 into equation 2.34,

$$f_d = f_0 \frac{d\tau}{dt}. \tag{2.35}$$

From equations 2.31 and 2.35 it is clear that the Doppler shift is equal to a change in phase and group delay corresponding to the change in range. In a discrete-time model, it it therefore not necessary to consider Doppler separately from the propagation delay τ for each sample. If τ is calculated per-sample, and $f_d(t)$ is properly sampled at f_s, it is not necessary to consider the Doppler effect at all for either the bandpass or lowpass cases.

It is necessary to ensure that $x_l[n]$ remains correctly sampled after the application of time dependent phase shifts. Where B is the bandwidth of $x_l[n]$, the sampling frequency f_s must be chosen such that:

$$f_s > 2\left(B + f_d\right), \tag{2.36}$$

in order to avoid aliasing.

2.2.4 Target Model

Targets in the simulator model are assumed to be point-like reflectors with a specified bistatic RCS. The bistatic RCS is a function of both the measured cross section of the target, and probabilistic variations in the apparent RCS of the target.

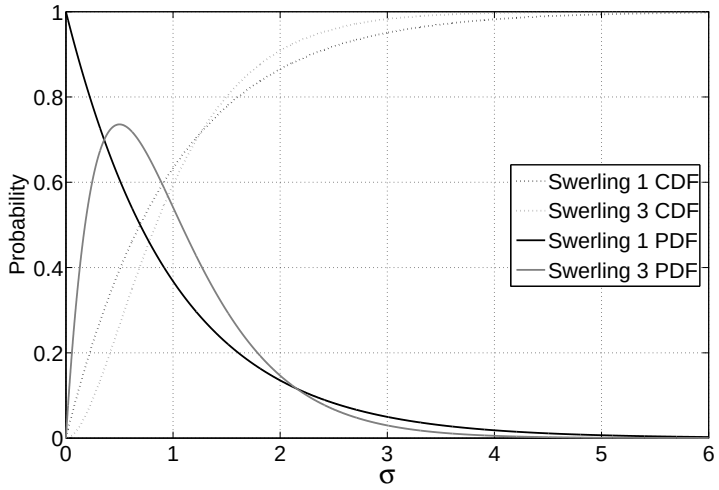

Figure 2.9: Cumulative density functions and probability density functions for Swerling cases 1 and 3 ($\bar{\sigma} = 1$)

The Swerling Cases

Statistical models of time dependent radar cross section fluctuations are widely applied in the simulation and analysis of radar systems [26, 50, 51]. While the most commonly applied statistical models are the Swerling cases [52, 53, 54], these have been found to be inadequate for many common radar applications [55, 56, 57]. While many alternatives [58, 21, 59] are available, the chi-square target model proposed by Swerling [57] is attractive as it is easily implemented and widely applicable.

The traditional Swerling RCS fluctuation model [54, 53, 51] breaks RCS fluctuations down into five cases. For cases one and two, the RCS probability density function is:

$$p(\sigma) = \frac{1}{\bar{\sigma}} \exp\left(-\frac{\sigma}{\bar{\sigma}}\right) \quad \sigma \geq 0, \tag{2.37}$$

where σ is the RCS and $\bar{\sigma}$ is the mean value of the RCS. In case one, the RCS is constant throughout a scan, and is uncorrelated between scans. In case two, the RCS is constant throughout a pulse, and is uncorrelated between adjacent pulses.

For Swerling cases three and four, the RCS PDF (illustrated in figure 2.9) is:

$$p(\sigma) = \frac{4\sigma}{\bar{\sigma}^2} \exp\left(-\frac{2\sigma}{\bar{\sigma}}\right) \quad \sigma \geq 0. \tag{2.38}$$

In case three, the RCS is constant throughout a scan and uncorrelated between scans, similar to case 1. In case four, the RCS is constant throughout a pulse and uncorrelated between pulses. Case five corresponds to a constant value of the target RCS.

Chi-Square RCS Model

The two parameter Chi-square probability density function for $2k$ degrees of freedom is [57, 60]:

$$p(x, \bar{x}) = \frac{k}{\Gamma(k)\bar{x}} \left(\frac{kx}{\bar{x}}\right)^{k-1} \exp\left(\frac{-kx}{\bar{x}}\right) \mathrm{u}(x), \tag{2.39}$$

where $\Gamma(x)$ is the Gamma function [61], $\mathrm{u}(x)$ is the unit step function and $\bar{x}$ is the mean of x.

The Chi-square model is related to the Swerling cases by the choice of the parameter k. Table 2.2 lists values of k for the Swerling cases, Weinstock's model [58] and the constant RCS case. Values of k between 0.3 and 2 have been found to be applicable to simple target shapes [51].

Table 2.2: Relation of chi-square fluctuations to other commonly used fluctuation models

Model	**Value of k**
Constant RCS (No fading)	∞
Swerling 1 and 2	1
Swerling 3 and 4	2
Weinstock	0.5

Similarly to the Swerling cases, the Chi-square distributed RCS value can be considered to change between pulses, or between scans. For CW systems, the pulse and scan times are not defined, and some other criterion must be chosen for the time dependent variation of RCS. For the simulated target

model in CW systems, the RCS changes every T seconds, with the values between changes interpolated with cubic spline interpolation [62].

While the Chi-square distributed RCS model is widely used, and applicable in many situations, other models for RCS fluctuations have been developed, which can offer better fits to experimental data in some cases. Alternatives to the chi-square model include models based on the Rician distribution [63], log-normal distribution [64, 65], Legendre polynomials [21] and the non-central Gamma distribution [59].

Target RCS Variation with Angle

The variation in radar cross section with the arrival and departure angles is as important to system performance as statistical fluctuations in the target RCS [66, 67]. The target model considers both the monostatic and bistatic radar cross sections of the target, by defining RCS as a function of the angle of arrival, angle of departure and the signal polarisation angle. The bistatic RCS σ_b in the radar equation (equation 2.20) is therefore [68]:

$$\sigma_b = \sigma\left(\theta_a, \phi_a, \theta_d, \phi_d, \phi_s\right), \tag{2.40}$$

where θ_a and θ_d are the azimuth angles of arrival and departure, ϕ_a and ϕ_d are the elevation angles of arrival and departure and ϕ_s is the signal polarization.

Where accurate measurements of bistatic RCS are available, σ_b can be interpolated from the measured data. Similarly, a variety of numerical methods are available for the calculation of bistatic RCS from target models [68, 69]. The availability of such data is useful for ensuring the accuracy of simulations.

Bistatic RCS measurements and simulations are not always available for simulations. Where monostatic measurements at $f_0 \cos(\beta/2)$ are available, for bistatic angle β, the monostatic RCS along the bisector of the bistatic angle accurately estimates the bistatic RCS for small β [70, 69], typically $\beta < 5^\circ$ [48].

To obtain the PDF of the bistatic RCS for a single target in the bistatic configuration, the bistatic RCS function $\sigma\left(\theta_a, \phi_a, \theta_d, \phi_d, \phi_s\right)$ is substituted for the mean RCS in equation 2.39. Discrete samples matching this RCS are

generated, per look or per pulse, and are used in equation 2.20.

Table 2.3: Parameters of the point target model

Parameter	**Unit**
Samples of bistatic RCS function values	m^2
Chi-square parameter k	

Table 2.3 lists the parameters of the target model. The bistatic RCS function is specified in terms of samples on a two dimensional grid, in azimuth and elevation.

2.2.5 Target Phase and Polarization Effects

Letting E_1^t and E_2^t represent the orthogonal components of the electric field of the transmitted plane wave on arrival at the target (the Jones vector), and E_1^r and E_2^r represent the components of the electric field of the plane wave re-radiated from the target on arrival at the receiver, the relation:

$$\begin{bmatrix} E_1^r \\ E_2^r \end{bmatrix} = \begin{bmatrix} S_{11} & S_{12} \\ S_{21} & S_{22} \end{bmatrix} \begin{bmatrix} E_1^t \\ E_2^t \end{bmatrix}, \tag{2.41}$$

can be formed [68, 71, 72], where S_{ij} are the target reflection co-efficients. The matrix:

$$S = \begin{bmatrix} S_{11} & S_{12} \\ S_{21} & S_{22} \end{bmatrix} \tag{2.42}$$

is called the polarization scattering matrix (PSM). The components of S include the effects of phase rotation, as they are complex valued, and are related to the RCS by:

$$S_{xy} = \frac{\sqrt{\sigma_{xy}}}{4\pi R_{ik} R_{kj}}, \tag{2.43}$$

where σ_{xy} is the complex radar cross section, and R_{ik} and R_{kj} are the transmitter-target and target-receiver ranges.

The PSM embodies all the effects of scattering from a single target for a single frequency and set of arrival and departure angles [68], and is a function of both the arrival and departure angles in a bistatic radar system. The RCS

model without considering phase and polarization effects corresponds to the PSM:

$$S = \frac{1}{4\pi R_{ik} R_{kj}} \begin{bmatrix} \sqrt{\sigma} & 0 \\ 0 & \sqrt{\sigma} \end{bmatrix}, \tag{2.44}$$

for $\sigma \in \mathbb{R}$. Where phase effects are considered, S remains diagonal, but complex values of σ are included.

The voltage received by the receiver j is [68]:

$$\sqrt{P_r} \propto \left| \vec{r_j} \cdot \begin{bmatrix} E_1^r \\ E_2^r \end{bmatrix} \right|, \tag{2.45}$$

where $\vec{r_j}$ is the polarization vector of the receiver j. Combining with the bistatic radar equation (equation 2.20) the return power becomes:

$$\sqrt{P_r} = \left| \vec{r_j} \cdot \begin{bmatrix} E_1^r \\ E_2^r \end{bmatrix} \right| \sqrt{\frac{P_t G_t G_r L_t L_r \lambda^2}{4\pi}}, \tag{2.46}$$

and the propagation phase shift (equation 2.31) becomes:

$$\lambda = \arg\left(\vec{r_j} \cdot \begin{bmatrix} E_1^r \\ E_2^r \end{bmatrix} \right) + 2\pi f_0 \frac{R_{jk} + R_{ik}}{c} \tag{2.47}$$

The RCS function can be specified to produce either real scalar RCS values or the components of the PSM. The specified RCS samples (Table 2.3) can therefore be either scalar or matrix values.

2.2.6 Bistatic Multipath Propagation

In an ideal bistatic radar system with a single target, two paths exist for energy to pass from the transmitter to the receiver: directly, or via a target. The addition of a plane with purely specular reflection to the configuration increases the total number of available paths to six, assuming that all objects are on the same side of the plane. The six paths are illustrated in figure 2.11(b). Propagation along any of the reflected paths alters the signal by attenuation, phase shift, and a change in polarization.

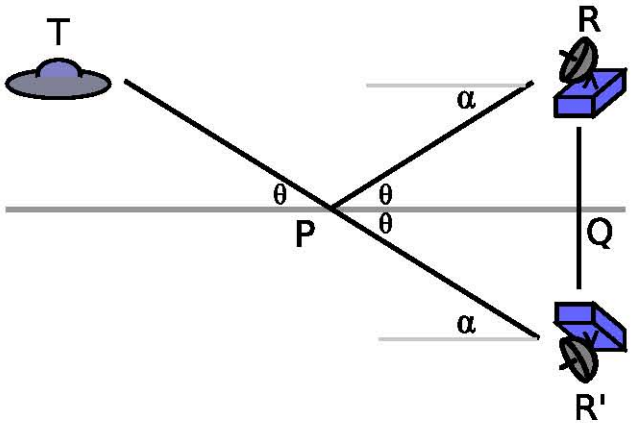

Figure 2.10: Geometric arrangement for reflection approach to multipath simulation

In a monostatic configuration with a single radar (at point R), and a single target (at point T), and two points of reflection from the plane (at P and Q), five propagation paths exist: RTR, RQR, RPTR, RPTPR and RTPR. Note that reflections are assumed to be purely specular — no paths such as RPR exist. Defining the point R', such that the distance RTR' is equal to RTPR and RQR' is equal to RQR, it can be shown that the angle of arrival α is equal for RTR' and RTPR, RPTR is equal to R'TR and RPTPR is equal to R'TR', as illustrated in figure 2.10. In this configuration, the plane of reflection can be removed, and the paths of propagation considered using a non-multipath model.

Given the equation of the plane of reflection as $ax + by + cz = d$, the point R' can be calculated as a reflection of the point R through the plane [73]:

$$\begin{bmatrix} x' \\ y' \\ z' \end{bmatrix} = \begin{bmatrix} -a^2+b^2+c^2 & -2ab & -2ac \\ -2ab & a^2-b^2+c^2 & -2bc \\ -2ac & -2bc & a^2+b^2-c^2 \end{bmatrix} \begin{bmatrix} x \\ y \\ z \end{bmatrix} - \begin{bmatrix} 2ad \\ 2bd \\ 2cd \end{bmatrix}, \quad (2.48)$$

provided $a^2 + b^2 + c^2 = 1$.

The reflected radar system R' must have its parameters adjusted to match the effects of the reflection of energy off the surface. These effects include a reduction in amplitude, phase shift and change in polarization [51]. Where

these effects have been included, the sum of the signals at R and R' without the surface is equal to the signal at R with the reflecting surface.

The complex envelope of the simulated reflected signal $x_r[n]$ can be expressed in terms of the complex envelope of the direct signal received from the transformed receiver $x_e[n]$ by:

$$x_r[n] = \rho x_e[n] e^{j\phi}, \tag{2.49}$$

where ρ and ϕ are dependent on the properties of the surface of reflection. This model considers only reflection from smooth surfaces, with a roughness correction factor.

Reflection Properties of Smooth Surfaces

Long [71] defines the *reflection coefficient*, or proportion of the total energy in the beam illuminating a surface reflected, as:

$$\text{Reflection coefficient} = \rho_s D \mathcal{R}, \tag{2.50}$$

where ρ_s is the reflection coefficient for a smooth earth, D is the reduction in reflection energy caused by curvature of the surface, and $\mathcal{R}$ is the reduction due to surface roughness. As the geometry in figure 2.10 is not valid for curved surfaces, the factor D is assumed to be unity. The roughness factor $\mathcal{R}$, where $0 \leq \mathcal{R} \leq 1$ depends on the roughness of the surface, where 0 and 1 correspond to extremely rough and completely smooth.

The factor ρ is dependent on the frequency and polarization of the signal and the angle of incidence (θ in figure 2.10), as well as on the electromagnetic properties of the surface. Where this discussion refers to *vertical* and *horizontal* polarization, it will mean perpendicular to and parallel to the surface of reflection. For a surface with permittivity K and conductivity σ, the complex dielectric constant ϵ is given by [71]:

$$\epsilon = \frac{1}{\epsilon_0}\left(K - \frac{j\sigma}{2\pi f_0}\right), \tag{2.51}$$

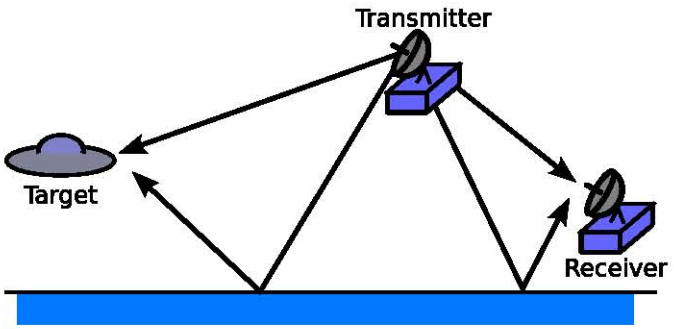

(a) Transmission paths

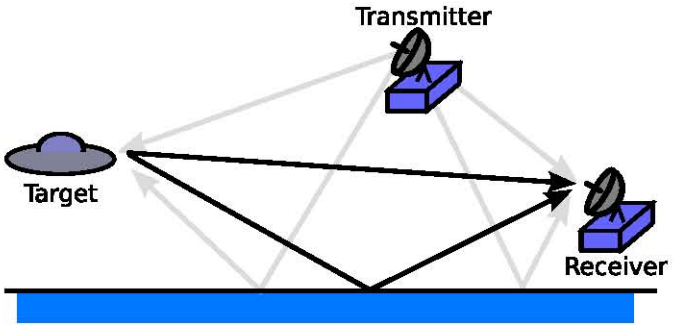

(b) Receive paths

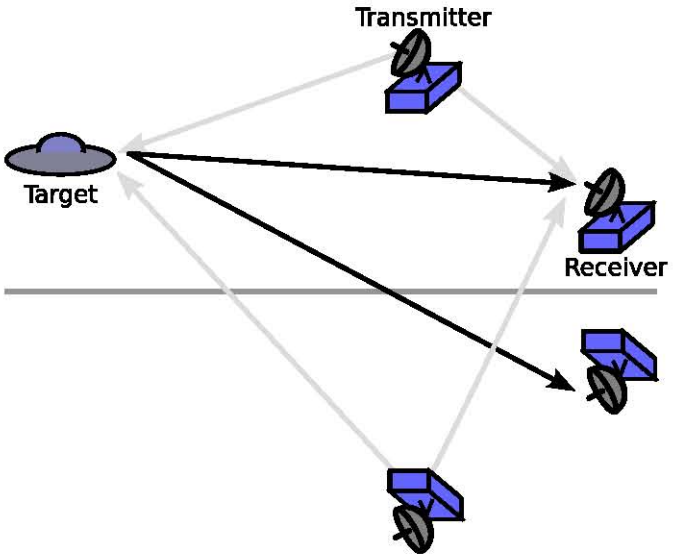

(c) Multiple paths replaced with multiple receivers and transmitters

Figure 2.11: Equivalence of rearrangement of system geometry and multipath propagation

where f_0 is the radar centre frequency and ϵ_0 is the electric constant [74]. For horizontal and vertical polarization respectively, the complex reflection coefficients are:

$$\Gamma_h = \rho_h e^{-j\phi_h} = \frac{\sin\beta - \sqrt{\epsilon - \cos^2\beta}}{\sin\beta + \sqrt{\epsilon - \cos^2\beta}} \tag{2.52}$$

$$\Gamma_v = \rho_v e^{-j\phi_v} = \frac{\epsilon\sin\beta - \sqrt{\epsilon - \cos^2\beta}}{\epsilon\sin\beta + \sqrt{\epsilon - \cos^2\beta}}, \tag{2.53}$$

where $\beta = \pi - \theta$. As Γ is a complex quantity, both a magnitude change (ρ) and phase shift (ϕ) occur during reflection. Equations 2.53 and 2.52 are equivalent to the Fresnel equations [41] for linearly polarized waves.

The multipath model presented here is limited — especially by the smooth surface and flat earth assumptions — but will provide useful results in cases where the underlying assumptions are valid. The extensibility of the simulator software (see Chapter 4) allows more complex models to be included, where necessary.

Polarization and Phase in Multipath Propagation

For the case of linear polarization, the phase, amplitude and polarization effects of reflection off a surface can be expressed in terms of a polarization scattering matrix (see Section 2.2.5 on page 31).

For linear polarization in cases where no depolarization occurs (such as for a smooth sea surface),

$$S = \begin{bmatrix} \Gamma_h & 0 \\ 0 & \Gamma_v \end{bmatrix}. \tag{2.54}$$

For circular polarization the PSM must be transformed using the Jones calculus [42], and S becomes

$$S = \frac{1}{2}\begin{bmatrix} 1 & -j \\ 1 & j \end{bmatrix}\begin{bmatrix} \Gamma_h & 0 \\ 0 & \Gamma_v \end{bmatrix}\begin{bmatrix} 1 & 1 \\ -j & j \end{bmatrix}. \tag{2.55}$$

Where depolarization occurs, the matrix S is not diagonal, and the change in polarization is expressed in the components S_{12} and S_{21}. The simulation

model accepts surface scattering parameters as either a single complex scalar Γ, or the complete PSM for the surface interaction.

Table 2.4: Parameters of multipath simulation surface

Parameter	**Units**
Coefficients of plane equation	m
Roughness factor ($\mathcal{R}$)	
Relative dielectric constant (ϵ), or	
Reflection coefficient (Γ), or	
PSM coefficients	

The parameters for the multipath surface model are listed in Table 2.4. If the dielectric constant is specified, equations 2.52 and 2.53 are used with equation 2.54 to derive the PSM. If a single value of Γ is specified, the PSM

$$S = \begin{bmatrix} \Gamma & 0 \\ 0 & \Gamma \end{bmatrix} \tag{2.56}$$

is used. Coefficients of the plane equation $ax + by + cz = d$ are specified in meters, relative to the centre of the global coordinate system.

2.3 Hardware Model

Modelling the receiver ($R_i(x,t)$) and transmitter ($T_j(x,t)$) effects requires modelling the behaviour of the radar system hardware and the effects of that hardware on the radar signal. The diversity of radar hardware requires that the model be sufficiently flexible to include all relevant effects. For accurate simulation, the performance parameters of the radar hardware under simulation must be mapped onto the model parameters.

2.3.1 The Transmitter Model

The transmitter model, illustrated in figure 2.12, consists of six parts: the signal source, the time and frequency source, the quadrature upmixer, the power amplifier, a bandpass filter, and the transmit antenna.

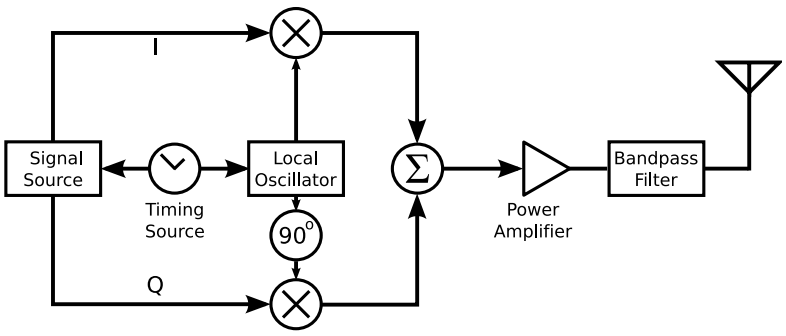

Figure 2.12: Block diagram of the transmitter hardware model

The Signal Source and Quadrature Upmixer

The signal source and quadrature upmixer model the devices in a radar system which generate the signal to be transmitted. The signal source generates the inphase (real) and quadrature (imaginary) parts of the complex envelope $x_l[n]$, samples of the continuous complex envelope $x_l(t)$. The quadrature upmixer mixes this signal up to the transmit frequency.

In many types of radar systems, the output signal $x(t)$ is not generated with a structure similar to that illustrated in figure 2.12. Where these signals can be mathematically represented as bandpass signals, their generation is still adequately represented by figure 2.12 as the signal source and quadrature upmixer together are mathematically equivalent to equation 2.6.

In modern digital radar systems (such as NetRad [75, 76, 77, 78], or HYCAM [79]) the signal source is likely to model a direct digital synthesizer (DDS), or a digital to analogue converter (DAC). For other types of radar systems, the signal source and quadrature upmixer can model a frontend based on magnetrons [80], Klystrons [51], IMPATT oscillators [81, 82], or many other technologies [51].

The effects of local oscillator phase noise on the upmixing process, and of timing source jitter on the signal source are considered in Chapter 3.

The parameters of the signal source are the system sampling frequency (f_s), and the digital samples of the complex envelope of the waveform to be simulated. The parameter of the quadrature upmixer is the local oscillator frequency (f_0). The transmit schedule defines when the transmitter will

transmit.

Time and Frequency Source

The time and frequency source is the source of the transmitter's concept of absolute time, relative time and frequency. The effects of imperfections in the transmitter's concept of time are complex, and are examined in detail in Chapter 3. In addition to modelling the time and frequency references of the transmitter, the timing source controls the transmit schedule, possibly synchronising with receivers or other transmitters in the modelled system.

The parameters of the time and frequency source are the oscillator centre frequency, oscillator phase noise curve, phase offset and frequency offset.

Power Amplifier

The power amplifier models the gain stages in the transmitter. The output of the signal source and upmixer is normalized to the range $[-1, 1]$, and the power amplifier provides the gain necessary to achieve the required transmit power.

The parameters of the power amplifier are the output power, noise temperature [83] and noise bandwidth.

Bandpass Filter

The bandpass filter included before the antenna is not explicitly simulated — it is included in the model to indicate the bandpass nature of the discrete-time simulation model. Physical radar systems are also bandpass in nature, and the simulation sample rate should be chosen to reflect the limited bandwidth of the physical system being simulated.

Antenna

The antenna is modelled as a two dimensional (azimuth and elevation) far field gain pattern. As the simulation does not consider nearfield effects, no details of antenna construction or geometry are required. The phase centre

of the antenna is not specified, as it is assumed to be positioned at the centre point of the platform (see the figure 2.7) to which the transmitter is attached.

Table 2.5: Parameters of the transmitter hardware model

Block	**Parameter**	**Units**
Signal Source	System sample frequency	Hz
	Complex signal envelope	
	Transmit schedule	
Quadrature Upmixer	Local oscillator frequency	Hz
Time and Frequency Source	Ideal centre frequency	Hz
	Phase noise curve	dBc/Hz
	Phase offset	rad
	Frequency offset	Hz
Power Amplifier	Output power	W
	Noise Temperature	K
	Noise Bandwidth	Hz
Antenna	Radiation pattern	dBi
	Loss Factor	
	Polarization	

2.3.2 The Receiver Model

The receiver model, illustrated in figure 2.13, consists of five parts: an antenna, a low noise amplifier, a quadrature downmixer, a time and frequency source, and a signal sink. The parameters of the antenna, quadrature downmixer and time and frequency source are identical to those in the transmitter model.

The parameters of the receiver model are listed in table 2.6, along with the expected units of the parameters.

Low Noise Amplifier

The low noise amplifier models the hardware between the receive antenna and the downmixer. The amplifier is assumed to have flat frequency and phase response, provide gain, and add Gaussian noise to the signal. The parameters of the low noise amplifier are gain and noise temperature.

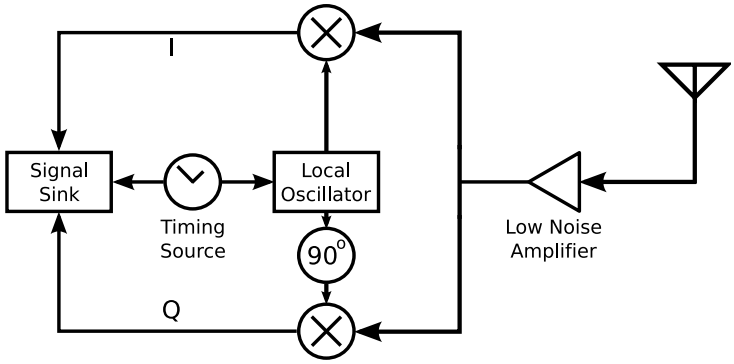

Figure 2.13: Block diagram of the receiver hardware model

Signal Sink

The signal sink models the method used for capturing the signal seen at the receiver. The signal sink does not perform any processing of the captured data except for simulation of signal quantization. The parameters of the signal sink are the system sample frequency, receive schedule, and number of bits in the ADC.

Table 2.6: Parameters of the receiver hardware model

Block	**Parameter**	**Units**
Signal Sink	System sample frequency ADC bits Receive schedule	Hz
Quadrature Downmixer	Local oscillator frequency	Hz
Time and Frequency Source	Ideal centre frequency Phase noise curve Phase offset Frequency offset	Hz dBc/Hz rad Hz
Low Noise Amplifier	Gain Noise Temperature Noise Bandwidth	 K Hz
Antenna	Radiation pattern Loss Factor Polarization	dBi

2.4 Conclusion

A model for the simulation of radar systems has been developed. The goal of the model was to retain as much flexibility as possible, while having sufficient descriptive power to clearly define radar simulation problems. In the interests of simulation flexibility, where particular models (such as the Chi-square RCS variation model in Section 2.2.4) for physical behaviours have been used, the simulation system allows these models to be bypassed or replaced.

The radar simulation model presented here is an hierarchical model (see figure 2.7 on page 23) recognising four physically realizable object types. Each of these object types has a number of parameters which set their properties and behaviour. Of these four object types three (receivers, transmitters and targets) can exist in any number in the simulated environment and one (surfaces) can only have a single embodiment. The simulation model breaks a complex simulation problem down into simpler simulations of monostatic and bistatic radar configurations, through application of the superposition principle.

Implementation of the radar simulation model as a computer program is discussed in Chapter 4.

Chapter 3

Time and Frequency Simulation

3.1 Introduction

The accuracy and precision of time and frequency sources are important parameters in the performance of radar systems. Key radar performance parameters which depend strongly on frequency source performance are range and Doppler accuracy, clutter rejection and processing gain. Examination of these parameters reveals the importance of accurate simulation of the effects of timing and frequency accuracy radar systems.

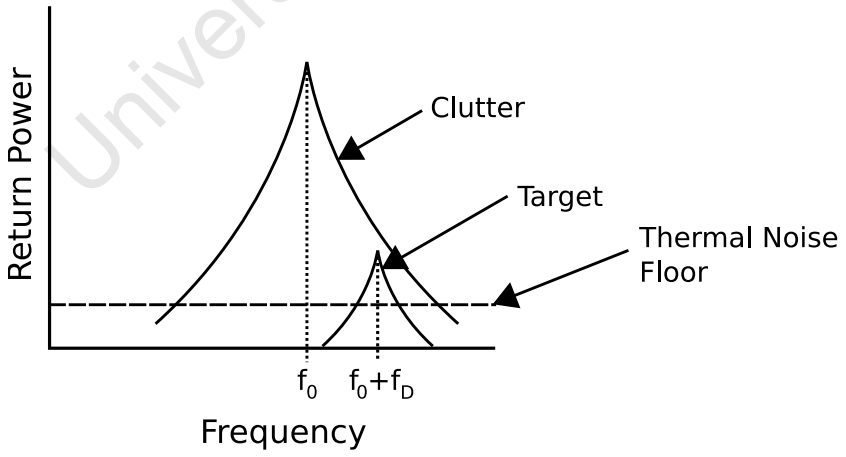

Figure 3.1: Doppler radar sensitivity is limited by clock phase noise where clutter spreading exceeds the system thermal noise floor. Adapted from Leeson et. al. [3]

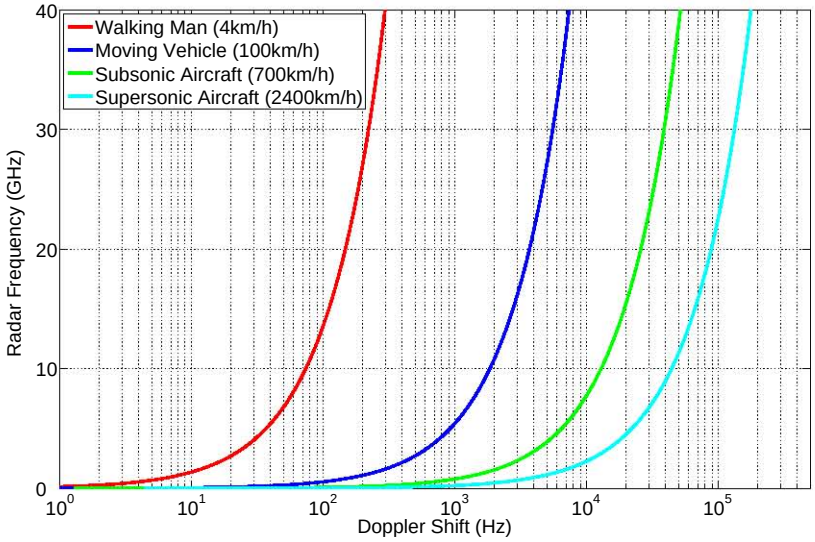

Figure 3.2: Doppler shift of common target types versus system frequency. Adapted from Vig [4]

In Doppler radar, the requirements on oscillator performance are expressed in terms of the power spectral density of the clock output at the Doppler frequencies of interest [3]. The narrower the clock linewidth, the lower the Doppler frequency required for a target to be distinguishable from stationary clutter. In figure 3.1, a target return is present which is visible above the thermal noise floor, but is hidden by widening of the clutter energy caused by clock phase noise.

Doppler frequencies depend on the operating frequency of the radar, and the radial velocity of the target. Figure 3.2 illustrates the Doppler shifts of common target types versus radar frequency. In an X band radar, for example, a walking person would exhibit a maximum Doppler shift of approximately 75Hz.

The accuracy and precision of the frequency source are also important for coherent radar operation. For optimum coherent operation of multistatic radar, the phase of the local oscillator in the receiver must not drift by more than $\frac{\pi}{4}$ radians over the integration time [84] (or $\frac{\pi}{50}$ for optimal performance [85, 48]) . Simulation of clock drift effects is therefore important to the

accurate simulation of the performance of coherent radar systems.

Time and frequency stability, and hence simulation of the effects of instability, is critical in multistatic and netted radar systems. Relative drifts and offsets in the phase and frequency of the timing sources in separate nodes can seriously degrade system performance, and must be included in a simulation of multistatic radar performance.

Timing instabilities can have a significant effect on the performance of netted radar systems. For example, if timing accuracy is sufficient to operate a netted radar system in coherent mode, the system signal to noise ratio increases with the square of the number of nodes [86, 87]. In non-coherent mode, the signal to noise ratio increases linearly with the number of nodes.

3.2 Stochastic Model of Frequency Sources

3.2.1 Definition of the Instantaneous Phase Deviation

An ideal oscillator produces the instantaneous output voltage $V_{ideal}(t)$:

$$V_{ideal}(t) = V_0 \sin(2\pi v_0 t), \tag{3.1}$$

where v_0 is the nominal frequency of the oscillator, and V_0 is the nominal output voltage. In physically realizable systems, several errors reduce the accuracy of the oscillator output — amplitude modulation ($\varepsilon(t)$), phase fluctuations ($\varphi(t)$) and additive noise ($V_1(t)$). Adding these error sources creates a black box [88] model of the expected output of physically realizable timing sources [89, 90, 91, 4]:

$$V(t) = (V_0 + \varepsilon(t)) \sin(2\pi v_0 t + \varphi(t)) + V_1(t). \tag{3.2}$$

In this section, we assume that the additive noise $V_1(t)$, and amplitude modulation $\varepsilon(t)$, are much smaller than the oscillator output voltage V_0, and hence we do not consider these effects.

Using these assumptions, Barnes et. al. [89, 90] define the instantaneous

fractional frequency deviation as

$$y(t) \equiv \frac{1}{2\pi v_0}\frac{d\varphi(t)}{dt}. \tag{3.3}$$

As the instantaneous frequency deviation of a timing source cannot be directly measured, the instantaneous time (or phase) deviation is used. Allan [92] defines the instantaneous time deviation function as:

$$x(t) \equiv \frac{\varphi(t)}{2\pi v_0}, \tag{3.4}$$

where:

$$x(t) = \int_0^t y(x)dx. \tag{3.5}$$

The complete simplified model of clock output, including phase and frequency deviations, is therefore defined to be:

$$V(t) = V_0 \sin(2\pi v_0(t + x_d(t) + x_r(t))), \tag{3.6}$$

where $x_d(t)$ and $x_r(t)$ are the deterministic and random components of the instantaneous time deviation $x(t)$.

3.2.2 Characterization of the Instantaneous Phase Deviation

The instantaneous time deviation function $x(t)$ can be considered to be the sum of two functions — deterministic and systematic errors $x_d(t)$ and random fluctuations $x_r(t)$. Modelling of the deterministic and systematic component of $x(t)$ is fairly straightforward, and will be considered in Section 3.2.3. Modelling of the random part of $x(t)$ is more complex, however, and will be discussed in depth.

Frequency Domain Characterization

Frequency domain classification of the phase deviation of an oscillator is typically performed using the power spectral densities (PSDs) of $x(t)$ and

$y(t)$, denoted as $S_x(f)$ and $S_y(f)$. For many types of precision oscillators, $S_y(f)$ can be approximated by a power law model [91]:

$$S_y(f) = \sum h_\alpha f^\alpha \quad \text{Hz}^2/\text{Hz}, \tag{3.7}$$

where f^α is the noise category, and h_α is the intensity coefficient in that category. From equations 3.5 and 3.7, the PSD of $x(t)$ can be written [93] as:

$$S_x(f) = \frac{S_y(f)}{(2\pi f)^2} = \sum \frac{h_\alpha}{4\pi^2} f^{\alpha-2} \tag{3.8}$$

Five categories of noise, corresponding to integer values of α in equation 3.7, are typically used for the analysis of phase deviation in the frequency domain. These categories are white phase modulation ($\alpha = 2$), flicker phase modulation ($\alpha = 1$), white frequency modulation ($\alpha = 0$), flicker frequency modulation ($\alpha = -1$) and random walk frequency modulation ($\alpha = -2$). Figure 3.4 on page 49 shows examples of $x(t)$ for each noise category.

Considering only the noise categories typically found in frequency sources [94, 95, 89], a complete frequency domain noise measure can be expressed as:

$$S_x(f) = \sum_{\alpha=-2}^{2} \frac{h_\alpha}{4\pi^2} f^{\alpha-2} \tag{3.9}$$

The phase noise figure $L(f)$ is typically specified on the data sheets of precision oscillators. The definition of $L(f)$ [96, 97] is:

$$L(f) = 10 \log_{10}(\frac{1}{2} S_x(f)) \quad \text{dBc/Hz}. \tag{3.10}$$

Some devices specify the complete curve of $L(f)$, and some specify only values of $L(f)$ at certain offset frequencies. $L(f)$ is the IEEE1139-1999 standard [96] frequency domain measure of oscillator stability. Figure 3.3 illustrates $L(f)$ specifications for two quartz crystal oscillators — a Wenzel oven controlled crystal oscillator (OCXO) [98], and a low cost Maxim temperature compensated crystal oscillator (TCXO) [8]. For comparison, requirements of oscillator phase noise levels for airborne Doppler radars are typically -110dBc/Hz [3]

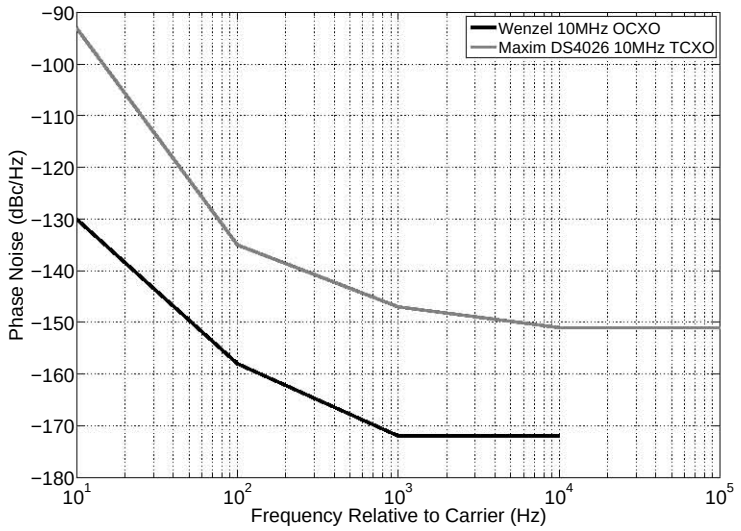

Figure 3.3: Comparison of specified phase noise measurements from two quartz oscillators

or less.

The use of a power law model of $S_x(f)$ with $\alpha < 0$ implies that the mean square values of $x(t)$ and $y(t)$ are unbounded [88]:

$$\lim_{f \to 0} S_x(f) \to \infty, \tag{3.11}$$

and the PSD of $x(t)$ and $y(t)$ are unbounded (except for $\alpha = 2$). The stochastic processes $x(t)$ and $y(t)$ are therefore long-range dependent [99, 100]. While the process which generates $x(t)$ and $y(t)$ is not wide-sense stationary, as the PSD is unbounded [101, 60], any finite length sample of $x(t)$ or $y(t)$ is stationary and has a bounded PSD and finite energy.

Time Domain Characterization

Equation 3.11 implies that the standard variances σ^2 of the instantaneous frequency ($y(t)$) and phase ($x(t)$) functions are unbounded, and therefore cannot be applied to the characterization and measurement of clock instability.

The most common measure used for time-domain characterization of clock

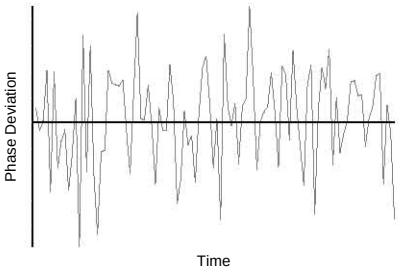

(a) White phase modulation

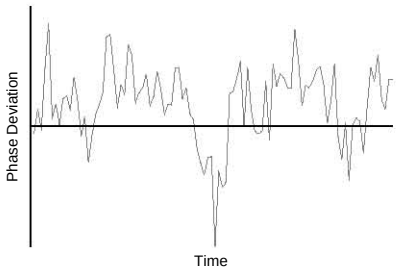

(b) Flicker phase modulation

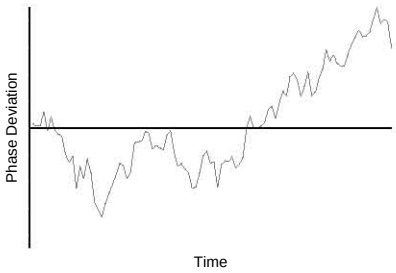

(c) White frequency modulation

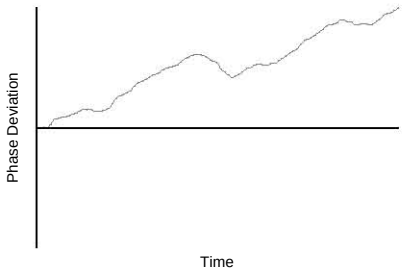

(d) Flicker frequency modulation

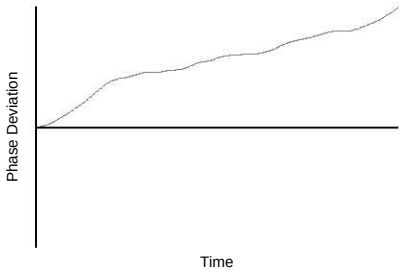

(e) Random walk frequency modulation

Figure 3.4: Examples of categories of phase noise, corresponding to power law spectra of $S_x(f)$

instability is the two-sample, or Allan, variance. In discrete sampled systems, the two-sample variance is defined as the dimensionless number [102, 103]

$$\sigma_y^2(\tau) = \lim_{N\to\infty} \frac{1}{N} \sum_{n=1}^{N} \frac{(x_n - 2x_{n-1} + x_{n-2})^2}{2\tau^2} \tag{3.12}$$

where $x_n = x(n\tau_0)$ and τ_0 is the system sample rate. Where only finite numbers of data points are available, the Allan variance can be estimated as

$$\hat{\sigma}_y^2(\tau) = \frac{1}{N-2m} \sum_{n=1}^{N-2} \frac{(x_{n+2m} - 2x_{n+m} + x_n)^2}{2m^2\tau_0^2}, \tag{3.13}$$

where $\tau = m\tau_0$, τ_0 is the system sample rate, and N data points are available. In bandlimited systems, the Allan variance is known to converge for all $\alpha > -3$.

The Allan variance is useful for characterization of noise as $\sigma_y^2(\tau) \sim \tau^{-\alpha-1}$ for $-3 < \alpha \leq 1$ [104]. Thus, the Allan variance can be used to estimate both the intensity and power spectral density of noise.

The characterization power of the Allan variance is limited by an ambiguity where $\alpha \geq 1$ — it cannot differentiate between white phase modulation (PM) and flicker PM noise. This shortcoming is addressed by the modified Allan variance [104], which is defined as:

$$\text{Mod } \sigma_y^2(\tau) = \frac{1}{2\tau^2} \left\langle \left(\frac{1}{n} \sum_{i=1}^{n} (x_{i+2n} - 2x_{i+n} + x_i) \right)^2 \right\rangle, \tag{3.14}$$

where $\tau = n\tau_0$ and $\langle x \rangle$ is the infinite ensemble average of x. For a finite data set of N points, Mod $\sigma_y^2(\tau)$ can be estimated as:

$$\text{Mod } \hat{\sigma}_y^2(\tau) = \frac{1}{2\tau^2 n^2 (N-3n+1)} \sum_{j=1}^{N-3n+1} \left(\sum_{i=j}^{n+j-1} (x_{i+2n} - 2x_{i+n} + x_i) \right)^2. \tag{3.15}$$

For the modified Allan variance, Mod $\sigma_y^2(\tau) \sim \tau^{-\alpha-1}$ for $-3 < \alpha < 3$. The modified Allan variance can therefore be used to characterize any of the five common types of noise, but at a greater computational cost than the

Allan variance.

For long averaging times the total variance measure [105, 106] is a superior measure of oscillator statistics than estimates of the Allan variance (equation 3.13) . The definition of this measure is similar to the Allan variance, but operates on a synthetically lengthened sample sequence:

$$\text{Totvar}(\tau) = \frac{1}{2\tau^2(N-2)} \sum_{n=2}^{N-1} \left(x^{\#}_{n-m} - 2x^{\#}_{n} + x^{\#}_{n+m} \right)^2 . \tag{3.16}$$

For $n = 1$ to N, $x^{\#}_n = x_n$ and for $j = 1$ to $N-2$, $x^{\#}_{1-j} = 2x_1 - x_{1+j}$, and $x^{\#}_{N+j} = 2x_N - x_{N-j}$.

For Totvar(τ), white and flicker phase modulations produce slopes of τ^-1; white frequency modulation (FM), flicker FM and random walk FM correspond to $\tau^{-\frac{1}{2}}$, τ^0 and $\tau^{\frac{1}{2}}$, respectively [105].

Relationship Between Time and Frequency Measures

An integral relationship exists between the PSD and the Allan variance [94, 107]:

$$\sigma_y^2(\tau) = \frac{8}{\tau^2} \int_0^\infty S_x(f) \sin^4(\pi\tau f) df, \tag{3.17}$$

however, this relationship is not easily calculated. Simplification of this relationship can be performed using the model expressed in equation 3.9. The contribution of each term in the summation can be considered independently, greatly simplifying the calculation of $\sigma_y^2(\tau)$ from $S_y(f)$ or $S_x(f)$. The contribution of each term is presented in the following table (from [90]), where f_h is the upper frequency limit of the measurement system, and γ is the Euler-Mascheroni constant ($\gamma \simeq 0.57722$).

Noise Category	**Contribution to $\sigma_y^2(\tau)$**
White PM	$h_2 \frac{3f_h}{(2\pi)^2\tau^2}$
Flicker PM	$\frac{h_1}{(2\pi)^2\tau^2} \left(3\left[\gamma + \ln(2\pi f_h \tau)\right] - \ln(2)\right)$
White FM	$\frac{h_0}{2}\lvert\tau\rvert^{-1}$
Flicker FM	$2h_{-1}\ln(2)$
Random Walk FM	$\frac{h_{-2}}{6}(2\pi)^2\lvert\tau\rvert$

The Allan variance $\sigma_y^2(\tau)$ can't be unambiguously mapped onto $S_x(f)$ (or $S_y(f)$), even for $-3 < \alpha \leq 1$. Greenhall [107] examines the limitations on the mapping of the Allan variance onto $S_x(f)$. Due to this limitation, it is more convenient to specify a simulation model of stochastic oscillator behaviour in terms of the unambiguous PSDs $S_x(f)$ or $S_y(f)$, than the Allan variance.

3.2.3 Modelling of Deterministic Phase Deviation

Many common types of oscillators exhibit systematic and deterministic deviations from the expected phase in addition to the stochastic phase deviation. When applying simplified models (such as equation 3.9) to the random part of the phase deviation, accuracy can be improved by considering deterministic errors separately.

Environmental Effects

A key source of systematic errors on frequency source outputs is environmental factors. A large number of such factors exist, including ambient temperature, vibration, power supply noise, radio frequency (RF) noise picked up from the environment, vibrations and many others. Many of these factors are strongly periodic — such as 100Hz for power supply noise, and daily and yearly periods for temperature effects.

Periodic environmental effects can be added to the frequency domain model of phase deviation. Considering each environmental factor i to have amplitude a_i and period T_i, then the equation 3.7 can be modified to include periodic environmental factors:

$$S_y(f) = \sum_{\alpha} h_\alpha f^\alpha + \sum_i a_i \frac{1}{T_i}. \tag{3.18}$$

Similarly, periodic environmental factors can be included in the instantaneous phase deviation (equation 3.5) as periodic components:

$$x_d(t) \equiv \frac{1}{v_0} \sum_i \left(a_i t \sin\left(2\pi t \frac{1}{T_i} \right) \right) \tag{3.19}$$

Offsets, Drift and Aging

In addition to periodic effects, frequency sources often exhibit other deterministic behaviours, such as a constant frequency offset, linear drift, and aging related behaviours.

Offset is a systematic inaccuracy in the output frequency of an oscillator, which does not effect the precision of the oscillator and *drift* is the time dependent systematic change in frequency of an oscillator [4]. Combining drift with a frequency offset yields the drift function $d(t)$, which is included in the oscillator model (equation 3.2) as follows:

$$V(t) = (V_0 + \varepsilon(t)) \sin\left(2\pi(v_0 + d(t))t + \varphi(t)\right) + V_1(t). \tag{3.20}$$

Considering only linear drift and constant offset allows the definition of the drift function as $d(t) = \Delta v + v_{drift}t$, where Δt is the frequency offset and v_{drift} is the frequency drift per unit time. Using this definition, drift and offset can be included in the definition of instantaneous frequency deviation (equation 3.3) to form:

$$y(t) \equiv \frac{1}{v_0}\left(\Delta v + v_{drift}t + \frac{1}{2\pi}\frac{d\varphi(t)}{dt}\right). \tag{3.21}$$

Combining the offset and drift factors with the periodic components of $x_d(t)$ (equation 3.19) yields:

$$x_d(t) \equiv \frac{1}{v_0}\left(\Delta v t + v_{drift}t^2 + \sum_i \left(a_i t \sin\left(2\pi t \frac{1}{T_i}\right)\right)\right). \tag{3.22}$$

3.2.4 Timing Jitter

When considering a digital waveform, jitter is the short-term variation in the timing of *significant events* (such as edges), compared to the ideal timing of these events [5]. In this definition, short-term is commonly considered to refer to events with a frequency greater than 10Hz [108]. Jitter is typically measured in one of three ways, as illustrated in figure 3.5: period jitter, cycle to cycle jitter and time interval error (TIE). Period jitter is the random

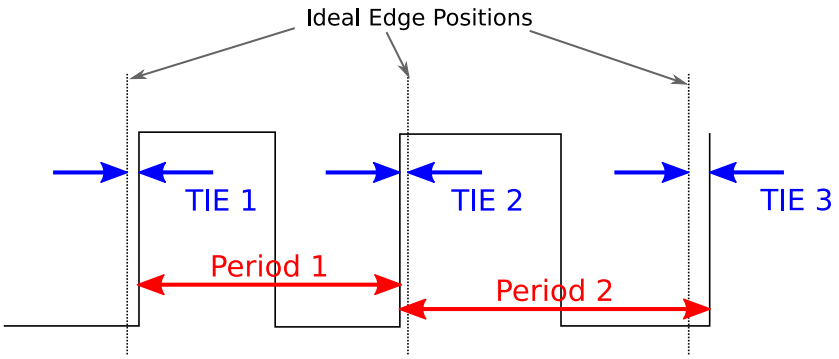

Figure 3.5: Definition of Period Jitter and Time Interval Error (after [5])

deviation of the length of each period of the waveform, cycle to cycle jitter is the random deviation in the length of each pair of adjacent cycles, and time interval error is the deviation of the position of edges from their ideal positions. Period jitter sample N is related to cycle to cycle jitter sample N by:

$$C_N = P_N - P_{N-1} \tag{3.23}$$

and to the TIE at period N by:

$$TIE_N = \sum_{i=0}^{N} \left(P_N - P_{ideal} \right), \tag{3.24}$$

where P_{ideal} is the ideal period.

The jitter on a digital clock signal derived from an oscillator with phase noise can be calculated by integrating the phase noise spectrum over the frequency band of interest [109]. Typically, the lowest frequency of interest is 10Hz, and the highest frequency of interest is $2f_0$, where f_0 is the oscillator frequency [110]. From the definition of $L(f)$ (equation 3.10), the time interval error noise power can be estimated by:

$$J = \int_{10\text{Hz}}^{2f_0\text{Hz}} L(f) df. \tag{3.25}$$

The estimated RMS jitter is therefore [110]:

$$J_{RMS} = \frac{\sqrt{2}\sqrt{10^{J/10}}}{2\pi f_0} \quad \text{seconds.} \tag{3.26}$$

3.3 Generation of Synthetic Phase Noise Sequences

Generation of synthetic clock signals for computer simulation requires calculation of the deterministic phase deviation $x_d(t)$, and generation of a synthetic noise sequence matching the statistical properties of the random phase deviation $x_r(t)$.

Calculation of $x_d(t)$ is straightforward, and can be performed directly using equation 3.22. The synthesis of $x_r(t)$ matching the required PSD and statistical properties is more complex, especially where large numbers of samples are required.

For computer simulation, a discrete representation of $x_r(t)$, which will be called $x_r[n]$, must be used. In this model, $x_r[n]$ will be considered a discrete representation of a version of $x_r(t)$ strictly bandlimited to $\frac{f_0}{2}$Hz, where f_0 is the system sample frequency. Using a strictly bandlimited $x_r(t)$ allows the model to ignore the effects of aliasing [102] of the higher frequency components of $x_r(t)$ on the spectral density of $x_n[t]$.

3.3.1 Power Law Noise Model

Equation 3.8 defines a power-law PSD model for $x_r(t)$. An explicit distinction must be made between random numbers with a power law distribution (that is, a probability density function (PDF) of the form $p(x) \propto x^{-\alpha}$), and random numbers with a power law power spectral density (such as those defined by equation 3.8) — this section is concerned with the latter. To avoid confusion, we will refer to the noise types of interest as $1/f$ noise, for all α.

3.3.2 Autocorrelation

The discrete Einstein-Wiener-Khinchine [111, 60] theorem relates the autocorrelation sequence $\phi_{xx}[n]$ of the samples $x[n]$ to the PSD $S_x[f]$ of those samples:

$$\phi_{xx}[n] = \frac{1}{N} \sum_{f=0}^{N-1} S_x[f] \exp\left(\frac{1}{n} 2j\pi f N\right) \tag{3.27}$$

By the localisation property of the discrete Fourier transform [29], the autocorrelation $\phi_{xx}[n]$ tends to spread as the PSD $S_x[f]$ becomes more compact. Following this observation, it is clear that for noise matching the PSD in equation 3.8 will have a wide spread autocorrelation where $\alpha \leq 1$ due to the strongly compact nature of the PSD. As $x(f)$ is long-range dependent [100] (see Section 3.2.2),

$$\sum_{n=1}^{\infty} |\phi_{xx}[n]| = \infty. \tag{3.28}$$

Categorising phase noise as a long-range dependent process adds the requirement of a long memory to processes which produce noise of this type. Long-term autocorrelation also implies that phase noise correlations may exist between radar pulses — these correlations must be preserved for accurate simulation.

3.3.3 Existing Approaches to $1/f$ Synthesis

Techniques for the digital synthesis of $1/f$ noise samples are well described in literature. Available techniques can be divided into two categories: exact and inexact. Exact generation techniques, where no systematic deviation is allowed from the required spectrum, include fast Fourier transform (FFT) based methods [112, 113] and time-domain filtering of discrete Poisson events [114]. Inexact synthesis methods, where some ripple or error is permissible in the noise PSD, include cascaded infinite impulse response (IIR) filters [115], cellular automata [116], iterated function systems [117], truncated autoregressive (AR) filters [113], Wavelets [118, 119, 120] and others.

The requirements for noise synthesis for radar simulation include the ability to generate noise sequences for all $2 \leq \alpha \leq -2$, computational efficiency,

memory efficiency and accuracy. Radar simulations require large volumes of random samples to be generated, and algorithms must be chosen which are suitable for this use.

3.3.4 Synthesis Using Time Domain Filtering

In general, it is not possible to filter a sequence of samples using a finite length digital filter to produce an exact $1/f$ response [113]. It is not possible, therefore, to apply a filter of shorter than N samples to produce the desired N samples of the $1/f$ noise process.

The processing of N samples with an N tap filter can be performed in $O(N \log N)$ time, using the FFT [112, 113] provided N is known. If N is not known, filtering must be performed in the time domain, requiring $O(N^2)$ operations and $O(N)$ memory. For large radar simulation problems, the requirement of $O(N)$ memory for N noise samples is likely to be restrictive, and alternate approaches which do not require storage of all noise samples must be sought.

In the generation of noise for radar simulation some ripple, provided it is sufficiently small, can be allowed in the $1/f$ PSD of the generated samples. Relaxing the requirement for exact synthesis allows implementation of time domain filtering with filters shorter than N.

Truncation of Exact Filters

The transfer function of an ideal filter for the generation of $1/f$ noise is [121]:

$$H(z) = \frac{1}{(1 - z^{-1})^{(-\alpha+2)/2}}. \tag{3.29}$$

From this relation, it is clear that trivial filters can be derived using the inverse z-transform [29] for $\alpha = 2$, $\alpha = 0$ and $\alpha = -2$. For $\alpha = 0$, the required filter is an ideal integrator, and for $\alpha = -2$ it is a cascade of two ideal integrators.

Where α does not take on one of these convenient values, the M coefficients for an exact autoregressive (AR) filter for $M = N$ can be derived

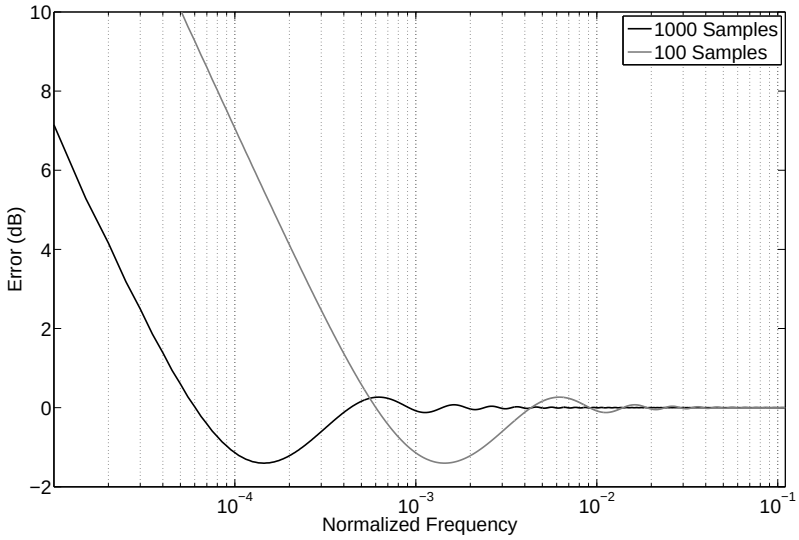

Figure 3.6: Deviation of truncated filters from the target response for $N = 10^5$ and $\alpha = 1$ (from [6])

from equation 3.29 [113]:

$$a_0 = 1 \text{ and}$$
$$a_k = \left(k - 1 - \frac{-\alpha + 2}{2}\right) \frac{a_{k-1}}{k}. \tag{3.30}$$

An approximation of the exact roll-off is produced where $M < N$. The PSD of the noise generated using such a truncated filter matches the required slopes at high frequencies but has a flat spectrum at low frequencies. The roll-off between the required slopes and flat response depends on M and α [6], but occurs at approximately $\omega = \frac{2\pi}{M}$.

Figure 3.6 illustrates the deviation from the required response for two truncated filters for $\alpha = 1$ generated using equation 3.30. Errors are well constrained for $\omega > \frac{2\pi}{M}$, but increase at approximately 3dB per octave at lower frequencies.

While equation 3.30 produces ideal filters for $M = N$, the filters produced for $M < N$ do not produce optimal results for a filter of length M. For example, a numerically designed third order IIR filter for $\alpha = 1$ (due to Bristow-Johnson [122]) can match the required roll-off within 0.3dB over ten

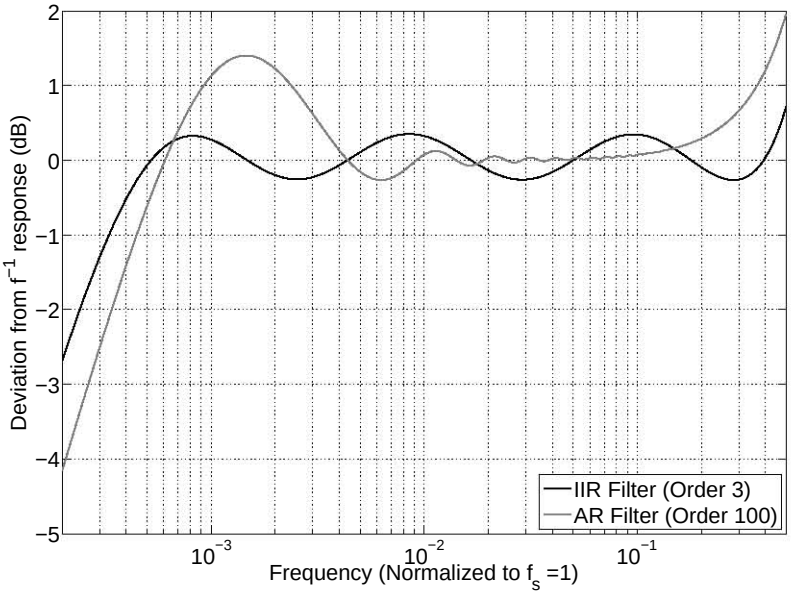

Figure 3.7: Comparison of deviations from the exact response of an optimal IIR filter, and an AR filter designed using equation 3.30 (from [6])

octaves [122]. Figure 3.7 compares a hand designed order three filter for $\alpha = 1$ with an order 100 filter designed using equation 3.30.

Filter Design Using Optimization Techniques

A variety of optimisation based design techniques exist, aimed at the direct design of digital (both finite impulse response (FIR) and IIR) filters approaching a desired response. These approaches can be divided into two categories: least-squares optimisation, and Chebyshev optimisation.

Least-squares optimisation approaches aim to design a filter with a chosen number of coefficients which approaches the target response in the least squares sense. That is, they aim to find a rational transfer function $H(z)$ which minimises the value of S, where

$$S = \frac{1}{2\pi} \int_0^{2\pi} \left(H_t(e^{j\omega}) - H(e^{j\omega}) \right)^2 d\omega, \tag{3.31}$$

and $H_t(z)$ is the desired transfer function. One optimisation method of

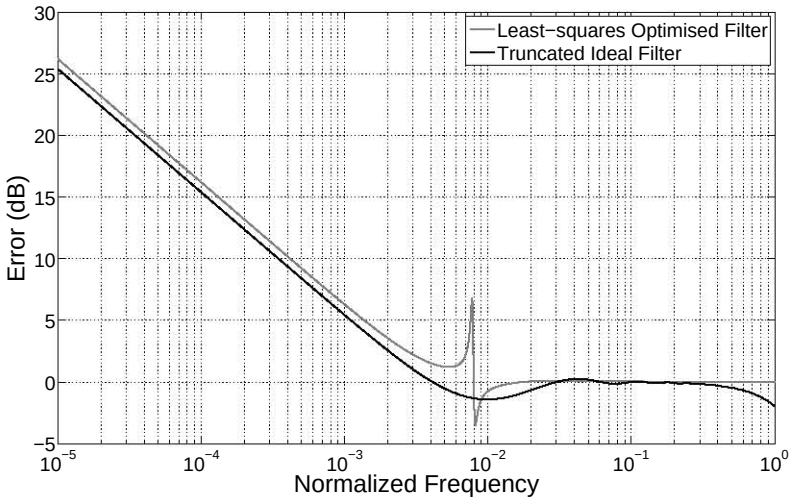

Figure 3.8: Comparison of deviation from $\alpha = 1$ response for least-squares optimal filter and truncated ideal filter (order = 30)

this kind, the modified Yule-Walker [123] method, is very widely used and implemented.

Despite its wide applicability to filter design problems, least squares optimisation is not suited to finding filters with $1/f$ type responses. Optimisation of S (equation 3.31) will find filters which closely match the required response for high frequencies, but like the truncated ideal filters, they do not match the required roll-off at low frequencies. This is because the width of the low frequency error is fairly low, and it has less effect on least-squares error than ripple at higher frequencies. Figure 3.8 compares the performance of an order 30 filter designed using the Yule-Walker least-squares optimisation procedure, and the order 30 truncation of the ideal filter for $\alpha = 1$. In this case, the least-squares designed filter performs better than the truncated filter at high frequencies.

Filter design using Chebyshev norm optimisation (also known as minimax optimisation and l_∞ optimisation) seeks to find the rational transfer function $H(z)$ which minimizes [124]

$$\|H(e^{j\omega}) - H_t(e^{\omega})\| = \max_{0 \leq \omega \leq 2\pi} |H(e^{j\omega}) - H_t(e^{j\omega})|, \tag{3.32}$$

where $H_t(z)$ is the required transfer function. That is, this procedure seeks to find the filter which minimizes the maximum deviation, at the cost of increased least-squares error [125].

Chebyshev optimal filter design is not as widely used as least-squares filter design, but has been extensively developed for cases where minimax optimisation is required. Available algorithms for Chebyshev optimisation include those based linear programming [126, 127], linear programming with differential correction [128, 129], the rational Remez exchange algorithm [124], eigenvalue decomposition [130, 131], and others.

Time domain filtering approaches are suitable for the efficient approximation of $1/f$ noise sequences for radar simulation. The design of filters for odd (and non-integer) α is challenging, and requires compromise between filter length, minimax error and least-squares error. Chebyshev optimal filters reduce error close to the carrier, but tend to introduce unacceptable deviations from the required response at higher frequencies. Least-squares optimal and truncated ideal filters match the required roll-off closely at high frequencies, at the cost of a flat response at low frequencies and truncation of the noise autocorrelation sequence.

3.4 Multirate Filters and Noise Generation

The time domain filtering technique is the most promising for the generation of synthetic phase noise sequences for radar simulation. The shortcomings of this technique, namely the difficulty of filter design and truncation of autocorrelation sequences, can be addressed by using multirate signal processing techniques.

3.4.1 Overview of Multirate Signal Processing

Multirate signal processing refers to digital signal processing performed with a set of operations including the compression and expansion operations, in addition to the operations used in single rate digital signal processing (DSP) [29]. The compression (also widely referred to as decimation) operation,

typically written as $\downarrow k$ for integer k, corresponds to the creation of a signal which contains every kth sample of the original signal [132, 133]. Where $y[m]$ is $x[n]$ compressed by the factor k,

$$y[m] = x[nk]. \tag{3.33}$$

The expansion operation, typically written as $\uparrow k$ for integer k, corresponds to the creation of a signal, every kth sample of which is a sample of the original signal [132], and the rest are zero. Where $y[n]$ is $x[n]$ expanded by the factor k,

$$y[m] = \begin{cases} x[\frac{m}{k}] & \frac{m}{k} \in \mathbb{Z}, \\ 0 & \text{otherwise.} \end{cases} \tag{3.34}$$

The *upsampling* operation is related to the expansion operation, by the use of a suitable filter for rejecting the images of $x[n]$ in the frequency domain introduced by expansion. The *downsampling* operation is related to compression, by the use of a suitable anti-aliasing filter to remove all frequencies of $x[n]$ above $\frac{1}{k}$ times the sampling rate of $x[n]$. The *resampling* operation by the rational factor $\frac{a}{b}$ corresponds to upsampling by a, followed by downsampling by b.

3.4.2 Multirate Filterbanks for $1/f$ Noise

Examination of figure 3.8 on page 60 reveals that the least-squares optimal filter for $\alpha = 1$ designed using the modified Yule-Walker [123] algorithm closely matches the required response over the top decade of frequency (that is, from $\frac{1}{2}f_s$ to $\frac{1}{10}f_s$). Figure 3.9 shows that the maximum deviation from the required response in this range for an order 10 least-squares IIR filter is less than 0.05dB.

Based on the observation that standard filter design procedures can accurately match the required response over a single decade of frequency, it can be hypothesised that a filter $Y(\omega)$ exists with similarly low ripple, made up of filters $G_i(\omega)$ which match the required roll-off in the ith decade and

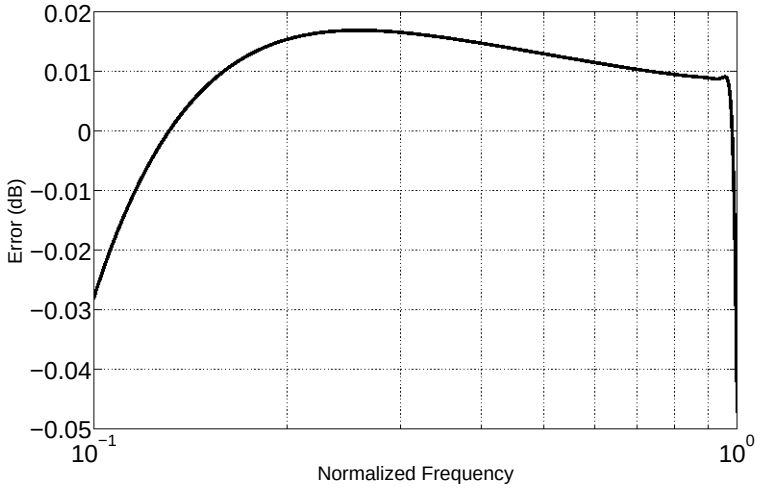

Figure 3.9: Deviation from $\alpha = 1$ response for least-squares optimal filter over the top decade of frequency (order = 10)

ideal bandpass filters $B_i(\omega)$, which select that decade:

$$Y(\omega) = \sum_{i=1}^{\infty} B_i(\omega) G_i(\omega). \tag{3.35}$$

Such a filter would not be practically realizable, as it requires an infinite sequence of subfilters and ideal bandpass filters. The decades of frequency below a particular limit can be discarded, as radar simulations are unlikely to be interested in phase noise periods in the order of centuries. Selecting D decades of frequency:

$$Y(\omega) = \sum_{i=1}^{D} B_i(\omega) G_i(\omega). \tag{3.36}$$

$Y(\omega)$ could be physically realised using the structure shown in figure 3.10. In this structure $y[n]$ are the simulated phase noise samples, and $g[n]$ are independent white Gaussian noise samples. Simplification of this structure, and application of multirate signal processing techniques, allows an approximation to the ideal filter $Y(\omega)$ to be implemented computationally efficiently.

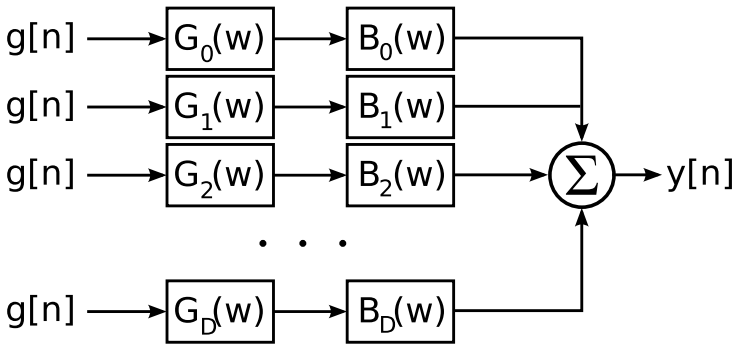

Figure 3.10: Filter structure for $Y(\omega)$

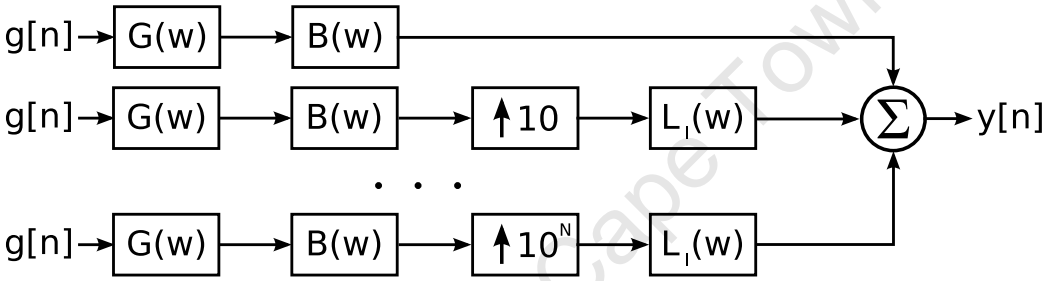

Figure 3.11: Simple multirate implementation of filter structure for $Y(\omega)$

Multirate Implementation of $Y(\omega)$

The ideal time-domain noise filter $Y(\omega)$ is ideally suited to implementation as a multirate filterbank. The top subband $B_0(\omega)$ $G_0(\omega)$ has only slightly less bandwidth than the whole system, so it must be run at the system sample rate f_0. The next subband has ten times less bandwith, and therefore can be run at a tenth of the sample rate and so on. In addition, the ideal bandpass filter $B_i(w)$ can be divided into two sections, a lowpass $L_i(\omega)$ and a highpass $H_i(\omega)$.

Executing each branch of the filter structure (figure 3.10) at sample rate suitable for its bandwidth has several advantages. If branches are spaced decades of frequency apart, and the sample rate in each branch is ten times lower than the next branch up, the same filters $G(\omega)$ and $B(\omega)$ can be used in each branch.

Figure 3.11 illustrates a simple adaptation of the structure in figure 3.10

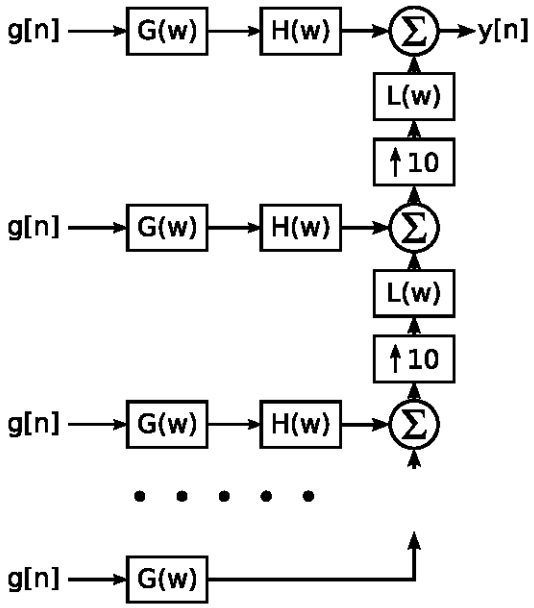

Figure 3.12: Optimised multirate implementation of filter structure for $Y(\omega)$ (Adapted from Park et. al. [7])

to use multirate signal processing principles. In this figure $\uparrow N$ corresponds to expansion by a factor of N, and $L_i(\omega)$ in an anti-imaging (interpolation) filter suitable for the upsampling operation. This structure can be further re-arranged to increase efficiency [7] by reducing the number of filtering operations required in each branch and the number of operations performed at the full rate.

Figure 3.12 illustrates an optimised structure for the implementation of $Y(\omega)$. In this structure, the bandpass filter $B(\omega)$ has been divided into highpass ($H(\omega)$) and lowpass ($L(\omega)$) sections. The lowpass sections have been combined with the anti-imaging (interpolation) filters for each branch, reducing the number of filtering operations required. In addition, the filters used for each branch are identical — only one set of filter designs is required.

For optimal performance of the structure in figure 3.12, the filters $H(\omega)$ and $L(\omega)$ must have narrow transition bandwidths, adequate stopband attenuation, and a flat (within reasonable bounds) summed response. The design of pairs of filters with the required specifications is well understood [133, 132] and can

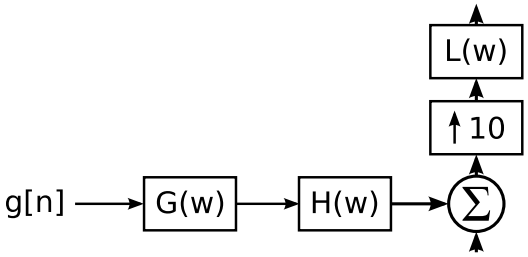

Figure 3.13: A single branch of the optimised multirate filter structure for $Y(\omega)$

be performed with standard filter design techniques. Elliptic [29, 134] filters are ideal for this purpose, as ripple can be tolerated in both the passband and stopband.

3.4.3 Computational Efficiency

The computational requirements of a single branch (figure 3.13) of the multirate filter structure for noise generation (figure 3.12) can be computed by adding up the individual computational requirements of each element. The branch includes two filters operating at the branch's sample rate, and one at ten times that rate. The summation and upsampling operations are also included.

Assuming that the three filters $G(\omega)$, $H(\omega)$ and $L(\omega)$ are implemented as direct form II [29] IIR filters with order N, each sample passed through these filters will require $2N + 1$ multiplications, $2N$ additions and N memory slots [27]. The filter $L(\omega)$ is clocked at ten times the rate, and hence will require $20N + 10$ multiplications and $20N$ additions for each noise sample produced by the branch. Expansion is a simple padding operation, and does not require any calculations. The total number of calculations for C required for each branch is $C = 4N_G + 4N_H + 40N_L + 12$ for each sample, where N_G, N_H and N_L are the orders of $G(\omega)$, $H(\omega)$ and $L(\omega)$ respectively. The highest rate branch does not require $L(\omega)$, and hence requires $C = 4N_G + 4N_H + 2$ calculations.

For each sample produced by the complete structure with D branches,

the number of calculations required is

$$C_t = 4\left(N_G + N_H + \sum_{i=1}^{D} \frac{1}{10^i}\left(N_G + N_H + 10N_L + 12\right)\right). \tag{3.37}$$

Choosing $N = \max\{N_H, N_G, N_L\}$, the upper bound of

$$C_u = 4\left(2N + (12N + 13)\sum_{i=1}^{D} \frac{1}{10^i}\right) = \frac{1}{9}\left(120N + 48\right) \tag{3.38}$$

is set.

If a single IIR filter with the required response and order M were to exist, producing each sample with such a filter would require $2M + 1$ calculations. The multirate filter bank is therefore more efficient when $M > \frac{1}{18}\left(120N + 48\right) + 1$. For example, for $N = 30$ the multirate structure is more efficient where $M \geq 204$ — and, as Section 3.3.4 discusses, no filter with such a short length is possible for most values of α over more than a few decades of frequency.

3.4.4 Accuracy

The accuracy of fit of the PSD of the noise generated using the multirate approach depends on the performance of the filters in the multirate filterbank. Specifically, the accuracy of the slope of the generated noise PSD depends on how well $G(\omega)$ matches the required slopes over the top decade of frequency. Deviations from perfect reconstruction in the filter pair $H(\omega)$ and $L(\omega)$ will cause ripple on decade boundaries. Passband ripple on $H(\omega)$ and $L(\omega)$ will produce ripple on the produced PSD, and insufficient stopband attenuation in these filters will allow the behaviour of $G(\omega)$ outside the band of interest to reduce the accuracy of the required estimate.

Figure 3.14 shows the performance of the filterbank for various α, estimated using the FFT and averaged over 100 runs to reduce the variance. For $G(\omega)$, an 11th order IIR filter designed using the modified Yule-Walker [123] algorithm was used. For $H(\omega)$ and $L(\omega)$, a pair of 11th order Elliptic (Cauer) filters [135, 27] was used.

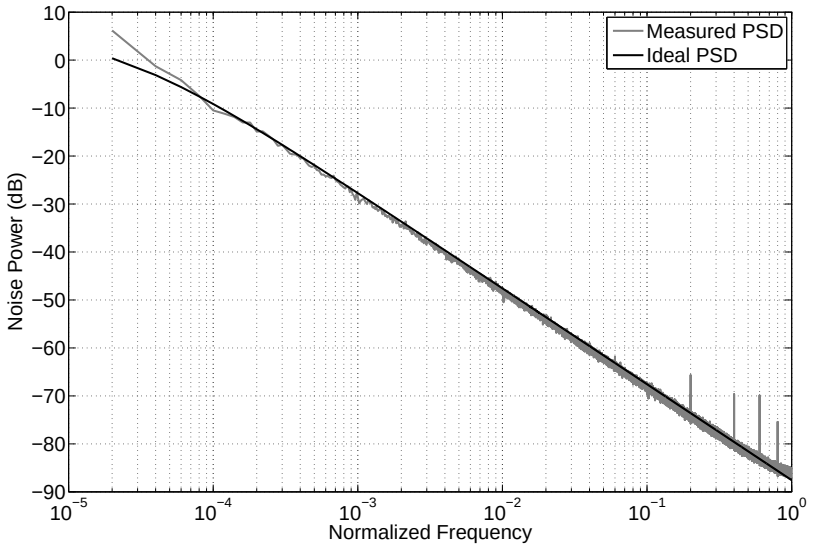

(a) $\alpha = 0$

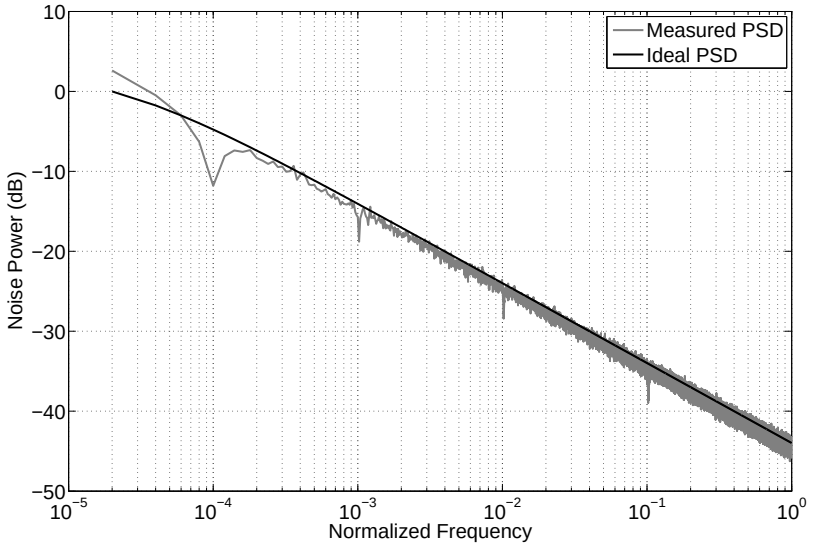

(b) $\alpha = 1$

Figure 3.14: Comparison of generated noise PSD versus required PSD for two coloured pseudonoise sequences

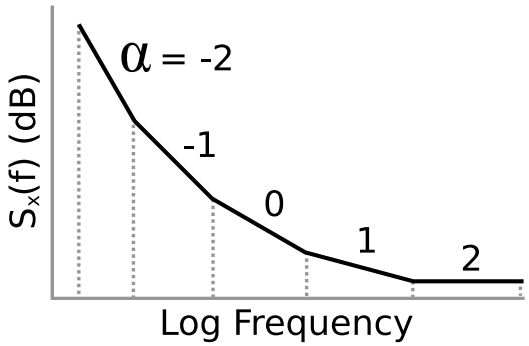

Figure 3.15: Piecewise linear representation of the power law noise model

3.5 Phase Noise Generation Using Multirate Filters

The multirate filtering procedure for generation of coloured noise sequences described in Section 3.4 on page 61 is well suited to the generation of synthetic phase noise sequences for radar simulation. The procedure, as presented, is suitable to the generation of coloured noise for a single value of α, generalizations to the procedure can be made to allow the generation of noise sequences matching the model presented in equation 3.8.

3.5.1 Polynomial Model of the Noise Spectrum

Where $S_x(f)$ matches the power law noise model (equation 3.9), it can be represented as a linear combination of powers of f^{-1} [102, 136], which corresponds to a strictly decreasing upwardly concave curve on a log-log scale. Figure 3.15 illustrates such a model, where noise of each category dominates over some part of the spectrum. The positions of the breakpoints in the linear piecewise model of the noise PSD depend on the values of h_α for each noise category of interest.

For each noise category α, h_α must be chosen to obtain a least-squares fit between the modelled PSD and the measured instantaneous phase deviation

PSD of the device to be simulated. That is,

$$\text{Error} = \int_0^{\frac{f_s}{2}} \left(\sum_{\alpha=-2}^{2} \left(\frac{h_\alpha}{4\pi^2} f^{-\alpha} \right) - S_x^m(f) \right)^2 df, \tag{3.39}$$

must be minimised, where $S_x^m(f)$ is the instantaneous phase deviation PSD of the measured oscillator. Methods for the extraction of h_α from measured data depend on the type of measurements available. Widely used techniques include extraction from the Allan variance or modified Allan variance (Section 3.2.2), the lag 1 autocorrelation technique [137] and least squares polynomial fitting. Direct least-squares polynomial fitting of $S_x^m(f)$ is not possible, but h_α for $-2 \leq \alpha \leq 2$ can be extracted from a fourth order polynomial fit to $f^4 S_m^x(f)$.

In order to perform this direct fitting, the spectrum of the phase noise must be estimated from a limited number of samples. The periodogram, the FFT of the samples with the application of a suitable window, has two major disadvantages for the estimation of power-law spectra [138]: high variance, and the effects of spectral leakage. High variance reduces the accuracy of a polynomial fit to the spectrum, and spectral leakage causes errors in the slope of the spectrum estimate where $\alpha < 0$.

Austin et. al. [138] recommend Capon's estimator [139] as particularly well suited to the estimation of power-law spectra. Other suitable techniques include the widely used Welch [140] modified periodogram method, and a variety of methods based on wavelets ([120] and [119], for example). An extensive discussion of spectral estimation procedures can be found in Kay [141].

The power law model (equation 3.9) can be directly implemented using a multirate filterbank to generate noise independently for each value of α. Efficiency can be increased, however, by only calculating each noise type over the decades of frequency where that noise type dominates. For example, if $\alpha = 0$ noise dominates $S_x(f)$ for some of the second and third highest decades of frequency, only those branches of the multirate filterbank corresponding to that frequency range need to be calculated. As some overlap is required for

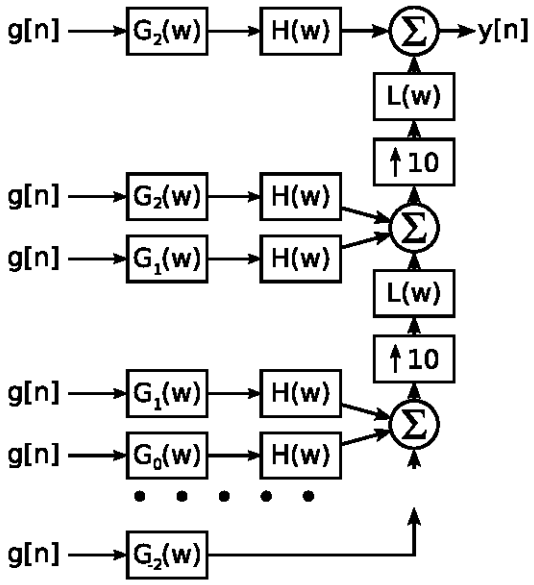

Figure 3.16: Modified multirate filter structure for the efficient generation of noise matching a spectrum polynomial in f^{-1} (from Brooker et. al. [6])

accuracy, and as frequency breakpoints are unlikely to be situated on decade boundaries, care must be taken to remove only those branches which will have an insignificant effect on the total noise PSD.

3.5.2 Phase Noise Generation Example

Figure 3.17 illustrates the result of the application of the piecewise noise generation model to the synthesis of phase noise matching the specifications of the MAXIM DS4026, a 10MHz TCXO [8]. A polynomial representation of $S_x(f)$ for $-2 \leq \alpha \leq 2$ (equation 3.9) was fitted to the specified characteristic phase noise PSD of the oscillator. The least-squares fit, figure 3.17(a), was found to match the specified phase noise curve within 4dBc/Hz between 10Hz and 1MHz from the carrier.

An implementation of the multirate filterbank, figure 3.12, was used to generate coloured noise for each α, which were scaled with h_α derived from the polynomial fit. Figure 3.17(b) compares the PSD of 10^6 generated samples and the target PSD. The generated noise closely matches the required PSD

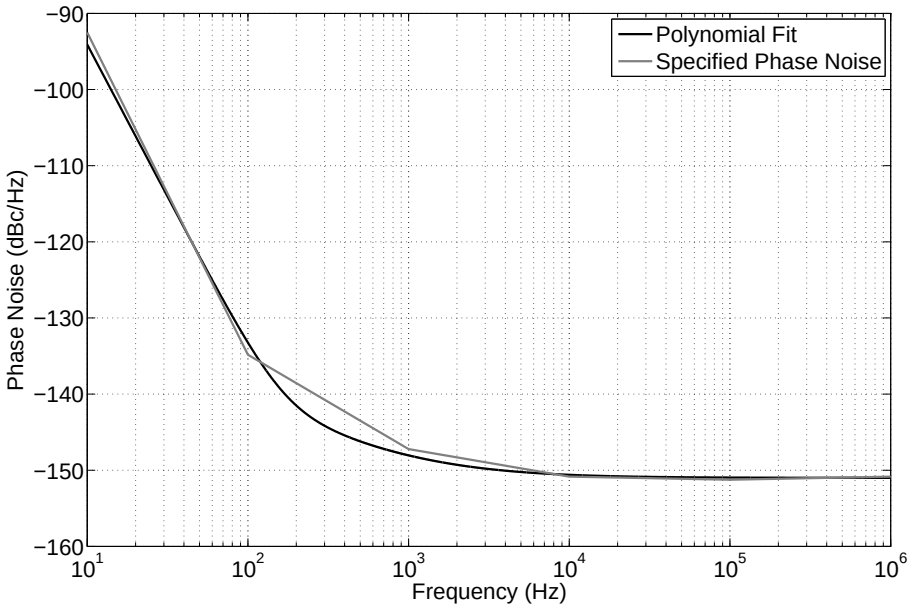

(a) Least-squares polynomial fit to specified phase noise curve

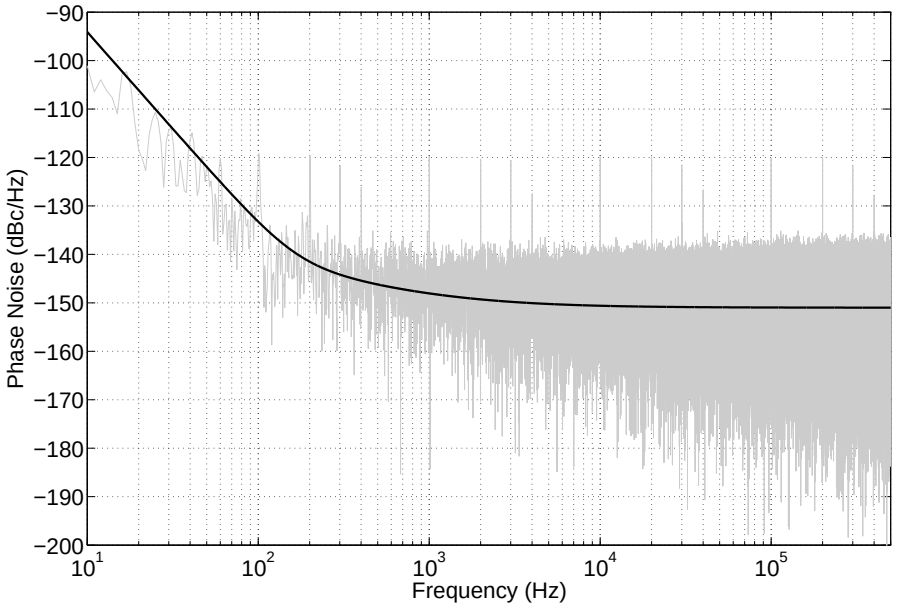

(b) Comparison of PSD of generated phase noise and target polynomial

Figure 3.17: Results of synthesis of phase noise matching the specifications of the Maxim DS4026 10MHz TCXO [8]

over the entire range of frequencies of interest.

3.6 Efficient Noise Synthesis for Pulsed Radar

For simulations of pulsed radar systems, synthetic phase noise is only required for simulation during the transmit and receive windows [26, 50]. It is necessary, however, to conserve the long-term correlations which are inherent in phase noise, due to the long-memory [100, 142] nature of the generating process. It is computationally inefficient to generate phase noise samples corresponding to the times when the simulated radar system is neither transmitting nor receiving.

The discrete Einstein-Wiener-Khinchin theorem [111, 60] states that the PSD of a sequence of samples $x[n]$ is equal to the discrete Fourier transform of the autocorrelation sequence of $x[n]$ [27]. From this observation, and the localisation property of the Fourier transform, it can be observed that the low-frequency branches of the multirate structure make the strongest contribution to the long-term correlations of $x[n]$.

Figure 3.18 illustrates the autocorrelation sequence for a 10^5 point noise sequence where $\alpha = 0$. The autocorrelation sequences of the filtered noise illustrates the effects of removing branches from the multirate filter. The autocorrelation of the lowpassed sequence (figure 3.18(b)) corresponds to the removal of the three highest frequency (and hence highest rate) branches from the tree. The autocorrelation of the highpassed sequence (figure 3.18(c)) illustrates the change in total autocorrelation due to the removal of these branches. While the absolute value of the differences is due to the relatively lower energy in the higher frequency bands, the shape of the high frequency autocorrelation illustrates that it makes little contribution to the long term correlation of the noise sequence. This results corresponds to the localisation property of the PSD — the support of the highpassed sequence is wide, therefore it has a narrow autocorrelation, conversely the support of the lowpassed sequence is narrow, and it has a wide autocorrelation. Similar results are obtained for $1 \leq \alpha \leq -2$.

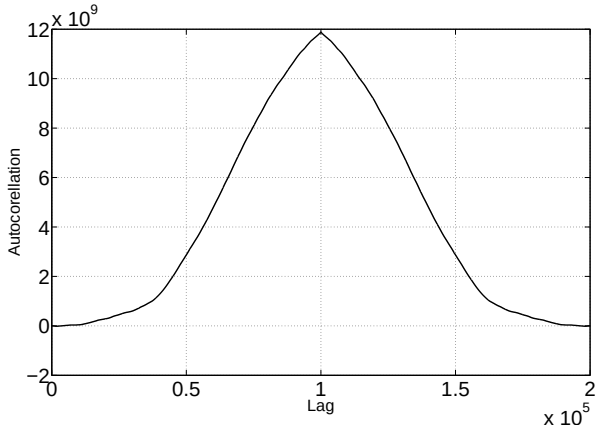

(a) Full spectrum

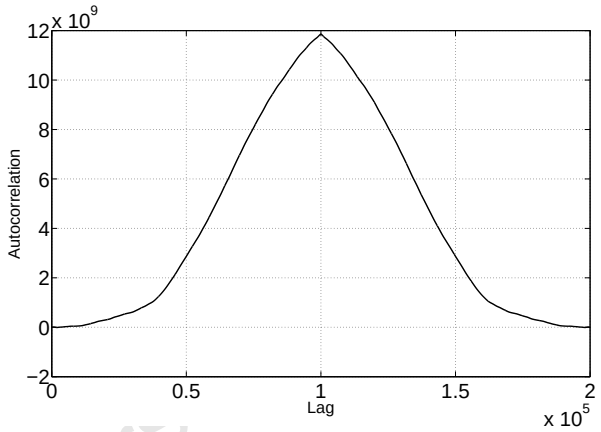

(b) Lowpass at $\omega = 2\pi/1000$

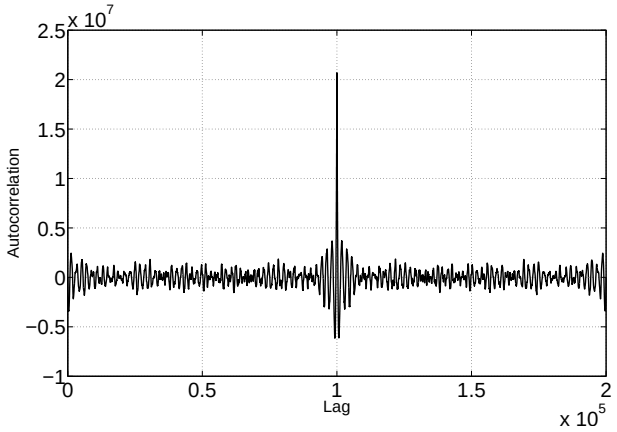

(c) Highpass at $\omega = 2\pi/1000$

Figure 3.18: Autocorrelation of filtered noise sequences for $\alpha = 0$

The Dynamic Pruning Approach

The long-term correlations present in $1/f$ noise sequences can be preserved while reducing computational costs by dynamically 'pruning' the higher frequency branches from the multirate filterbank during inter-pulse periods. Assuming $H(w)$ in figure 3.16 is an ideal high pass filter, the nth branch of the filter bank will decorrelate in approximately $\frac{10^k}{f_s}$ seconds. Branches which decorrelate during the inter pulse interval can be pruned during this interval without destroying the long-memory nature of the generated sequence. Pruned branches are flushed and restarted at the end of the interval.

Algorithm 1 Dynamic pruning algorithm

while Phase noise samples are required **do**
  while In the receive/transmit period **do**
    Calculate samples using complete structure
  end while
  Compute the number of branches that will decorrelate during the inter pulse interval, K
  Disable top K branches from the filter structure
  while In the inter pulse period **do**
    Calculate samples using pruned structure
  end while
  Flush memory of top K branches
  Re-enable top K branches
end while

If K of the D branches of the filterbank can be pruned during the interpulse periods, the number of operations per sample (equation 3.37) is reduced to

$$C_t = 4\left(N_G + N_H + 10N_L = 12\right)\sum_{i=K}^{D}\frac{1}{10^i} \tag{3.40}$$

The total reduction per branch removed is therefore approximately

$$C_t = \frac{\left(N_G + N_H + 10N_L = 12\right)\sum_{i=1}^{D}\frac{1}{10^i}}{\left(N_G + N_H + 10N_L = 12\right)\sum_{i=2}^{D}\frac{1}{10^i}} = \frac{1}{10}, \tag{3.41}$$

or 90% reduction per branch removed.

Applying the pruning approach to preserving long-term correlations allows these correlations to be preserved over the inter-pulse interval with low computational and memory requirements.

Dynamic Pruning Performance Example

The real world performance advantages of the pruned multirate filterbank approach were measured during the simulations of the pulse-Doppler system described in Section A.2 on page 133. This simulated system has a PRI of 50μs and a receive window of 2.5μs, for a total receiver duty cycle of 5%. To compare the performance of the pruned and complete structures, 200×10^6 samples were generated using the pruned and complete filterbanks.

The complete structure generated 200×10^6 samples in an average of 6.01s. The Callgrind [143] cache simulator estimated that 2.09×10^{10} CPU cycles were required on an Intel Core 2 processor. In this example, 95% of the generated samples were unused. Using the dynamic pruning approach, the samples were generated in an average of 0.25s, requiring an estimated 1.13×10^9 CPU cycles. This difference in computation time reflects an reduction in the required computation time by 18.5 times, while preserving the long-memory nature of the generated noise sequences.

Another example of the advantages of the dynamic pruning algorithm is present in Section A.2 in Appendix A. In this example, long term phase noise correlations were preserved over simulation times up to 100 seconds — which would have required a naive algorithm to generate 100×10^8 phase noise samples. For the 100s simulation, the dynamic pruning algorithm reduced the computer time required to generate the phase noise samples by a factor of 10^5.

3.7 Effects of Oscillator Behaviour On Radar Signals

3.7.1 Upmixing and Downmixing Effects

The effects of deviations from the ideal behaviour of the receiver (figure 2.13) and transmitter (figure 2.12) local oscillators can be modelled as a variety of effects on the complex signal envelope $x_l[n]$. The effects of these deviations on the performance of radar systems is complex, and highly dependent on the type of processing used on the received signals. Analyses for moving target indication (MTI) radar systems, for example, can be found in Shrader and Gregers-Hansen [144] and Kerr [145].

Deterministic Phase and Frequency Errors

Constant phase errors on the system clock ($x_d(t) = \phi$ for constant ϕ in equation 3.6) is equivalent to a phase shift of the received signal, and is not distinguishable from the phase shift due to propagation delay (equation 2.28). Constant frequency offset on the system clock ($x_d(t) = f_e t$ for constant f_e in equation 3.6) is equivalent to a time dependent phase shift on the received signal. For a single target, this time dependent phase shift is indistinguishable from the frequency shift caused by a time-dependent change in the target range — the Doppler effect.

Coherent [146] radar systems seek to reduce these constant deterministic errors through time and frequency calibration, as coherent operation has many advantages in both monostatic [147] and multistatic [86, 87] radar systems.

Random Phase and Frequency Errors

Including phase noise on the local oscillators in figure 2.8, an expression for the complex output $y(t)$, in terms of the input complex signal $x_l(t)$, instantaneous phase deviation on the transmit and receive local oscillators $n_t(t)$ and $n_r(t)$,

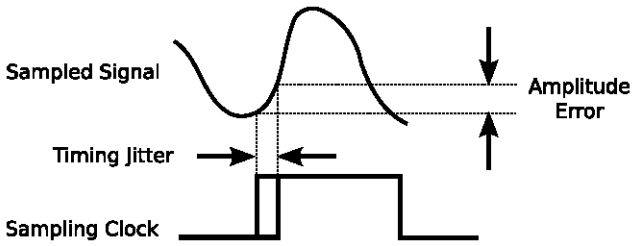

Figure 3.19: Amplitude error as a result of ADC timing jitter (after [9])

and propagation phase shift θ:

$$y_l(t) = x_l(t) \exp\Big(j(\theta + n_t(t) + n_r(t))\Big). \tag{3.42}$$

This process is equivalent to angle modulation [148] of the complex baseband signal $x_l(t)$.

The effects of random angle modulation of the received signal depend on the processing performed on these systems. In coherent pulse Doppler radar, random phase modulation reduces integration gain, and reduces Doppler and range resolution and accuracy. A complete analysis for pulse Doppler radar is presented by Belcher and Morris [149] and for MTI radar by Kerr [145].

Simulation results of the effects of phase noise on pulse Doppler and SAR systems are presented in Appendix A.

3.7.2 Jitter Effects

Jitter in Data Converters

Conversions of signals between digital and analogue representations assume that the clock pulses used for sampling and reconstruction are evenly spaced in time — there is no jitter present. Where jitter is present on these clocks, the signal to noise ratio of the conversion is reduced, and distortion can be introduced.

In analogue to digital converters, jitter introduces an error on the measured amplitude of each sample. As illustrated in figure 3.19, jitter causes the input waveform to be sampled at the wrong instant, introducing an error

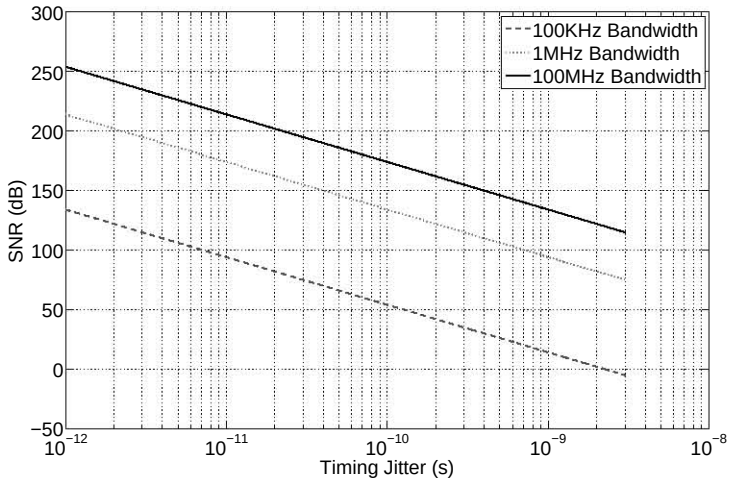

Figure 3.20: Data converter maximum SNR versus RMS timing jitter

proportional to the slope of the signal between the ideal sampling instant and the actual sampling instant. Similar effects are present on the output of digital to analogue converters [150]. In sampling of a single sinusoid of frequency f_0, the maximum SNR of the sampling system is [151]:

$$\mathrm{SNR}_{\max} = \frac{1}{4\pi^2 f_0^2 \sigma_t^2}, \tag{3.43}$$

where σ_t is the RMS jitter in seconds. For non-sinusoidal band-limited signals with bandwidth B and $\sigma_t \ll 1/B$, the maximum signal to noise ratio (SNR) is approximately [9]:

$$\mathrm{SNR}_{\max} = \frac{1}{2\pi^2 B^2 \sigma_t^2}. \tag{3.44}$$

Figure 3.20 illustrates the maximum SNR of a data converter in terms of the bandwidth of the converter and RMS timing jitter. The output SNR of the sampling process is degraded when the peak amplitude error due to timing jitter becomes bigger than the quantization step size at the effective number of bits of the ADC.

3.8 Conclusion

A multirate filterbank for the synthesis of coloured noise sequences has been developed, expanding on the results of Park et. al. [7]. This approach to the generation of coloured noise offers improved efficiency over methods such as direct IIR filtering [113], FFT based methods [112], and other widely used methods.

An investigation into the statistical properties of oscillator phase and frequency noise has been completed. A polynomial model for the power-spectral density of oscillator phase noise has been derived, based on a simple model of oscillator behaviour. This model has been combined with the multirate filterbank approach to coloured noise generation to create a complete algorithm for the generation of synthetic clock phase noise sequences, matching measured or specified oscillator performance parameters. Algorithms for the generation of sparse or pulsed sequences of synthetic oscillator phase noise samples have also been developed.

The multirate approach to the generation of synthetic phase noise sequences matching a specified PSD is believed to be novel, and an original contribution to the field. The application of pruning of multirate filterbanks to the generation of sparse coloured noise sequences is also believed to be novel.

Chapter 4

Simulator Development and Software Design

4.1 Introduction

This chapter presents a discussion of the development of the Flexible Extensible Radar Simulator (FERS), based on the simulation model presented in Chapter 2. FERS is freely available for use, modification and distribution under the terms of the GNU General Public Licence (GPL) [152]. FERS was designed and written for maximum portability, and can be compiled and used without modification on most modern operating systems (including Linux, Apple OSX and Microsoft Windows). The simulator uses open standards for data interchange, and does not require any commercial software or special purpose hardware. Complete source code for FERS is available from the Radar Remote Sensing Group, or for download from Sourceforge.net[1].

In this chapter, a high level discussion of the structure of the simulator is presented, along with detailed discussions of critical parts of the simulator software. A complete discussion of the development and implementation of an algorithm for designing fractional delay filters is presented, along with an examination of the importance of subsample accuracy in radar simulation. In addition, motivation for the choice of programming languages used to

[1] http://www.sourceforge.net/projects/fers/

implement the simulator software is presented.

4.1.1 Choice of Programming Language

The standard C++ [23] programming language was chosen for the implementation of the core simulator components and the Python [153] programming language was chosen for the implementation of extensions.

The Choice of C++

A wide variety of programming languages are available for the implementation of application level software. In order to choose a language, a set of requirements was developed.

Portability The language is required to be well supported on all major platforms and operating systems, including Linux, Microsoft Windows, Apple OSX and Unix. High quality compilers or interpreters for the language on these platforms must be widely available at low cost.

Standardization The language is required to be well standardized — allowing the code to be used for future projects without requiring specific compiler versions or specific software.

Performance The language is required to offer good and predictable performance for large numerical calculations and other computationally intensive tasks.

Multithreading The language is required to support multiple threads or processes, to allow the simulator to spread load over a number of processors or systems.

The ISO14882 [23, 154] standard C++ programming language, together with the widely used [155] and formally reviewed Boost [156] C++ libraries were found to meet these requirements better than alternative languages. C++ is a standardised language, with a wide variety of compliers available, both as open source and commercial software. It is supported on all widely used

platforms and operating systems, and offers performance competitive with the best languages for numeric computations with freely available compilers [157]. The C++ programming language is extremely popular, and has a market share of approximately 9% [158] (compared to approx. 20% for the market leader, Java). As several different versions of the C++ language are available, C++ will be used in this document to mean the ISO1442:2003 standard C++ language (sometimes called C++03).

Multithreading support for C++ is provided by the boost.thread library, which adds multithreading, synchronisation and thread management support to the C++ language. The boost.thread library is conceptually compatible with the thread support proposed [159] for addition to the C++ language in the upcoming revision of the ISO standard (widely called C++0x).

The C++ standard library [160, 154] offers a rich set of data structures and algorithms, including vectors, queues, heaps and searches and sorts optimised for these structures. These facilities are efficient, well characterized [161] and well documented. The FERS code makes extensive use of this standard library, as well as the extensions provided by the Boost [156] project.

C++ supports the Object Orientated (OO) programming paradigm, which was chosen as it is a natural match for the object focus of the simulation model (Chapter 2).

The Choice of Python

Where a compiled language, C++, was chosen for the implementation of the simulator, it was concluded that an interpreted language was more suitable for the implementation of extension components. Interpreted languages do not need to be compiled, and are interpreted from source code at program run time. This allows the simulation user to make changes to the components and have them available for simulation without recompiling.

Python [153] is a widely used interpreted programming language, with approximately 4.5% market share as of March 2008 [158]. It offers a wide variety of numerical and computational capabilities through the *scipy* and *numeric* libraries. In addition, Python provides mechanisms for interfacing

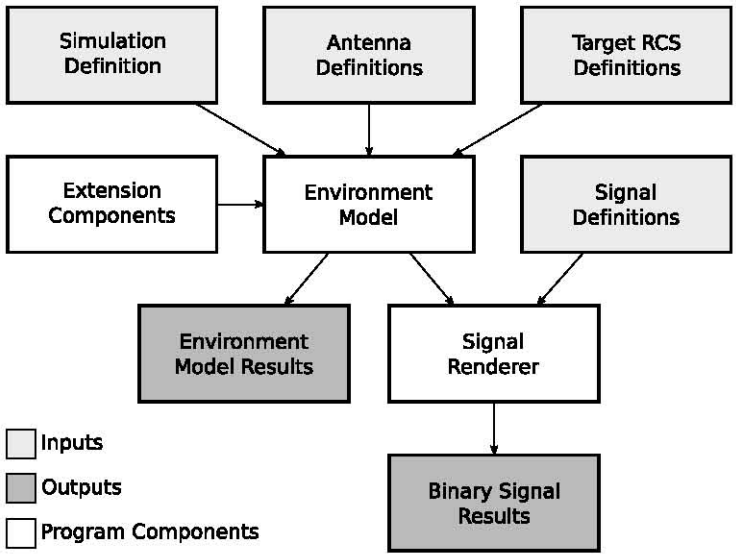

Figure 4.1: Block diagram of simulator software structure and data flow

with C++ code — simplifying the implementation of the extension mechanism.

4.2 Software Structure and Implementation

As illustrated in figure 4.1, the FERS simulator program consists of three software elements: the environment model, the signal renderer and optional extension modules. Each of these modules is completely independent, and communicates using well defined data structures over a simple interface.

The simulator takes a number of definition files as input. The simulation definition, or script, uses the extensible markup language (XML) to describe the radar system and environment to be simulated. The other definition files provide complete descriptions of antennas, target radar cross sections, and the waveform transmitted by each transmitter.

The simulator produces two sets of output. The first set is an XML file containing the results of the environment model — the basic parameters of radar performance such as range, return power, SNR, and other similar results. The signal renderer produces the second set of results: a binary file (in the widely used HDF5 format) containing the samples of each receive

window as captured by each receiver in the simulated system.

4.2.1 Input Data Files

The input data file formats for FERS were chosen to allow maximum flexibility in the specification of the parameters of the simulation and objects within the simulated world. The extensible markup language (XML) is used for all human readable data files, and the Hierarchical Data Format version 5 (HDF5) is used for all binary files. XML is a free, widely used container language for storing structured data in a human readable format. HDF5 is a widely used hierarchical binary file format, which is well supported and can be read and written by both MATLAB and GNU Octave.

Simulation Definition

The simulation definition file is an XML file containing all the simulation parameters, the parameters of each of the objects in the simulated environment, and all other simulator settings. Where complete details of the parameters of an object (an antenna gain pattern, for example) cannot be stored in the definition, the definition references an external file.

The major sections of the simulation definition are:

parameters One section describing simulation parameters such as start time, end time and propagation speed.

pulse One or more sections describing transmitted waveforms, or pointing to an external file containing waveform data.

timing One or more sections containing performance parameters for timing sources, such as phase noise and drift.

antenna One or more sections describing antenna gain patterns, or pointing to a file containing gain pattern data.

platform One or more sections describing platforms, and the receivers and transmitters attached to them.

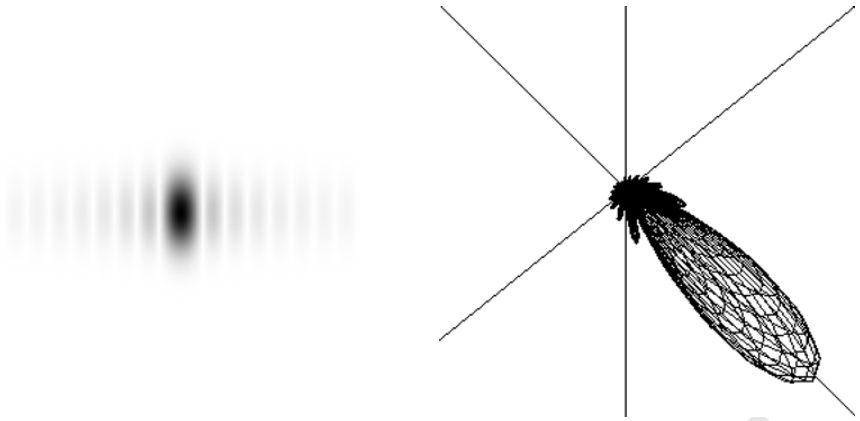

(a) Bitmap View (b) 3D View

Figure 4.2: Bitmap antenna view and corresponding 3D gain plot

include Zero or more sections referencing a file of supplementary XML data to include at that point.

The simulator definition format is designed to be easily human readable and editable — allowing both hand editing of simulation definitions and automatic generation by a graphical front end. A complete Document Type Definition (DTD) for the simulation definition is included with the FERS source code, along with a variety of examples. The simulation definition for the SAR experiments described in Section 5.2.2 on page 110 contains 80 lines of XML.

Antenna and Target RCS Definitions

Two formats are supported for antenna gain pattern definitions: an XML format and an HDF5 binary format. The XML format describes gain patterns as they are typically specified on antenna datasheets ([162] for example), with measurements of gain taken at points along the elevation and azimuth axes. The file specifies samples along each of the axes, and the simulator interpolates the off-axis antenna gains.

The binary antenna definition format, illustrated in figure 4.2, allows the user to specify antenna gain patterns for all azimuth and elevation angles. In this two dimensional array format, illustrated as a bitmap in figure 4.2(a),

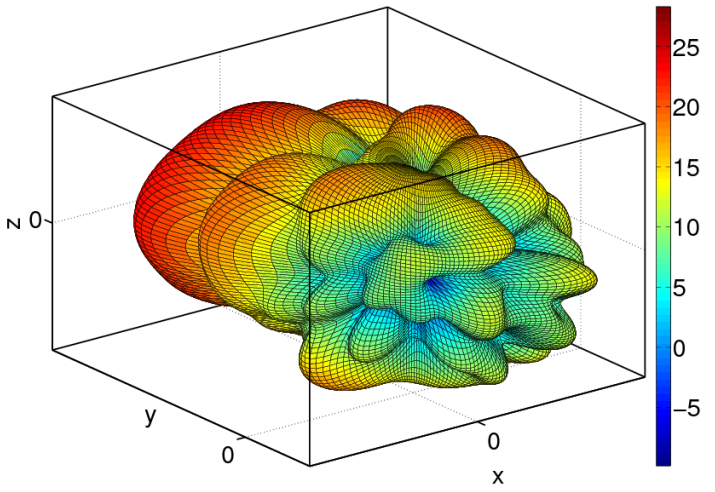

Figure 4.3: Bistatic RCS (in dBm^2) of an F5 fighter for transmitter at (-60°, 60°) (data courtesy of Professor Keith Palmer, University of Stellenbosch)

samples of the antenna gain are specified on a rectangular grid in azimuth and elevation. The grid spans π radians in elevation and 2π radians in azimuth. The grid spacing is user defined, and gains between the grid points are calculated by the simulator using cubic spline interpolation [62]. Figure 4.2(b) shows a 3D view of the antenna gain pattern corresponding to the bitmap in figure 4.2(a).

Monostatic target RCS patterns are specified in the same way as antenna gain patterns, using either the XML or binary format. Bistatic RCS patterns are a function of four variables (arrival azimuth and elevation, and departure azimuth and elevation), and are stored in an HDF5 file as a four dimensional binary array.

Figure 4.3 illustrates the bistatic RCS of an F5 fighter for a transmitter at 60° azimuth and −60° elevation, with the fighter pointing down the y axis and the colour scale in dBm^2. This is a three dimensional representation of a single two-dimensional slice of the entire bistatic RCS function.

Signal Definition

Signal definitions are stored as 64bit floating point samples in an HDF5 binary file. The signal is stored as samples of the complex envelope (see Section 2.1.3 on page 15) of the transmitted signal. The real (inphase) and imaginary (quadrature) parts of the signal are stored in separate columns.

4.2.2 Implementation of World Model

The world model calculates the parameters of each response (transmitter-receiver pair or receiver-target-transmitter triple), building work lists which the renderer uses to create the simulated data. The world model interfaces with the renderer through a set of work stacks, one per receiver, and is allowed to run to completion before the renderer starts.

The world model is completely multithreaded, allowing the simulator to take advantage of SMP systems and multicore CPUs.

Algorithm 2 World model flow

```
Load XML file with environment description
Build lists of transmitters, receivers and targets
Add transmitters and receivers for simulated multipath
for i = 1 to the number of receivers do
  while Running threads is equal to limit do
    Wait
  end while
  Create work stack for receiver i
  Create thread for receiver i
  Call world model in thread
end for
```

Algorithm 3 World model controller flow

for $j = 1$ to number of transmitted pulses **do**
  Add direct propagation from transmitter j to receiver i to work stack
  for $k = 1$ to number of targets **do**
    Add propagation from transmitter j via target k to receiver i to work stack
  end for
end for
Pass work stack to environment model

Algorithm 4 Environment model flow

for $i = 1$ to the number of items in work stack **do**
  if Item i is a direct propagation **then**
    Calculate receive and transmit antenna gain in relevant direction
    Calculate propagation loss
    Calculate range (R) and $\frac{dR}{dt}$
  else
    Calculate receive and transmit antenna gain in direction of the target
    Calculate propagation losses
    Calculate receive range (R_r) and transmitter range (R_t) to the target
    Calculate $\frac{dR_r}{dt}$ and $\frac{dR_t}{dt}$
    Calculate target RCS
  end if
  Calculate polarization effects
end for

4.2.3 Work Stack Entries

Each work stack entry corresponds to a single transmitted pulse (or entire waveform, for CW systems), from a single transmitter, received by a single receiver, and optionally via a single target. Work stack entries differ between long pulses and short pulses. For short pulses, the world model assumes that the first derivatives of range and power are constant (note that this is not

equivalent to the stop-go assumption used in some other radar simulators, which assumes these derivatives are zero). For longer pulses and CW, the work stack entry consists of a number of samples of these parameters, which are interpolated to calculate the values of these parameters in the renderer. The number of samples taken during the pulse interval is set in the simulation definition.

Each interpolation point contains the power, range, phase shift and Doppler shift for the pulse at the time of that interpolation point. Short pulse work list items contain two interpolation points — one at the beginning of the pulse and one at the end. Long pulse work list items contain a number of interpolation points set by the user. In addition to interpolation points, work list items contain the transmitted waveform, and the transmitter parameters including power and noise temperature.

4.2.4 Implementation of Renderer

The renderer consists of three sections, the *thread controller*, the *response renderer* and the *window renderer*. The thread controller section is run once per receive window, and calls the response renderer, as required, per response. The window renderer combines the responses to form the signal as seen in the receiver's receive window.

The renderer is completely multithreaded, allowing the simulator to take advantage of SMP and multicore computers.

Thread Controller

The thread controller takes a worklist for the pulses seen by the receiver from the world model, and calls the other renderer sections to render each receive window. It is run once per receive window. The flow of the thread controller is:

The thread controller ensures that the optimum number of threads are running until the worklist is complete. The simulator implementation assumes this number is equal to the number of cores in the machine. As the thread controller is not computationally intensive and spends the majority of the

Algorithm 5 Thread controller flow

```
Launch window renderer thread
for i = 1 to limit of render threads per window do
  while Number of render threads is equal to global limit do
    Wait
  end while
  Launch response renderer thread
end for
```

time waiting, it is not included in the total thread count.

Response Renderer

The response renderer modifies the transmitted signal to produce the response received by the receiver for each transmitter-target pair. In the notation developed in Section 2.1.1 on page 13, the response renderer calculates

$$y_{ijk}[n] = R_i\left(E_{ijk}\left(T_j\left(x[n]\right)\right)\right). \tag{4.1}$$

The flow of the response renderer is:

Algorithm 6 Response renderer flow

```
while Work list not empty do
  Lock work list mutex
  Pop work unit x from work list
  Unlock work list mutex
  for i = 1 to the number of samples in x[n] do
    Calculate the phase shift, time shift and amplitude at the time of i
    x[i] = x[i] * amplitude
    Design fractional delay filter for the time shift (see Section 4.3)
    Apply filter to x[i]
    x[i] = x[i] * amplitude * exp(−j ∗ phase shift)
  end for
  Add results to local window
end while
Lock render window mutex
Add local window to receive window
Unlock render window mutex
```

The response renderer uses binary semaphores (mutexes) [163, 164] to ensure thread safety during worklist management operations and when writing to the global render window. Per-thread local copies of the render window were implemented to reduce the time spent waiting on the render window lock. All other multithreaded operations are data independent, and hence do not require synchronisation to achieve thread safety.

Window Renderer

The window renderer combines the results from all the response renderer threads and prepares the results of the simulation. Additive noise, phase noise, quantization and sampling jitter are all applied to the simulated data by the window renderer.

Algorithm 7 Window renderer flow

```
Create sample buffer the length of the window
while Response renderer threads running do
    Wait
end while
for i = 1 to number of samples in window do
    Get phase noise sample for time i (see Chapter 3)
    window[i] = window[i] * exp(−j ∗ phase noise)
    Apply simulated jitter to sample i
    Quantize sample i
end for
Write results out to file
```

4.2.5 Computational Cost of Simulation

For reasonable simulation parameters, simulation run time is linearly dependent on the number of return samples to be calculated, equal to the product of the number of simulated pulses, pulse length in samples, number of targets, number of transmitters and number of receivers. All algorithms used by the simulator depend linearly on these parameters — hence the simulator can be

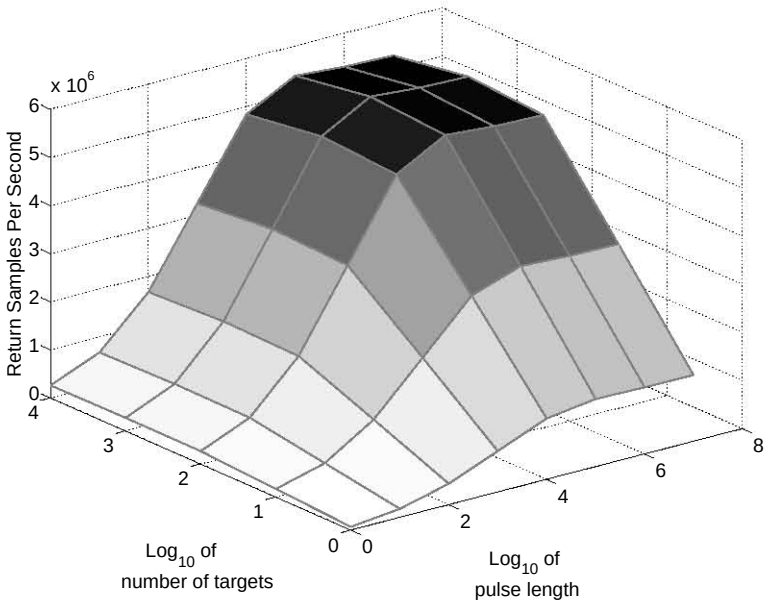

Figure 4.4: Simulator performance in return samples per second versus transmitted pulse length and target count

said to run in O(N) time, where

$$N = \frac{N_x N_{targ} N_{trans} N_{recv} t}{PRI} \tag{4.2}$$

and N_x is the pulse length, t is the simulation interval and PRI is the system pulse repetition interval. For CW simulations, $\frac{t}{PRI} = 1$.

Figure 4.4 presents simulator performance versus pulse length and target count. Simulator performance increases for large numbers, as startup overheads such as loading the script and pulse data dominate simulation time for small N. Performance reaches a plateau for large numbers of targets and pulse lengths, demonstrating the O(N) nature of the simulation algorithm.

The performance in figure 4.4 was achieved on a modestly priced quad core PC, with four cores at 2.4GHz (Intel Core 2 Quad Q6600) and 2GB of RAM. In this example, peak performance achieved was 5.63×10^6 samples per second. This performance corresponds to realtime simulation of an air search radar with a PRF of 400Hz, pulse width of 10μs, bandwidth of 25MHz and 50 targets, or a CW simulation with bandwidth of 5.6MHz requiring

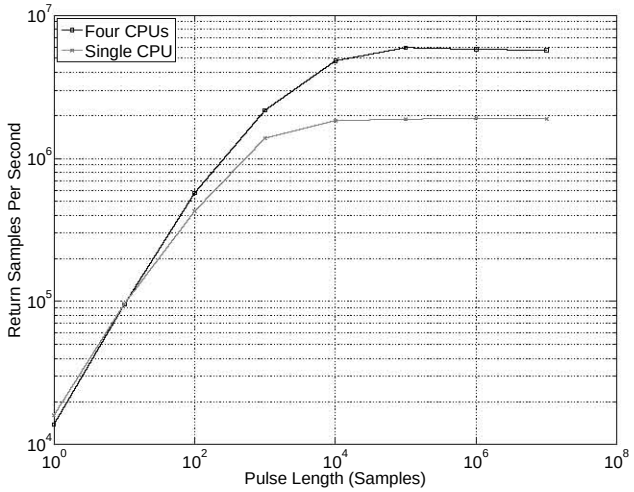

Figure 4.5: Simulator performance in return samples per second versus transmitted pulse length

approximately one second of runtime per second of simulated time per target.

A small decrease (approximately 5%) in performance is visible for large pulse lengths. Measurement with the Callgrind [143] cache and memory simulation tool based on the Valgrind [165, 166] binary instrumentation framework indicates that this is due to an increase in L2 data cache misses [167] with increasing working set size. The most significant cause of L2 data cache misses in the simulator is rendering data replacing the work stack entries in the data cache, causing cache misses when these entries are accessed.

SMP Scaling

Due to the multithreaded nature of the world model and signal renderer, simulator performance scales well with increasing processor count on symmetric multiprocessing (SMP) computers. Figure 4.5 compares simulator performance between a single CPU and four CPUs on the same hardware. The simulator is marginally faster on a single CPU for very small simulations ($N \ll 100$) due to reduced thread management overhead, but performs significantly better on multiple processors for larger simulations. Figure 4.6 illustrates the improvement factor achieved by running the simulator on a

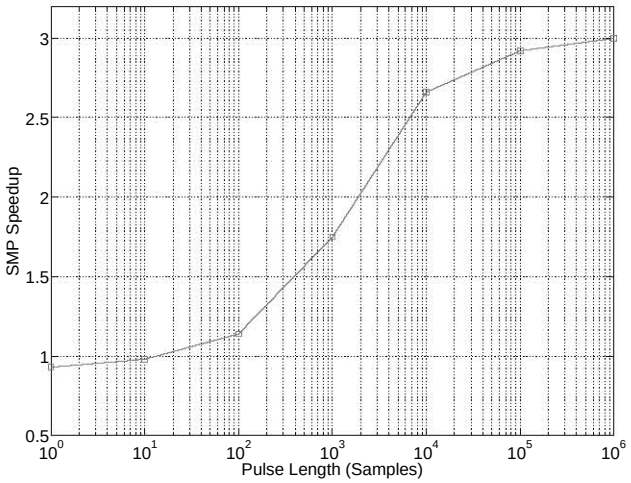

Figure 4.6: Simulation time reduction versus pulse length for a four core SMP computer

four core SMP computer. Significant performance improvements are visible for $N > 100$, converging on an improvement of approximately three times.

The Karp-Flatt metric [168] is widely used to estimate how well a computation task parallelizes. In the model used by the Karp-Flatt metric, parallelization seeks to reduce the serial portion e, defined as:

$$e = \frac{\frac{1}{\psi} - \frac{1}{p}}{1 - \frac{1}{p}}, \tag{4.3}$$

where ψ is the speedup observed when the program is run on p processors. The speedup ψ is defined as the ratio:

$$\psi = \frac{T_1}{T_p}, \tag{4.4}$$

where T_1 and T_p are the runtime of the program when run on 1 processor and p processors, respectively. Using this metric, and the data from figure 4.5, the serial portion e for large N can be estimated at $\approx 11\%$.

4.2.6 Extending Parallelization to Cluster Computers

MapReduce [169] is a pattern for the parallelization of programs based on a generalization of the *map* and *reduce* higher-order functions from functional programming ([170] or [171], for example). The MapReduce pattern allows simple parallelization of computing tasks on many types of computers, including clusters [169, 172], shared memory symmetric multiprocessing (SMP) computers [173] and heterogeneous multicore computers [174]. The term MapReduce is used in this section to apply to the pattern only, and not the implementation of the same name from Google, Inc.

The higher-order function *map* applies a function to a list of elements. Given the list $a = [b, c, d]$ and the function $f(x)$, the function *map* f a will return $[f(b), f(c), f(d)]$. The higher-order *reduce* (or *fold*) function combines a list of elements to produce a single value. Given the list $a = [b, c, d]$ and the function $f(x, y)$, the function *reduce* f a will return $f(a, f(c, d))$, using the 'right fold' and $f(f(a, b), c)$ using the 'left fold'.

The MapReduce model breaks a computation task up into two subtasks: a *map* task and a *reduce* task. The *map* tasks performs the *map* higher order function on a list of key/value pairs to produce an intermediate list of key/value pairs. The *reduce* task performs the corresponding higher order function on the intermediate list, to merge all the intermediate list items with the same key. Examples of this process for a variety of computation tasks are provided by Dean and Ghemawat [169].

FERS as a MapReduce Problem

The FERS renderer can be expressed as two MapReduce problems. The input to the first process would be a list of the signals transmitted from each transmitter in the environment. The first *map* step would produce a list of scattered signals for each transmitter/scatterer pair, which would be reduced to a list of scattered signals from each scatterer by the first *reduce* step. This process would be equivalent to the calculation of the results of E_{ijk} for all j and k in equation 4.1. The second MapReduce problem would then *map* the list of scatterer/scattered signal pairs onto a list of scattered signals for

each scatterer/receiver pair. The final *reduce* function would sum this list to produce a list of received signals for each receiver, completing the evaluation of equation 4.1.

The operations performed by such an implementation would be the same as those performed by the renderer implementation described in Section 4.2.4. The two implementations are therefore equivalent, and the FERS renderer can be considered an application specific implementation of the MapReduce model. While the current implementation scales efficiently on SMP machines, its equivalence to a MapReduce problem suggests that it could be implemented to scale efficiently on large computing clusters.

4.3 Fractional Delay Filter Design

In order to relax the stop-go limitation — the assumption that the round trip time is constant during a pulse — the simulator must be able to apply a time-varying group delay to each sample of the simulated pulse. Typically, this group delay will not be an exact multiple of the sample time, and a fractional sample delay is required. FIR fractional delay filters are well suited to this application, as they are computationally efficient and offer acceptable performance.

This section discusses the derivation and implementation of a design process for FIR fractional delay filters which offers sufficient computational efficiency to be executed per-sample.

4.3.1 Ideal Fractional Delay Filters

In a continuous time system, an ideal delay applied to the signal $x(t)$ can be expressed as:

$$y(t) = x(t - d), \tag{4.5}$$

where d is the delay in seconds. In a discrete time system, this becomes:

$$y[n] = x[n - df_0], \tag{4.6}$$

where f_0 is the system sample rate. Taking the z transform of the system expressed by equation 4.6 yields

$$H(z) = z^{-df_0}, \tag{4.7}$$

which corresponds to a digital allpass filter with the transfer function

$$H(e^{j\omega}) = e^{-j\omega d}. \tag{4.8}$$

Equation 4.7 can be implemented directly as a finite length FIR filter where $df_0 \in \mathbb{Z}$. Where the delay is not an integer number of samples, this transfer function must be realized using the family of filters known as *fractional delay filters* (FD filters) [175, 176].

The ideal FIR implementation of fractional delay filters is most simply derived from the Shannon interpolation formula [30, 28]:

$$x(t) = \sum_{n=-\infty}^{\infty} x[n] \operatorname{sinc}\left(tf_s - n\right). \tag{4.9}$$

The samples of the fractionally delayed signal $x(t-d)$, can therefore be represented as:

$$x(t-d) = \sum_{n=-\infty}^{\infty} x[n] \operatorname{sinc}\Big((t-d)f_s - n\Big). \tag{4.10}$$

The samples of the fractionally delayed signal $y[k]$ (equation 4.6) can therefore be expressed as:

$$y[k] = \sum_{n=-\infty}^{\infty} x[n] \operatorname{sinc}\Big(k + df_s - n\Big), \tag{4.11}$$

which is equivalent to convolution of $x[n]$ with an infinite length FIR lowpass filter with a transition frequency of $f_s/2$.

Direct implementation of a fractional delay such a FIR filter is not desirable, as it requires $O(N^2)$ processing time for $x[n]$ with length N. Truncation of this infinite length filter is therefore required.

4.3.2 Window Design of FIR FD Filters

Window design of FIR filters [29, 177] is simple, robust, computationally efficient, guaranteed to converge, and approaches the performance of the best known FIR filter design methods available for FD filters [178, 179]. The choice of window and window parameters is critical in realising optimum performance from fractional delay filters. The Hamming [180], von Hann [179], and Kaiser [181, 182, 183] windows have been applied to the design of FD filters.

The window design of FIR filters is performed by truncating the number of filter coefficients and applying a suitable window function to the remaining coefficients. The choice of window function influences the transition width, passband ripple and stopband attenuation [29, 134] of the resulting filter. The Kaiser (or I_0-sinh) window [184, 185] is an approximation, using the modified Bessel function of order zero of the first kind [186], of the prolate spheroidal wave functions [187] which provide a least-squares optimal tradeoff between the time and frequency domain widths of the window function [134] and hence maximize the ratio between mainlobe and sidelobe energy. The Kaiser window function is defined as

$$w(k) = \begin{cases} \frac{I_0\left(\beta\sqrt{1-(k/N)^2}\right)}{I_0(\beta)}, & |k| \leq N \\ 0, & |k| > N \end{cases} \tag{4.12}$$

where $I_0(x)$ is the modified Bessel function of the first kind [61], N is the width of the window in samples, and β is the window shape parameter.

Effects of N and β

The Kaiser window parameters β and N make this window good for the implementation of an adjustable FIR fractional delay filter design procedure, as the requirements for filter size (and hence computational cost), passband ripple, and bandwidth can be adjusted for the application in question.

In fractional delay filter design, the window shape parameter β represents a tradeoff between ripple in the passband and limited bandwidth. Figure

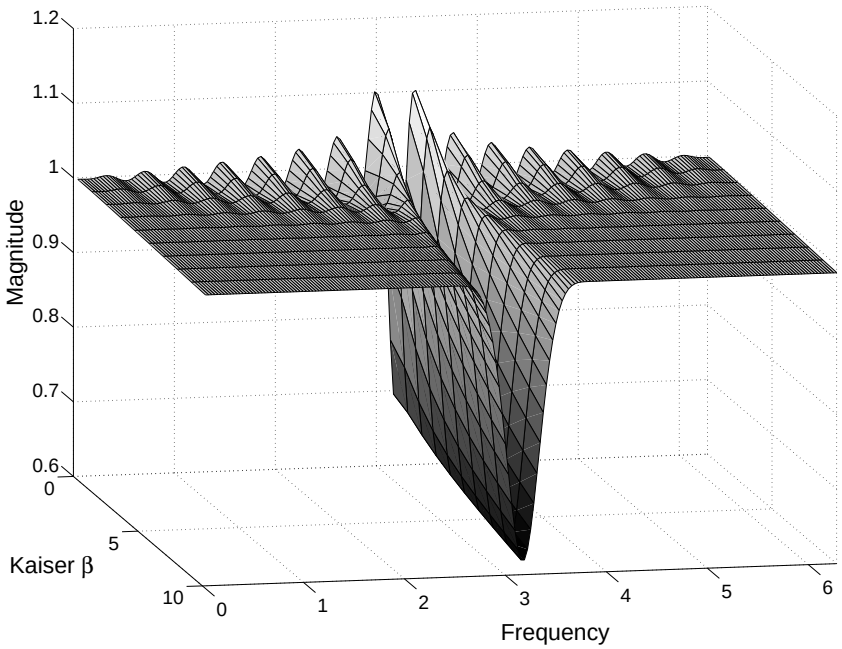

(a) System frequency response versus β for $N = 32$

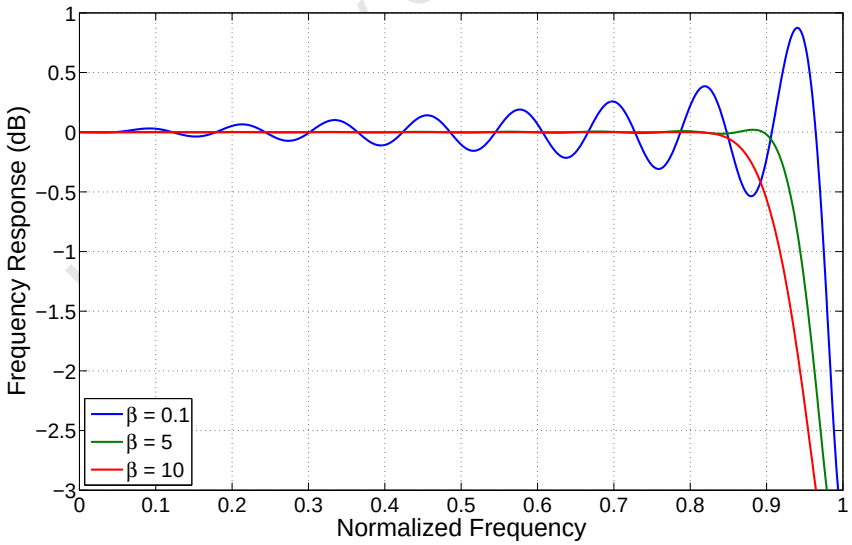

(b) Cuts through $\beta = 0.1$, $\beta = 5$ and $\beta = 10$

Figure 4.7: The effect of Kaiser window β parameter on the frequency response of a FIR fractional delay filter with $N = 32$

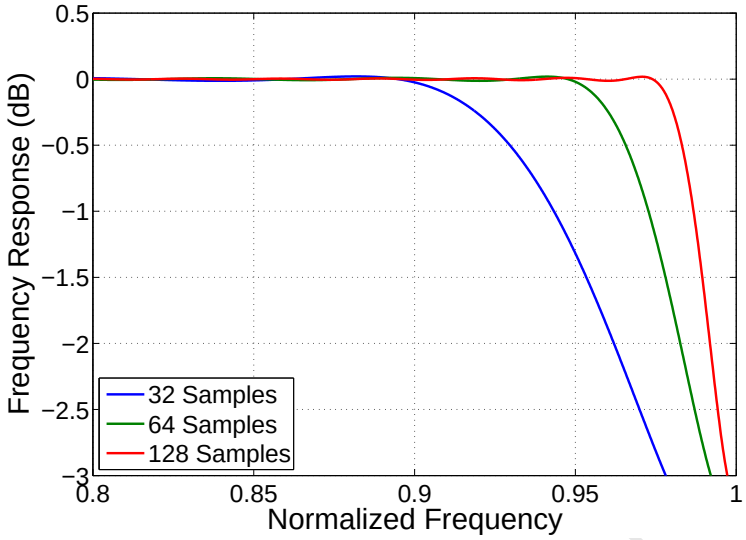

Figure 4.8: The effect of filter length on the frequency response of a FIR fractional delay filter ($\beta = 5$)

4.7 illustrates the effects of β on the frequency response of a fractional delay filter with $N = 32$ and $d = 0.5/f_s$. For small β, the filter is within 2dB of the ideal flat response up to $0.49f_s$, at the cost of 1.4dB peak-to-peak ripple in the passband. For larger β, the ripple is reduced, but the system passband is significantly narrowed. The ideal allpass response is flat across the entire frequency range.

The Kaiser window has the same mainlobe width as the Hamming window for $\beta = 5.441$, and the Blackman window for $\beta = 8.885$ [134]. The Kaiser window offers reduced ripple and better stopband attenuation than these windows for the same mainlobe width.

The length of the truncated filter represents a tradeoff between the system passband and the computational cost of filter implementation. Figure 4.8 illustrates the effects of the filter length N on a Kaiser windowed fractional delay filter with $\beta = 5$ and $d = 0.5/f_s$. The figure clearly shows that the system passband tends towards the ideal allpass response as for increasing N. Each doubling of N approximately halves the width of the transition band.

For the simulation of radar systems where the pulses are oversampled,

even by a small amount, the ideal tradeoff is a large β, for example $5 \leq \beta \leq 10$ and a short filter (e.g. $N = 32$ is sufficient in the case where the waveform is oversampled by 10%). Where the radar waveform is close to critically sampled the tradeoff is between significantly larger N (and hence longer computation times) and passband ripple due to decreased β.

The window design of FIR fractional delay filters is efficient, simple and offers excellent performance for oversampled signals. Alternative direct FIR filter design procedures are likely to be too computationally expensive for execution on a per-sample basis. While the Farrow [188] structure provides another alternative to the direct implementation of fractional delays which is well suited to time-varying delay applications, the associated computational costs are higher than for the table-based implementation of windowed FIR FD filters.

4.3.3 Implementation

The subsample filter design and application process requires $O(NM)$ runtime for window length N and signal length M. As the window length is constant, and small compared to the signal length, it can be assumed that the process runs in linear time. The most computationally expensive part of the implementation of the filter design process is the computing of the modified Bessel function $I_0(x)$ used by the Kaiser window. The modified Bessel function of the first kind is defined as [61]:

$$I_v(x) = (\frac{1}{2}x)^v \sum_{n=0}^{\infty} \frac{\left(\frac{1}{4}x^2\right)^n}{n!\Gamma\left(v+n+1\right)}, \tag{4.13}$$

which, for order zero, simplifies to [134]:

$$I_0(x) = 1 + \sum_{n=1}^{\infty} \left[\frac{(x/2)^n}{n!}\right]^2. \tag{4.14}$$

The Kaiser window requires values of $I_0(x)$ in the range $[0, \beta]$. FERS uses a twelfth order polynomial approximation to $I_0(x)$ (from Abramowitz and Stegun [61]), with a maximum error of 8×10^{-8} in the range $[0, 20]$. Using this

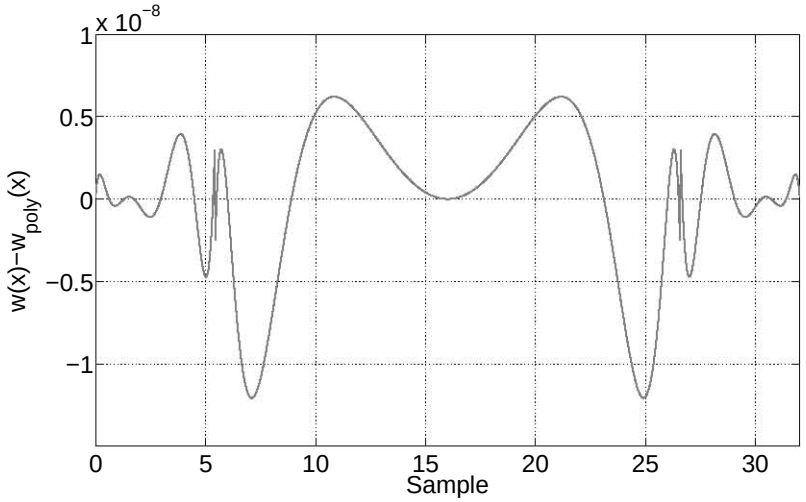

Figure 4.9: Error of polynomial approximation of Kaiser window function (N = 32, $\beta = 5$)

polynomial approximation, the approximated Kaiser window function $w_{poly}(x)$ is defined. Figure 4.9 illustrates the error in the approximated function, compared to the exact Kaiser window function $w(x)$ (equation 4.12).

For moving targets, transmitters or receivers (where $\frac{dR}{dt}$ is non-zero), the delay filter is recalculated for each sample and convolved with the input signal $x[n]$ to produce the output signal $y[k]$. As an optional optimisation, the simulator builds a table of precalculated subsample delay filters, for subsample delays in the range $[-0.5, 0.5]$. The filter is extracted from this table for the subsample delay value of each sample.

In this approach, $T \times M$ filter co-efficients are calculated at program startup, where T is the number of entries in the table and M is the filter length. As the filter table lookup is a cheap operation, the table based approach reduces runtimes for $T \times M \ll N$, for N defined in equation 4.2 on page 93. The processing speed gain due to this approach depends on the simulation parameters, and will be largest when N_x is the dominant factor in equation 4.2. Callgrind [143] measurements show that this approach decreases runtime by approximately 30% for the SAR simulations described in Section 5.2.2.

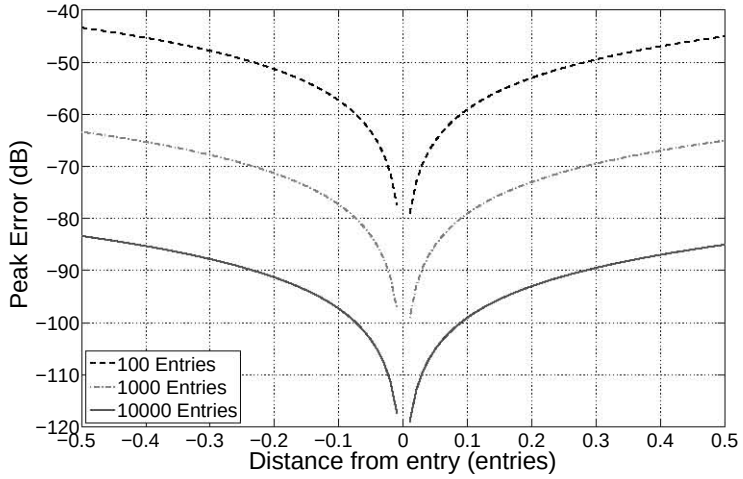

Figure 4.10: Peak subsample delay error versus distance from filter table entry

The loss in accuracy due to the table based approach depends on the level of quantization of the fractional delay, and hence on the number of table entries T. Figure 4.10 illustrates the peak error caused by using filters from the lookup table versus offset from the table entries ($d \times T - \lfloor d \times T + 0.5 \rfloor$, where d is the subsample delay). For a table of 10000 entries, requiring approximately 2.6MB of memory, the peak error is approximately -83dB. For comparison, the peak error for an implementation without subsample accuracy is approximately -6dB.

Sample accurate group delay implementation simulates the Doppler effect on baseband signals, and complex envelope of bandpass signals. Validation of the performance of the baseband Doppler implementation using bistatic sonar measurements is presented in Section 5.3.2 on page 119.

4.4 Conclusion

The FERS simulator, as described in this chapter, consists of approximately 9000 lines of C++ code implementing the simulation model described in Chapter 2 and the synthetic phase noise generation algorithm described in

Chapter 3. In addition, the simulator includes over 1500 lines of support code in MATLAB, Python and C++. The complete source code for the FERS simulator is freely available under the GNU GPL [152] version 2.

As described in section 4.2, the simulator implementation is divided into two parts: the world model and the signal renderer. The world model produces a high level description of the simulator output in XML format and provides these results to the signal renderer. The renderer combines the world model results to produce complete raw signal results for all simulated receivers. The complete simulator supports arbitrary radar configurations, including numbers of transmitters, receivers and targets limited only by available memory.

FERS runs well on modern PC hardware, with typical simulations (see Section 4.2.5 on page 92) taking from a few seconds to several minutes. Modern SMP PC hardware, including mass market multicore hardware, offers a nearly linear speed up with processor count for large simulation tasks.

Chapter 5

Validation of Simulator Accuracy

5.1 Introduction

Validation of the accuracy of the simulation model and implementation was performed using two approaches: comparison of simulation results with theoretical expectations, and comparison of simulations with measurements from the NetRad [76, 77, 78] netted radar and a bistatic sonar system. This chapter presents the results of these comparisons, and discusses the conclusions which can be drawn about the accuracy of the simulation results from each step of the validation process.

The validation programme was specifically designed to validate two types of simulator behaviour: the accuracy of simulation of phenomena explicitly implemented in the model, and the accuracy of emergent behaviours which are not explicitly implemented. Emergent behaviours reflect the ability of the simulator to predict aspects of radar performance beyond the scope of the simulation model. Validation of these behaviours tests many aspects of simulator performance.

The comparisons described in this chapter show that simulation results match measured results with a high degree of accuracy, and suggest that simulation results for other systems will be accurate.

5.2 Comparison with Theoretical Predictions

Radar signal processing techniques, such as moving target indication (MTI) and synthetic aperture radar (SAR) use the phase and amplitude of the received pulse to reject clutter (in MTI) and improve cross-range resolution (in SAR). These techniques are based on theoretical predictions about the properties of the received information. Processing simulated radar signals using these techniques will measure how accurately the simulated results match the predictions that the processing is based on, and hence will measure the accuracy of some aspects of the simulation results.

5.2.1 Moving Target Identification Radar

The term moving target identification (MTI) is typically applied to radars operating at a low PRF which enhance the detection of moving targets through application of time-delay cancelers. The simplest such canceller, the two pulse canceller, outputs the vector difference between two consecutive pulses [145]:

$$x_o[t + PRI] = x_i[t] - x_i[t + PRI], \tag{5.1}$$

where PRI is the system pulse repetition interval. For a single target return processed by a two pulse canceller, the output power is $4\sin^2(\pi f_d PRI)$, where f_d is the Doppler frequency of the target. When the target Doppler frequency is a multiple of the system PRF the target will be cancelled along with the clutter — these frequencies are referred to as blind frequencies.

Improved cancelers and processing techniques are available which seek to sharpen the notch at zero Doppler (cascaded delay cancelers) and reduce blind frequencies (PRF stagger). While these systems will not be considered in this section, the conclusions presented here also apply to these types of processing.

A key performance attribute for MTI systems is the improvement factor [144] — "The signal-to-clutter ratio at the output of the clutter filter divided by the signal-to-clutter ratio at the input of the clutter filter, averaged uniformly over all target radial velocities of interest" [189]. Errors in the

receiver LO frequency limit the improvement factor to [144, 145]:

$$I_{dB} = 20 \log_{10} \left(\frac{1}{2\pi \delta f T} \right), \tag{5.2}$$

where T is the round trip propagation delay, and δf is the pulse to pulse frequency change.

Figure 5.1 compares the results of simulation of the effects of receiver LO frequency drift on MTI improvement factor with the theoretical limit. The simulation was structured to ensure that LO frequency drift was the limiting factor on MTI improvement. The simulated and theoretical results agree very closely at both short (20km) and long (210km) ranges.

Another limit on the MTI improvement factor is antenna scan modulation: the return power changes between views caused by the antenna gain pattern. The clutter power standard deviation due to scanning with a Gaussian pattern antenna is [144]:

$$\sigma_c = 0.265 S_r W_b, \tag{5.3}$$

where S_r is the antenna scan rate (in degrees per second) and W_b is the -3dB beamwidth of the antenna, in degrees. The improvement factor limit for a three delay canceller is [50]:

$$z = \frac{2\pi \sigma_c}{PRF} \tag{5.4}$$

$$I_2 = \left(1 - \frac{4}{3} \exp\left(\frac{-z^2}{2}\right) + \frac{1}{3} \exp\left(-2z^2\right)\right)^{-1}. \tag{5.5}$$

Figure 5.2 compares the results of simulation of the improvement factor of an MTI system versus the limit from equation 5.5. The simulated system has an antenna beamwidth of 6°, scan rate of 360° per second and other parameters chosen to ensure that the improvement factor is limited by scan modulation. The simulated results and theoretical predictions match extremely closely over the entire range of pulse repetition frequencies simulated.

Comparison of the results of the simulation of an MTI system with theoretical performance predictions revealed very close agreement between theory and predictions. The phenomena tested by the simulation of MTI

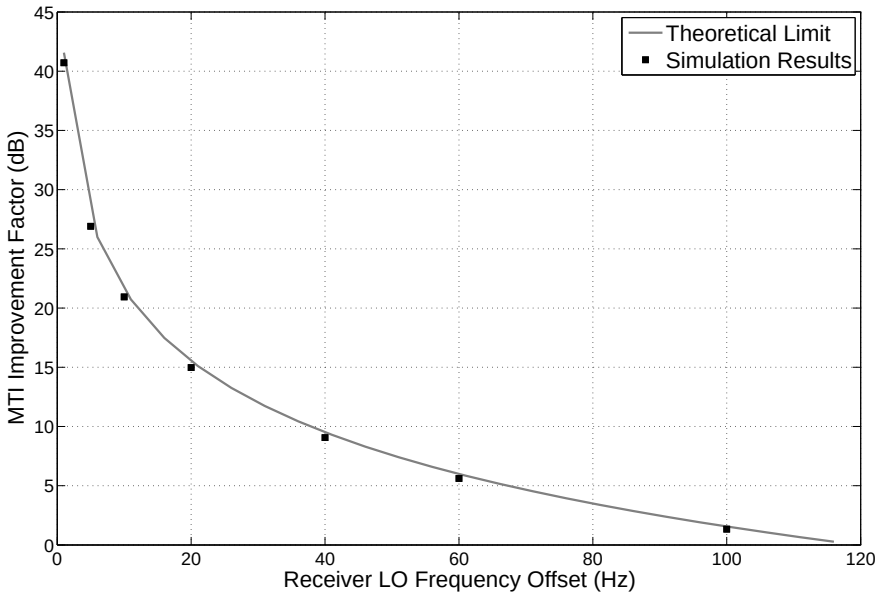

(a) 420km Round Trip

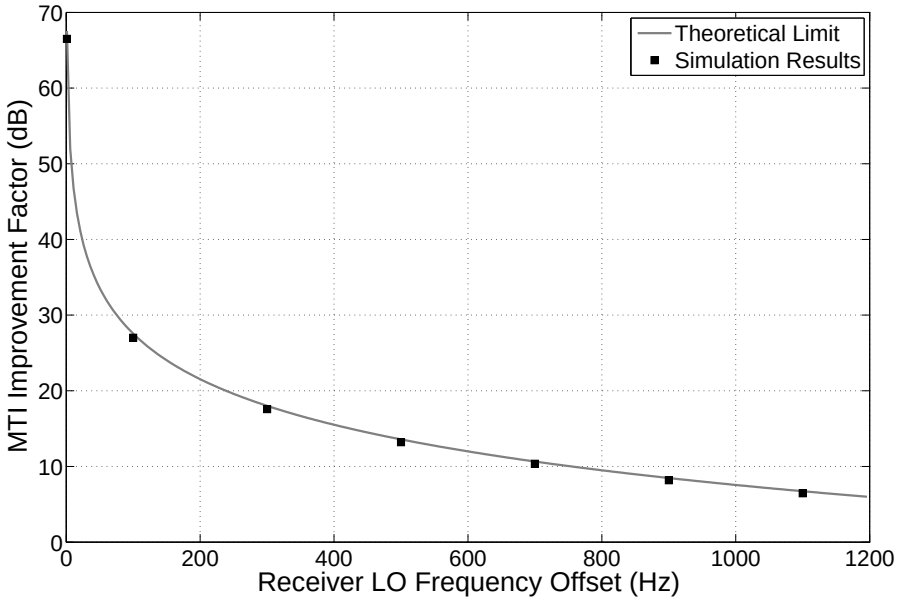

(b) 40km Round Trip

Figure 5.1: Comparison simulated MTI improvement versus theoretically predicted limit

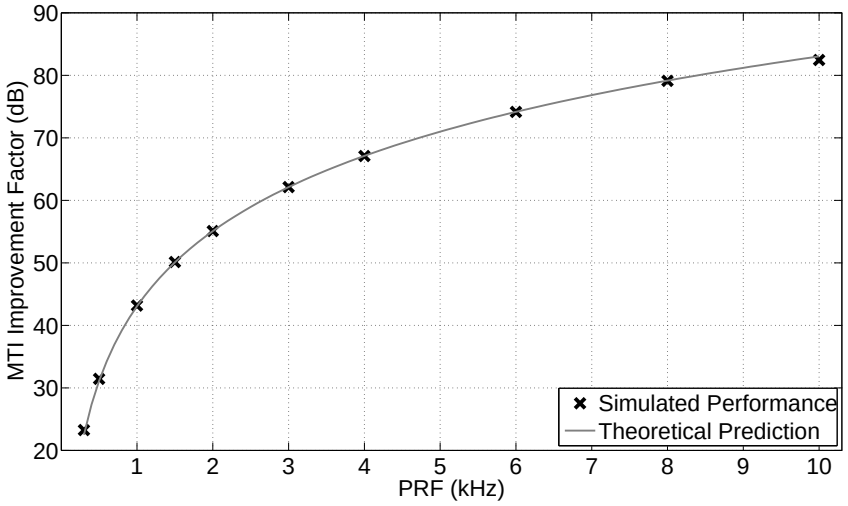

Figure 5.2: MTI Improvement factor limitation due to antenna scan modulation

systems are not explicitly implemented in the simulation model, and are emergent behaviours of the model.

5.2.2 Synthetic Aperture Radar

Synthetic aperture radar (SAR) is a type of radar signal processing which simulates the effect of a narrow beam (or long aperture) by performing signal processing on a train of received pulses [190, 191]. Conceptually, the simplest type of SAR is airborne stripmap SAR, where an aircraft is flown along a linear track with an antenna looking sideways at a swath of ground. Figure 5.3 illustrates the geometry of an ideal stripmap SAR system.

The South African SAR system (SASAR) is a VHF SAR sensor [192, 193] designed and built in South Africa during the 1990s. Part of the project was the development of an advanced Range-Doppler SAR processing suite, titled G2 [10, 194]. This section presents the results of simulation of a SAR system with the same parameters as SASAR, with the results processed with the G2 SAR processor. Table 5.1 lists the parameters of the SASAR system used in the simulations in this section.

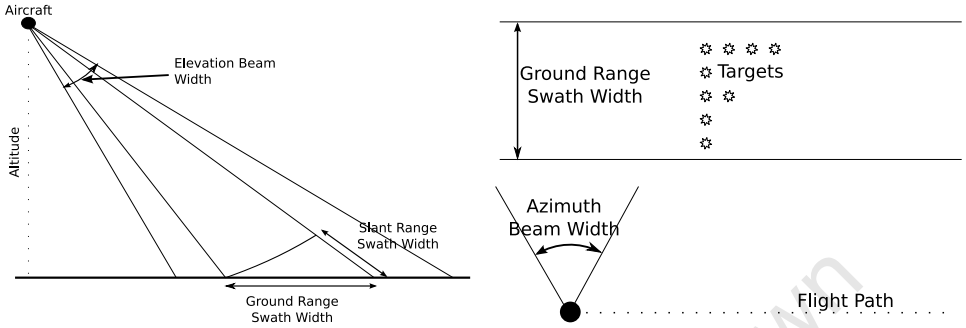

(a) Side view (after [10])

(b) Top view

Figure 5.3: Airborne Stripmap SAR Geometry

Table 5.1: SASAR System Parameters (after [10])

Parameter	**Value**
Centre Frequency	141MHz
Bandwidth	12MHz
Pulse modulation	monochromatic
PRF	545Hz
Ground Speed	90 ms^{-1}
Altitude	4000 m
Azimuth Beamwidth	60°
Elevation Beamwidth	60°
Sample rate	24MHz

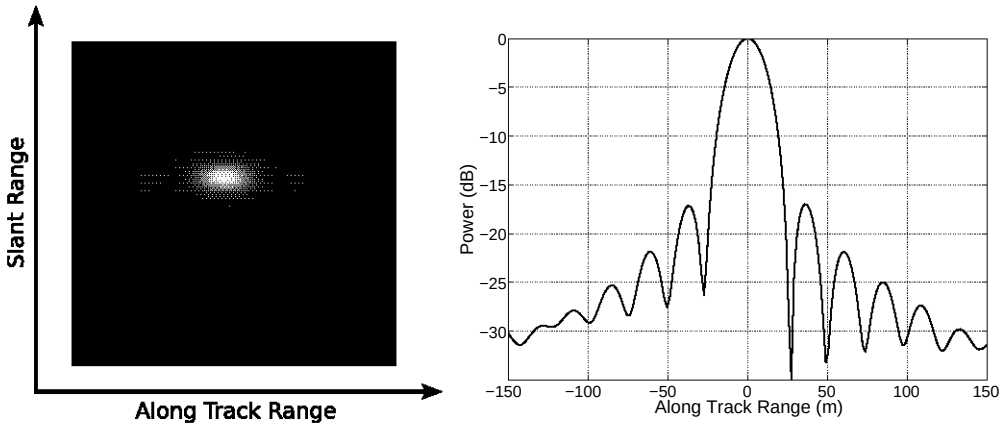

(a) SAR Image (b) Cut through target

Figure 5.4: Processed results of VHF SAR simulation with single target

Figure 5.4 illustrates a SAR image of a single target, simulated with FERS and processed with G2. The image in 5.4(b) spans 1245m in slant range by 165m in along track range. Four seconds of simulated data were generated, corresponding to a synthetic aperture of 360m. The image clearly shows a single, sharpened target — demonstrating that the phase calculations in the simulator match the theoretical predictions used by focused SAR processing. Figure 5.5 is a multiple target test, with the targets spaced 80m apart in along track range and 200m apart in ground range. This test case demonstrates that phase calculations are valid at all ranges.

Increasing the effective synthetic aperture of a SAR system improves resolution, and reduces the width of a single target. Figure 5.6 illustrates the effects of increasing the synthetic aperture on the sharpness of a single target. Results are presented for 1s, 2s and 10s of data.

Deviations in the trajectory of the radar sensor reduce the accuracy of SAR processing, as the phases of consecutive pulses can no longer be precisely aligned. Most SAR systems perform motion compensation using measurements of the platform's position to correct for these deviations. The G2 processor, for example, can perform motion compensation using measurements from GPS and an inertial platform [10].

Figure 5.7 on page 114 shows the effects of uncorrected sensor trajectory

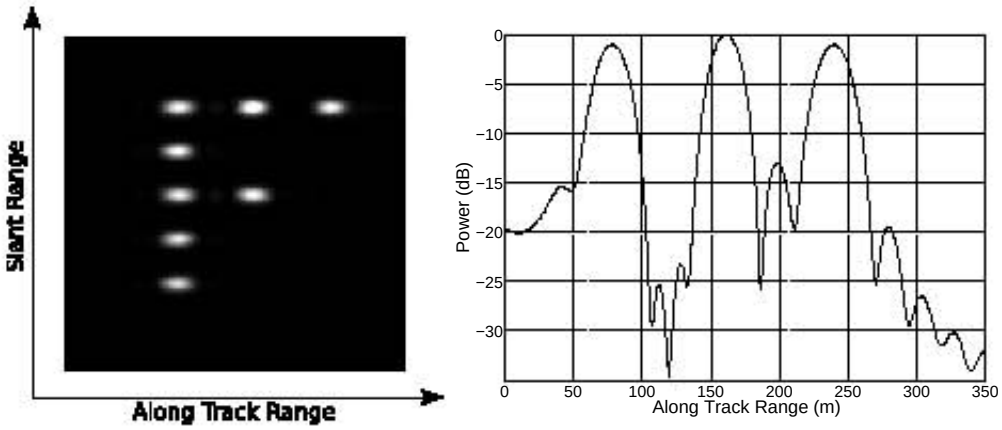

(a) SAR Image (b) Cut through target

Figure 5.5: Processed results of VHF SAR simulation with multiple targets

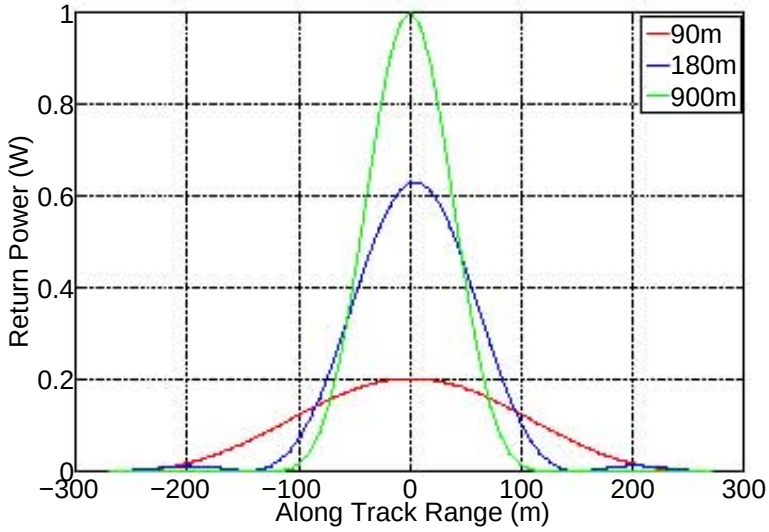

Figure 5.6: The effect of synthetic aperture length on the sharpness of SAR targets

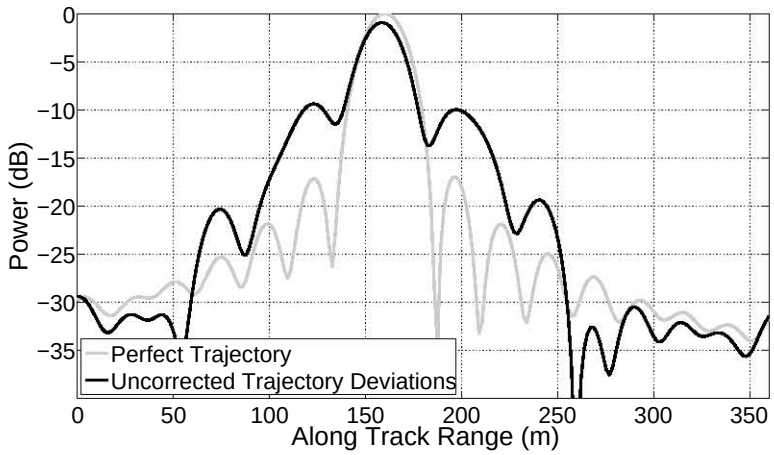

Figure 5.7: Effect of sensor trajectory deviations on SAR processing

deviations as a cut through the target. In this example, the altitude was perturbed with a sinusoidal modulation with an amplitude of 0.25m and a period of 2s. The results clearly illustrate how sensor trajectory deviations reduce the integrated sidelobe ratio (ISLR) and increase the peak sidelobe level — corresponding to the along track blurring of SAR images. A discussion of the effects of local oscillator phase noise on SAR processing, and its equivalence to uncompensated motion errors, is presented in Appendix A.

These results of from SAR processing provide a qualitative demonstration of the accuracy of the simulation of a VHF SAR system produced by FERS. In each case, the parameters of the processed SAR image depend on the parameters of the simulation in the way predicted by theory. This demonstrates the accuracy of phase calculations, and the simulation of systems with moving sensors.

5.2.3 Passive Coherent Location

A passive coherent location (PCL) radar is a multistatic radar system which uses non-cooperating 'illuminators of opportunity' instead of a traditional transmitters [195]. Suitable illuminators include FM radio transmissions [196, 197, 198, 199], analog television [200, 201], GSM cellular telephone transmitters [202] and satellite transmitters [203]. The advantages of PCL

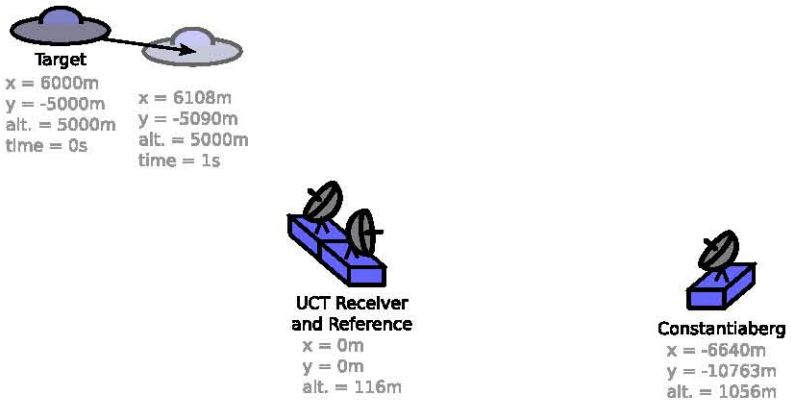

Figure 5.8: Layout of the transmitter, receiver and target for PCL simulations

include reduced cost, improved resistance to some types of stealth technology, improved resistance to electronic counter measures and stealthy operation. Working examples of PCL systems include the Silent Sentry air surveillance radar from Lockheed Martin, and the Manastash Ridge system for remote sensing of the upper atmosphere [199].

A PCL air surveillance radar, based on FM radio transmissions, is currently under development at UCT. The prototype system will use receivers based at UCT and the FM transmitter at Constantiaberg to track aircraft targets approaching Cape Town International Airport. In simulation experiments designed and performed by Sebastiaan Heunis at UCT, FERS was used to predict the performance of the prototype simulation system. This section demonstrates the accuracy of FERS simulations of a CW PCL system using some of the results from these experiments.

Simply, the PCL system receives the direct (reference) signal and scattered signal using two separate antennae. The reference signal (which is much higher in power than the scattered signal [195]) is phase shifted and mixed with the scattered signal channel, to attenuate the portion of the direct signal received in that channel. Processing is performed by correlating the reference signal, and Doppler shifted versions of the reference signal, with the scattered signal.

Figure 5.9 shows the range-Doppler plots of the processed results for two PCL signals with 50MHz bandwidth. In figure 5.9(a), the signal used was a one second simulated commercial FM radio signal, with the station

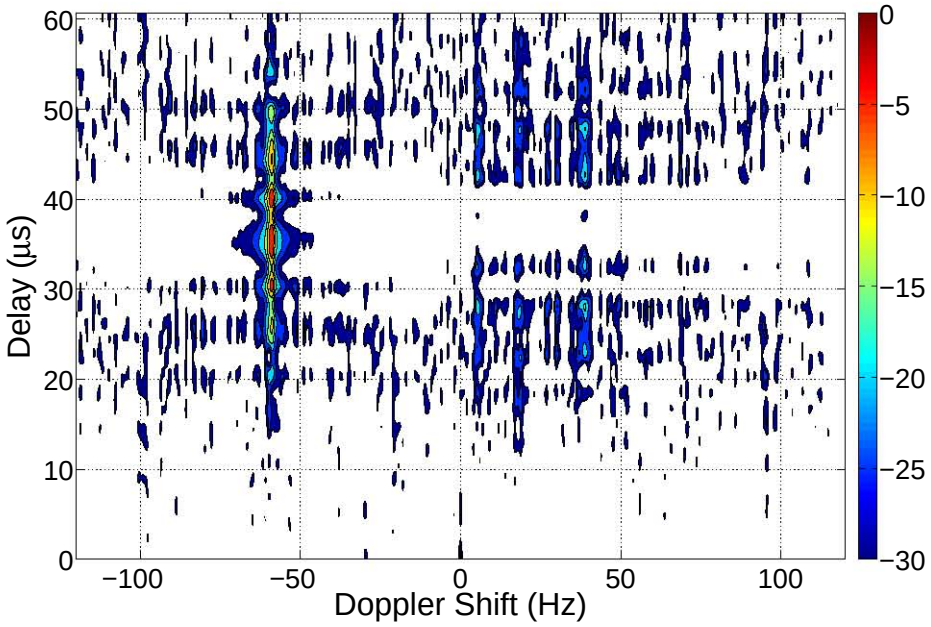

(a) Simulated FM radio signal

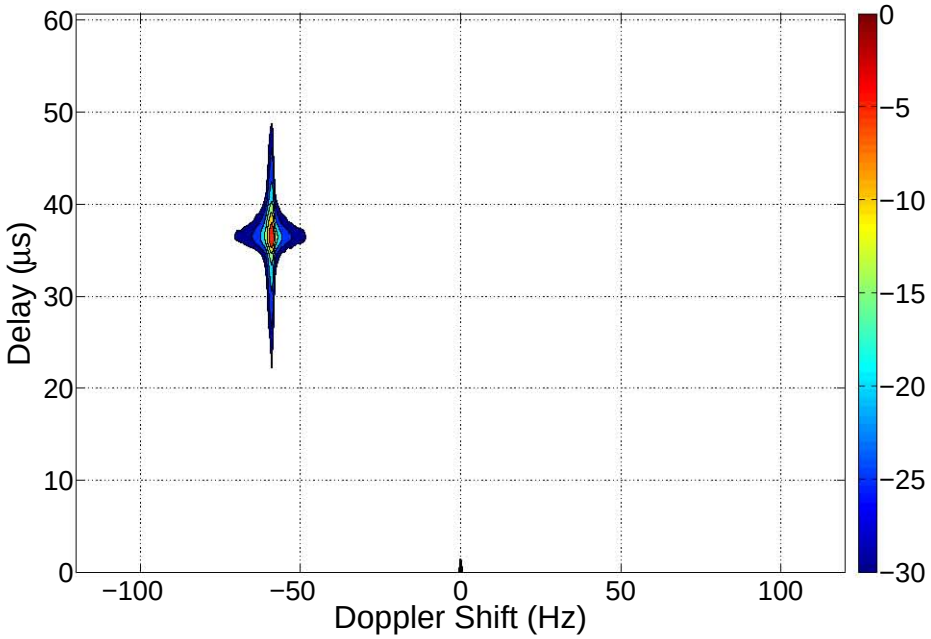

(b) White Gaussian Noise

Figure 5.9: Range-Doppler plots for processed PCL simulation results (simulation by Sebastiaan Heunis)

transmitting a metalcore (similar to punk and heavy metal music) track. The signal used for figure 5.9(b) was white Gaussian noise with the same bandwidth as the simulated FM signal. In both examples, processing was performed using a frequency domain cross-correlation method.

The comparison of figures 5.9(a) and 5.9(b) clearly demonstrates that, while the FM signal clearly shows the target, the 'ambiguity function' (in the sense used by Baker, et. al. [204]) for the white Gaussian noise is closer to optimal. In both cases, the target is shown at the correct range (approximately 36.4μs delay) and Doppler shift (approximately -59.5Hz. Note that the delay figure refers to the difference in arrival times of the scattered signal and reference signal. These preliminary results show that FERS is able to simulate a CW system, and introduce the correct Doppler and time shifts onto the return signal. The structural similarity of the results in figure 5.9(a) and the results obtained by Baker, et. al. [204] for FM signals suggests that the FERS simulation and processing are producing plausible results.

These results present the first results of an ongoing process of simulating PCL performance. They are a strong demonstration that the FERS simulator is able to simulate a PCL system, and can be used for the prediction of PCL performance.

5.3 Comparison with Measurements

The ultimate goal of a simulator is to produce results matching those which would be produced by a physical system with the same specifications as the simulated system. Comparison of simulator outputs against measured results is therefore an extremely important step in the verification process. This section describes two sets of verification comparisons — one with a prototype netted radar system and one with a simple bistatic sonar system. The goal of the netted radar comparisons was to verify the accuracy of simulations of a multistatic pulse Doppler radar. The goal of the comparison with the bistatic sonar was to verify the accuracy of the baseband delay (and hence Doppler) calculations and the group delay renderer (Section 4.3).

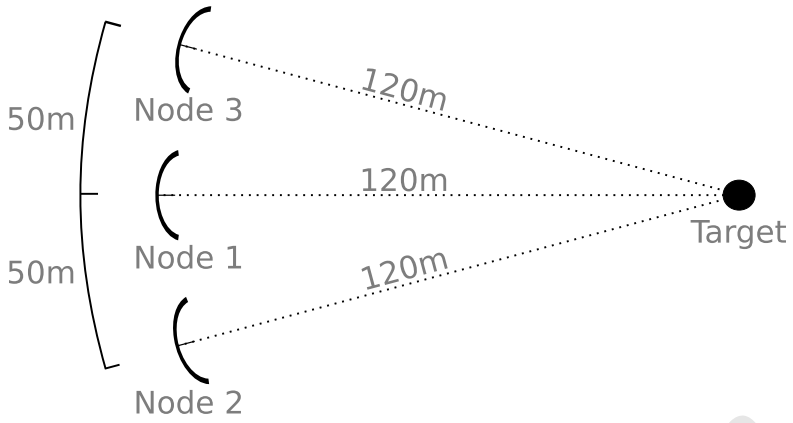

Figure 5.10: Netrad geometry used for validation measurements

5.3.1 Netted Radar System

Netrad [75, 76, 205, 77, 78] is an experimental pulse-Doppler netted radar system developed at the University College London. The system has three nodes operating at 2.4GHz, with a maximum bandwidth of 50MHz, maximum power of −23dBm, and antenna gain of 15dBi [162]. For the comparisons presented here, the nodes were set up as illustrated in figure 5.10.

In the default configuration, transmissions are interleaved between the nodes (with node 1 transmitting, then node 2, then 3) with a total PRF of 20kHz. The measurements described in this section were performed with a 1.5ms linear chirp with a bandwidth of 50MHz.

A series of measurements using the Netrad system were performed by Doughty, et. al. at UCL in July 2007. Comparisons between data from this measurement campaign and simulations of the measured scenarios were used to validate the accuracy of FERS simulations of netted radar systems. A number of scenarios were simulated, including static targets, large moving targets (such as a van), and small moving targets (such as a walking man).

In all cases, it was found that the simulated results closely matched the measured results, taking into account the assumptions made by the radar simulator. While the range used for the measurements was relatively free of clutter [77], some clutter returns were still present in the measured data — and absent in the simulations. Some types of moving targets, including

people and vehicles, were found to be spread out over several Doppler bins, due to microdoppler, an effect which wasn't included in simulations of the netted radar system.

Figures 5.11 and 5.12 present a comparison between simulated and measured results for an experiment performed with Netrad. In this experiment, a van was driven obliquely across the range at 9ms^{-1} and observed using interleaved pulses from each transmitter in turn. Pulses were received on all three transmitters. Range-Doppler plots for pulses transmitted by Node 1 and received by Node 3 are shown in figure 5.11. The overall structure of the simulated and measured results are identical — with the peak in range bin 15 and Doppler bin 9. Stationary clutter is present in Doppler bin 0 in the measured data, but is clearly separated from the moving target.

Cuts through the the target in range and Doppler are presented in figure 5.12. In Doppler (figure 5.12(a)), the peak position and rolloff of the simulated data and measured data are similar. Noise is less effectively suppressed in the measured data, and the maximum deviation between measured and simulated signals is small. In the range cut (figure 5.12(b)), the differences between the simulated and measured data are small — mostly limited to clutter returns beyond range bin 30.

While these figures only present the results of a single simulation, they correlate well with the results of simulations of other measurements taken with the netted radar hardware. In all cases, it was found that the processed range-Doppler results of the simulations closely match the measured results. The results demonstrate both the accuracy of the simulation model for bistatic radar (Chapter 2) and the correctness of the implementation of this model.

5.3.2 Bistatic Sonar

Validation of the baseband phase and frequency shift model, and its implementation (Section 4.2.4), was performed using a bistatic CW sonar (ultrasound) system. The sonar system used for these tests was designed and built by the author.

Figure 5.13 illustrates the setup of the ultrasound sonar system. A 40kHz

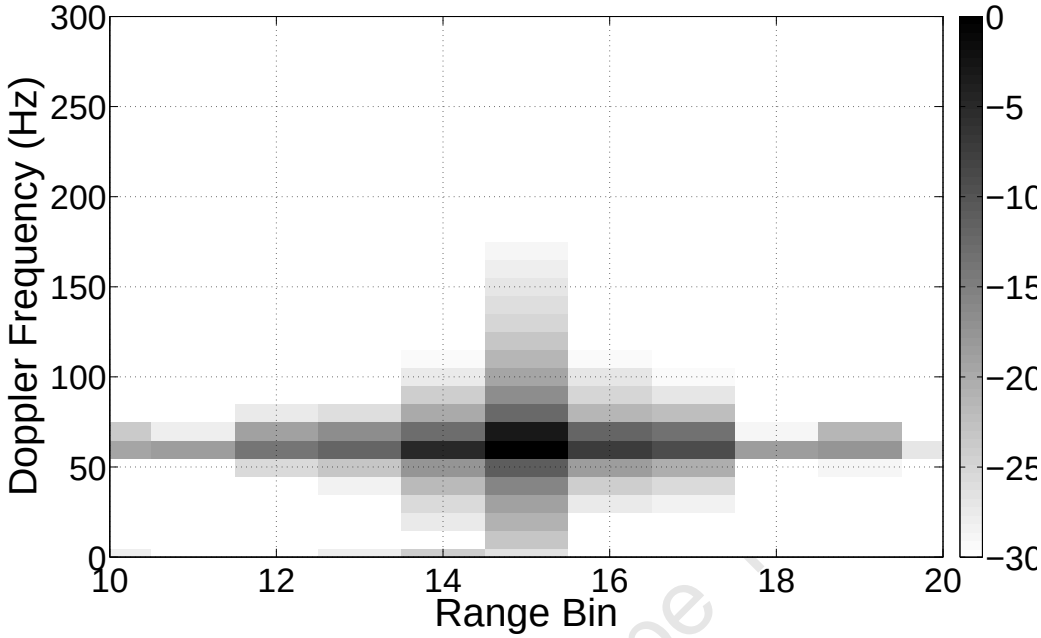

(a) Measured result

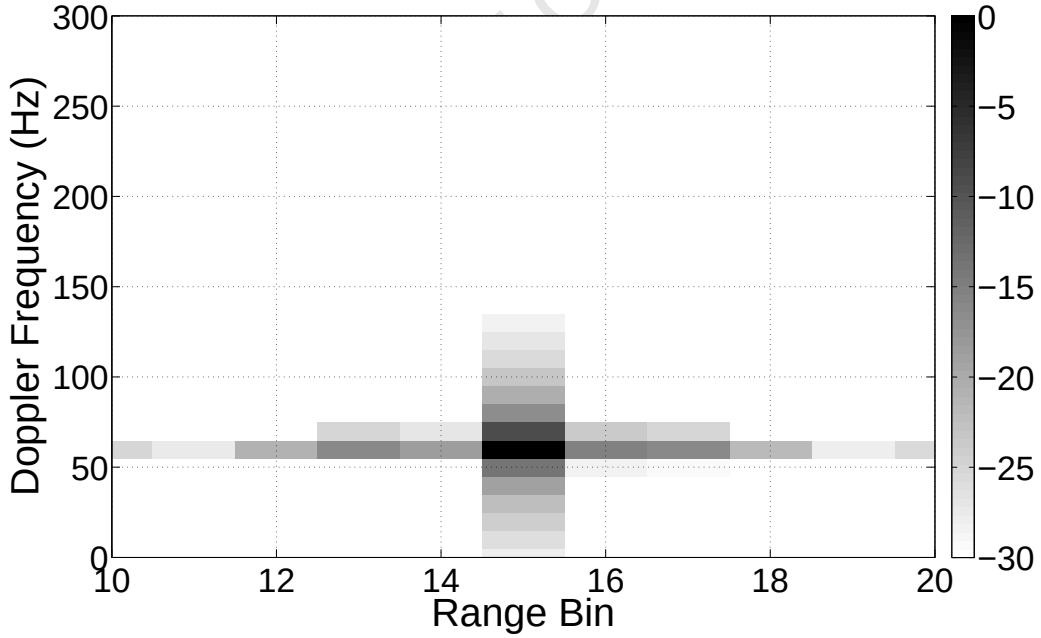

(b) Simulated result

Figure 5.11: Measured and simulated range-Doppler images for netted radar experiment

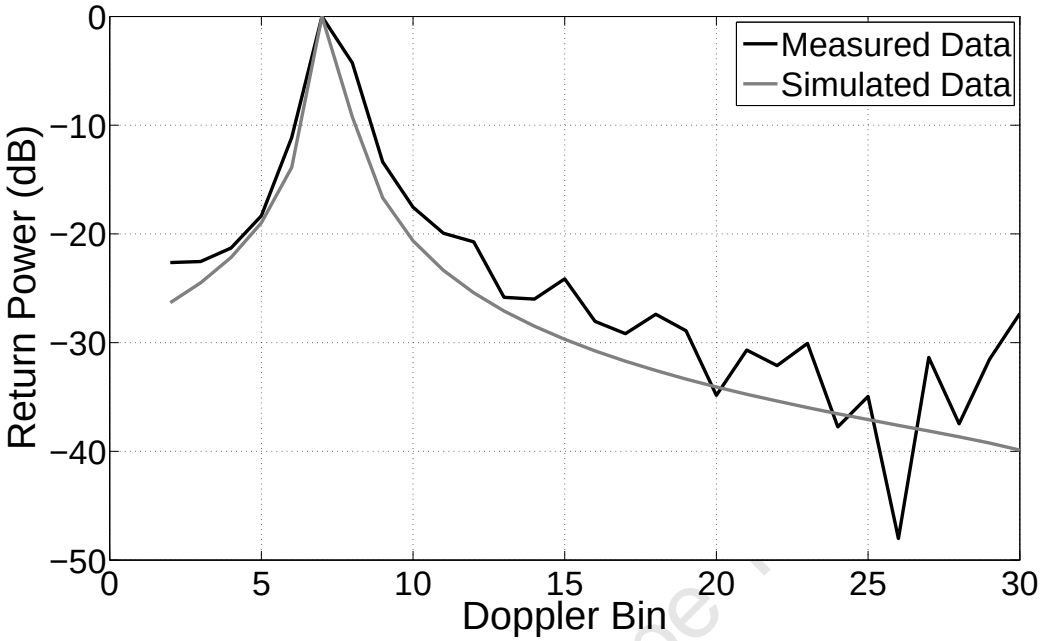

(a) Cut through Doppler bin 7

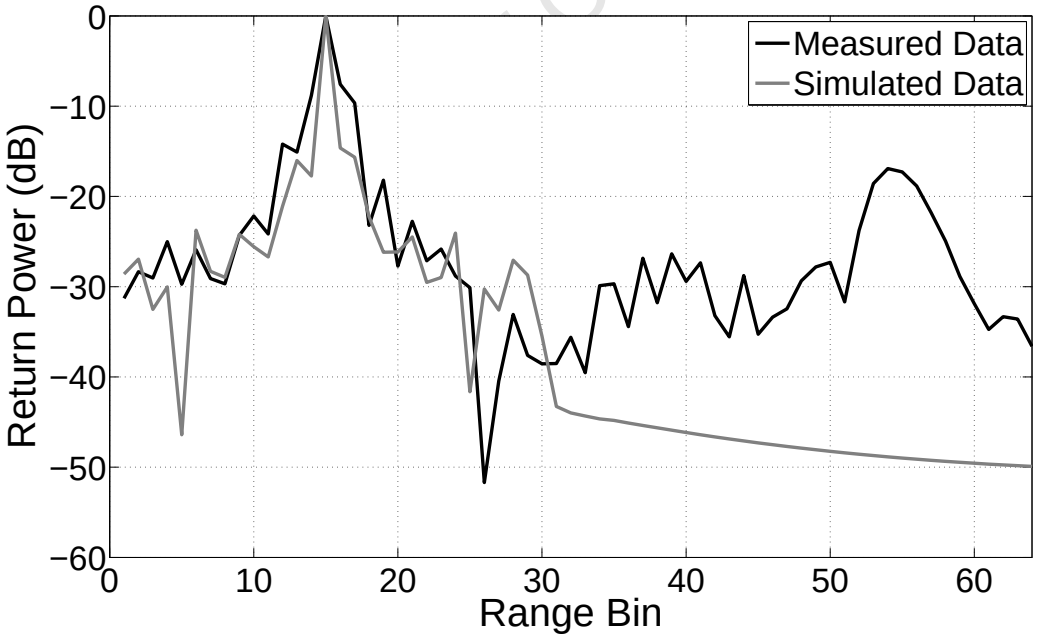

(b) Cut through range bin 15

Figure 5.12: Cuts through netted radar measurement and simulation in range and Doppler

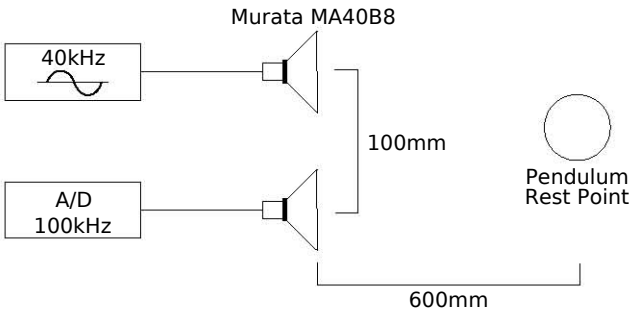

(a) Top view

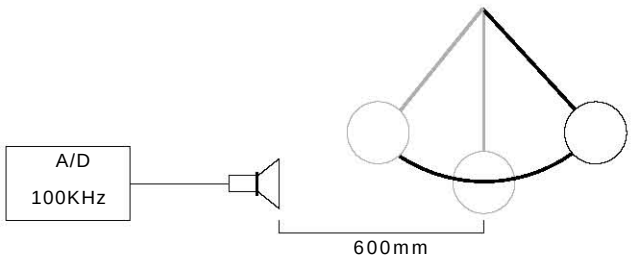

(b) Side view

Figure 5.13: Experimental setup for CW sonar system

$12V_{p-p}$ sinusoid was generated with a signal generator and used to drive a Murata MA40B8S [206] piezoelectric sonar transducer. A spherical pendulum was suspended with its rest point 600mm from the center of the sonar baseline. The return signal captured with Murata MA40B8R transducer, amplified and sampled at 8 bits. To reduce the effects of the analog sampling process, the signal was sampled at a rate of 200kHz, followed by polyphase downsampling to 100kHz with a steep rolloff. Due to the extremely limited bandwidth, and high quality factor (Q) [83], of the transducers used the received signal was strongly bandlimited. A sample rate of 100kHz was sufficient to capture the received signal without aliasing.

The pendulum was suspended from a fixed point 505mm above the plane of the sonar transducers, and raised to an angle of 37 degrees. The sonar returns were recorded for 8 seconds. The returns were normalized then analysed with the short time Fourier transform (STFT) [207, 29], using transforms of 4096 samples, 50% overlap, and a Hamming [134] window. A simulation was

performed using the FERS simulator, with an extension module to simulate pendulum motion and the results processed in the same way as the measured signal.

Figure 5.14 compares the STFTs of results of the simulation of the sonar system with the measured results. The results show a frequency modulation of the return signal due to motion of the target, and an unmodulated version of the signal received directly from the transmitter. The simulated and measured results show identical overall structure, peak Doppler (332 ± 0.6Hz) and ratio between the direct and return signals.

Using the differential equation of pendulum motion,

$$\frac{d^2\theta}{dt^2} = -\frac{g}{l}\sin\theta, \tag{5.6}$$

where $g = 9.81\text{ms}^{-1}$ and $l = 505$mm, the maximum velocity of the pendulum is expected to be 1.41ms^{-1}. The maximum measured bistatic Doppler is therefore expected to be 332.58Hz. This closely matches the maximum Doppler in both the measured and simulated results. While equation 5.6 was used to define the motion in the simulator extension used, the results demonstrate that the baseband Doppler shift algorithm (based on the fractional delay filters described in Section 4.2.4) produces the expected results. These results also highlight the usefulness of the simulator extension mechanism.

5.4 Simulation of Phase Noise Effects

Simulation of the effects of local oscillator phase noise on radar signals is an important feature of the FERS simulator, and the simulation model. The pruned multirate filterbank approach to the generation of synthetic phase noise sequences, as described in Section 3.6, allows simulation of the effects of phase noise in pulsed systems with little increase in simulation time. Appendix A contains two case studies of the results of simulation of phase noise effects. While these results were not directly considered to be part of the verification process, they provide a demonstration that the behaviour of the phase noise generation process is correct.

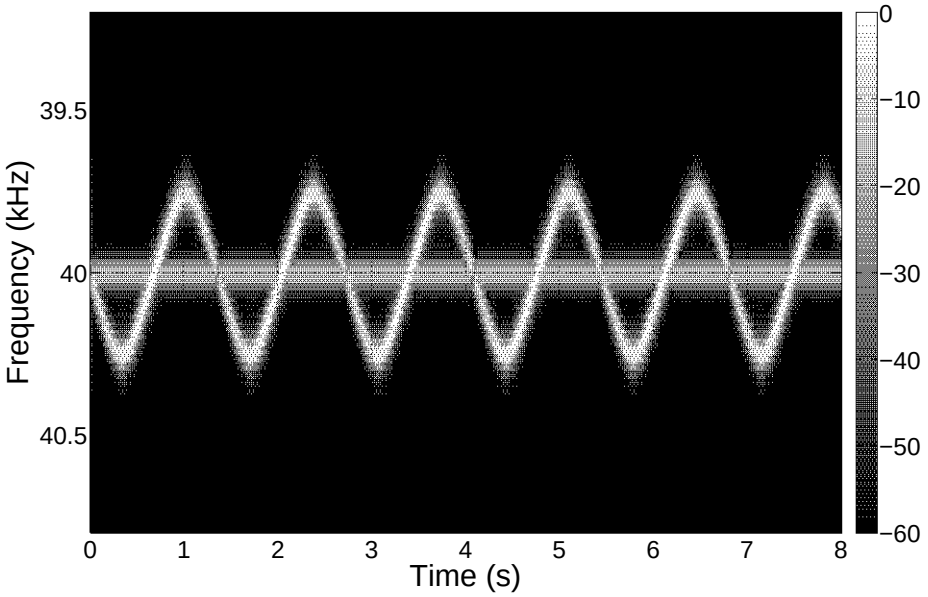

(a) Simulation

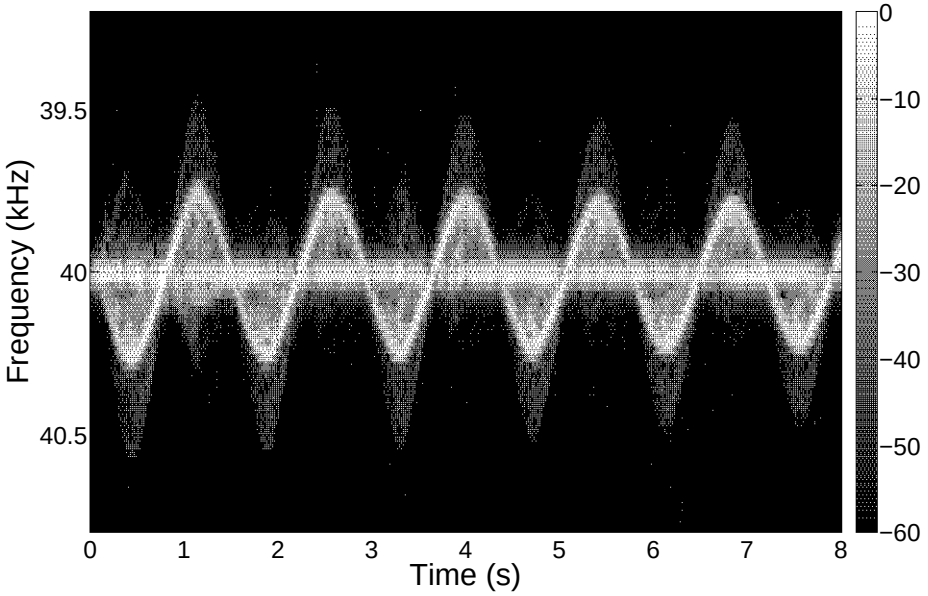

(b) Measurement

Figure 5.14: Comparison of measured and simulated results for pendulum experiment

The results presented in the Appendix demonstrate that the dynamic pruning algorithm effectively preserves long range correlations in $1/f$ noise processes. This can be clearly seen in the long integration time results in the pulse-Doppler radar example (Section A.2), where the long-memory components of phase noise cause increasing degradation of Doppler resolution. If the long-memory nature of $1/f$ noise was destroyed by the generation algorithm, the Doppler resolution would have been observed to improve over long integration times.

5.5 Conclusion

The accuracy of the results of the FERS simulator has been demonstrated by comparing these results to both measurements and theoretical predictions. In the comparison to theoretical predictions, it was found that the simulations of the behaviour of an MTI radar system closely matches the predicted behaviour of such a system. In addition, the phase shift calculations were verified by demonstrating that the simulated results produce a sharp SAR image, with the targets at the expected positions. As the SAR processing was performed with a well validated SAR processor, this strongly suggests that the simulator results are correct to within the parameters used in SAR processing.

Comparison of simulation results to measurements taken using the NetRad netted radar also show a high degree of correspondence. The postion of range and Doppler peaks match between the simulated and measured results (figure 5.11), and cuts through these peaks show a nearly identical structure (figure 5.12). Further comparisons with measurements taken using a bistatic sonar system demonstrate the correctness of the baseband Doppler shift algorithm, and the implementation of this algorithm using FIR fractional delay filters.

The process of validating the accuracy of FERS is ongoing. Preliminary results of work currently underway at UCT, by Yoann Paichard and Sebastiaan Heunis, have suggested the FERS simulations of an FM radio based passive coherent location (PCL) system match the expectations of theory. The use of FERS in this research is likely to provide a large amount of validation data, from both theory and measurements.

Chapter 6

Conclusion

6.1 Summary and Contributions

This thesis describes the design and implementation of FERS, a flexible and extensible signal level radar simulator. FERS is capable of simulating a diverse range of radar system designs and radar phenomena, including arbitrary numbers of targets, transmitters and receivers. The simulator's extensibility and flexibility make it ideal for research and development — supporting the student or engineer in effectively exploring the radar design space without artificial constraints on system parameters.

FERS is also suitable for education and training. In a university environment, the simulator could be used to demonstrate the effects of radar parameters on output signals, to generate example signals for radar signal processing exercises, or to provide a means for the student to test the performance of hypothetical radar systems. Coupled with a suitable graphical user interface (GUI) and signal processor, FERS could be used for training radar operators and technicians.

Chapter 1 introduces the work, and describes the different philosophies and approaches to radar systems. The diverse nature of radar is presented to the reader, and a justification for the requirements of flexibility and extensibility is presented. The introduction also describes the structure of this thesis, and briefly lists the contributions of this work to the field of radar

simulation.

A discrete-time model for radar simulation is presented in **Chapter 2**. The emphasis of the model is on providing maximum flexibility while not significantly limiting descriptive power. The structure of the model is described, with the details of each section of the model clearly explained. The key contributions of this chapter are:

- A radar simulation model without restrictions on the configuration of the system under simulation. The model places no restriction on the system geometry; the number of transmitters, receivers and targets; the transmitted waveform; or the key parameters of the simulated system.
- The use of the superposition principle to reduce the simulation of the return of a multistatic radar system into a linear time problem, without placing any restrictions on the system being simulated.

Chapter 3 describes the approach used for the generation of phase noise sequences in FERS. A model of the performance of frequency sources tailored to radar systems, including both random and deterministic effects, is developed. This model draws on both the radar field and the time and frequency field, and presents the key parameters of oscillator performance in a manner which is relevant to radar simulation. A quantitative study of a variety of algorithms for the generation of synthetic phase noise sequences is presented. Chapter 3 describes two contributions to the radar field:

- A multirate filterbank for the efficient generation of phase noise sequences matching the measured performance of high precision oscillators. While the generation of coloured noise using multirate filterbanks has been described in the literature [7], the structure presented here is the first which allows the power spectral density slope to change between bands, modelling the performance of real oscillators. The use of multirate filters for synthetic phase noise generation has not been described in the literature in the context of radar simulation.
- A novel extension of the multirate approach to the generation of phase noise sequences allowing the efficient generation of *sparse* or *pulsed*

coloured noise sequences. This approach is more efficient than any other currently available method for generating sparse sequences of coloured noise while preserving long term correlations.

The implementation of the simulation model as a C++ program is described in **Chapter 4**. A high-level overview of the software design is presented, and the simulator inputs and outputs described in detail. The chapter examines the design of the two stages of simulation (the world model and the signal renderer), and presents pseudocode for the top level flow of each stage. Performance figures for single- and multiprocessor machines and the design and implementation of an algorithm for the windowed design of FIR fractional delay filters are presented. The key contributions of this chapter are:

- The mapping of the multistatic radar simulation problem onto multi-threaded computers by exploiting the superposition property of linear systems.
- The use of a table of FIR fractional delay filters to efficiently and accurately apply a subsample accurate group delay to arbitrary digital signals. The use of this approach in a radar simulator has not been described in the open literature, and is believed to be a novel contribution to the field of radar simulation.

Chapter 5 presents selected results from the validation of the simulator. Simulated results are compared against both theoretical expectations, and measurements from a multistatic radar system. The use of the FERS for simulating the effects of local oscillator phase noise on the performance of a pulse-Doppler radar system is described. In addition, Appendix A describes the use of the simulator as part of a stochastic simulation of the effects of phase noise on Synthetic Aperture Radar.

6.2 Future Work

This section describes possible future directions for research into radar simulation. Areas for future work can be divided into two categories: extension of the scope and accuracy of the simulator, and uses of the simulator to obtain a better understanding of radar phenomena.

Radio Propagation Modelling

The free space propagation equation, as described in Section 2.2.2, does not consider the effects of terrain and the atmosphere on the propagation of radar signals. A more complete model, including simulation of terrain effects, would improve the applicability of simulator results to real-world radar systems. Research is currently underway at UCT, by Gunter Lange and others, into combining the results of the propagation simulator AREPS [208, 209] with the results of FERS in the context of an FM based passive coherent location (PCL) system.

The extension of this work to the development of a simple method for combining the results of the two simulations would increase the value of FERS in terrain-dominated simulations. Alternatively, an open-source terrain effect model could be implemented as an extension to FERS. In order for such a model to be valuable, it would need to consider effects which are not included in AREPS — such as propagation in indoor and built up environments.

The inclusion of a complete channel model in FERS would also increase the value of the simulation in some circumstances. Such a model could consider fading, scattering and dispersion in environments where these effects are relevant to the performance of radar systems.

Global Illumination

The expansion of the environment model (Section 2.2) to consider multiscatter effects (Section B.3 in Appendix B) would improve the accuracy of the simulation algorithm in some radar applications. The most promising source of algorithms for efficient implementation of multiscatter is likely to be the

computer graphics field of global illumination (see [210] and [211] for good introductions to the topic). Specifically, indirect illumination algorithms such as radiosity and ray tracing are likely to prove to be adaptable to the radar simulation problem.

Section B.3 provides a justification for the exclusion of multiscatter effects from the simulation model described in this work. Where the assumptions made in this section do not hold, however, the implementation of a global illumination based simulation of multiscatter effects will increase the accuracy of radar simulation. In addition, global illumination algorithms could provide an extension of the limited multipath simulation model described in Section 2.2.6.

Target and Antenna Modelling

The extension of FERS to include electromagnetic simulation capabilities would enable the simulator to calculate bistatic RCS patterns and antenna radiation patterns dynamically, based on the requirements of the simulations. A simple way to achieve this goal would be the development of an extension to FERS to allow integration with an existing electromagnetic simulator (such as FEKO [212]). The implementation of a method of moments or physical optics code as an extension to FERS would also be desirable.

Optimisation of Radar Systems

The number of parameters which must be considered during the development and deployment of radar systems makes direct optimisation of designs prohibitively difficult, especially for netted and multistatic designs with large numbers of sensors. Traditional engineering approaches, such as the application of heuristics, allows workable solutions to be found — but these are not likely to be truly optimal.

The use of a simulator such as FERS in the loop of powerful optimisation approaches, such as genetic algorithms, could allow better optimisation of system parameters and improve the performance-to-cost ratio of radar systems. A future project at UCT will look at the use of a combination of FERS and

AREPS for the optimisation of the placement of sensors in a PCL system.

Appendix A

Stochastic Simulation of Phase Noise Effects

A.1 Introduction

This chapter presents an example of the use of FERS to investigate aspects of radar performance which are not well covered by theory. In the case studies presented here, FERS is used to examine the effects of phase noise on two radar systems: a VHF SAR system, and a multistatic pulse-Doppler system.

The pulse-Doppler case study presents simulations of the effects of phase noise on the Doppler resolution of a multistatic radar system, modelled after NetRad [76, 205, 77, 78]. Traditional theory predicts [26] that the Doppler resolution of such a system increases with integration time. The simulations presented in this chapter examine the validity of that assumption in the presence of phase noise generated by long-memory processes.

In the SAR case study, the effects of phase noise on Synthetic Aperture Radar (SAR) processing are investigated, with the goal of deriving relationships between the properties of the phase noise and SAR performance. As in Section 5.2.2, the SASAR VHF system has been used as a model for the simulation parameters.

In this chapter, the stochastic simulation (Monte Carlo) approach is used to analyse the performance of radar systems in the presence of phase noise.

This approach is necessary due to the random nature of phase noise — each run will produce different results, but general rules about performance can be extracted from the results of multiple runs. A similar approach, with different details, was used to analyse the performance of SAR systems in the presence of Gaussian phase deviations by Greene and Moller [213].

The goal of this chapter is to illustrate the type of simulation and analysis which can be performed with FERS, that can not be performed with other widely available radar simulators.

A.2 Bistatic Pulse-Doppler Radar

As illustrated in figure 3.1 on page 43 the detectability of targets in a pulse-Doppler radar system can be compromised by Doppler spreading of stronger targets in the same range bin. This spreading is typically caused by local oscillator phase noise. This effect is especially important in multistatic radar systems, as the direct signal from a transmitter to a receiver is likely to be much higher in power than any target responses, and is not rejected by a T-R switch as in traditional monostatic systems.

In an ideal system, the visibility of targets separated in range and Doppler from these high power direct signals is limited only by the ambiguity function of the transmitted waveform. Phase noise on the receiver's local oscillator, however, will spread these signals out over more Doppler bins than predicted by the ambiguity function, effectively reducing the visibility of targets close to the direct path in range and Doppler.

In this case study, FERS was used to simulate the effects of phase noise on a multistatic radar system similar to NetRad. The transmitter was assumed to contain an ideal local oscillator and the phase noise on the receiver's oscillator was chosen to match the measured phase noise on the NetRad system. Figure A.1 shows the phase noise curve used for simulations, based on the phase noise measured between two nodes in the NetRad system.[1]

The simulator was configured with two nodes: a receiver, and a single

[1]Thanks to Stephan Sandenbergh at the University of Cape Town for performing these measurements and sharing the results

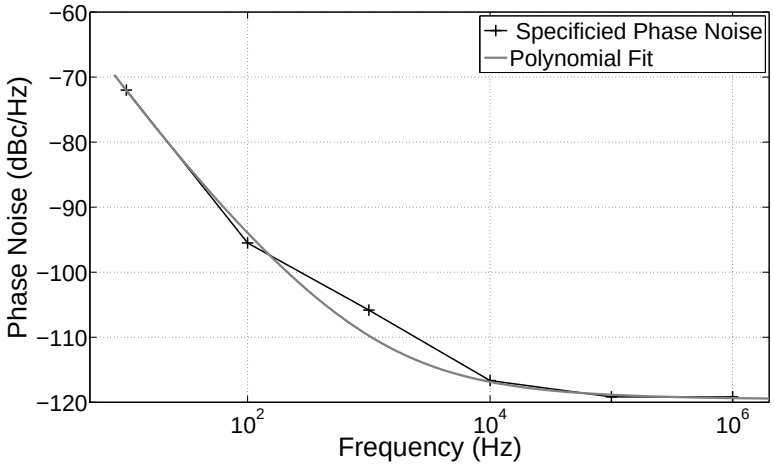

Figure A.1: Measured phase noise of NetRad cable-based clock transfer system, and polynomial fit

transmitter 55m away in the main beam of the receiver. No targets or multipath effects were included in the simulation. The results from each range-Doppler bin were taken as the mean of the return powers over 50 simulations.

A.2.1 Simulation Results

Figure A.2 illustrates the direct signal from transmitter to receiver in range-Doppler space, with the Doppler scale in Hertz. The intensity and contours represent power normalized to 0dB, with contours at 10dB intervals. In the ideal case, with zero phase noise, each of these plots would be a single horizontal line, with the peak Doppler sidelobe below −200dB.

For an integration time of 0.1 seconds (figure A.2(a)), Doppler sidebands above −50dB extend up to 100Hz above and below the zero Doppler line. Increasing the integration time to one second (figure A.2(b)) reduces the power in the sidelobes, effectively increasing the detectability of targets close to the transmitter. Further increases in the integration time do not improve the sensitivity — a slight decrease is evident for 10s of integration (figure A.2(c)), with a significant decrease for 100s (figure A.2(d)).

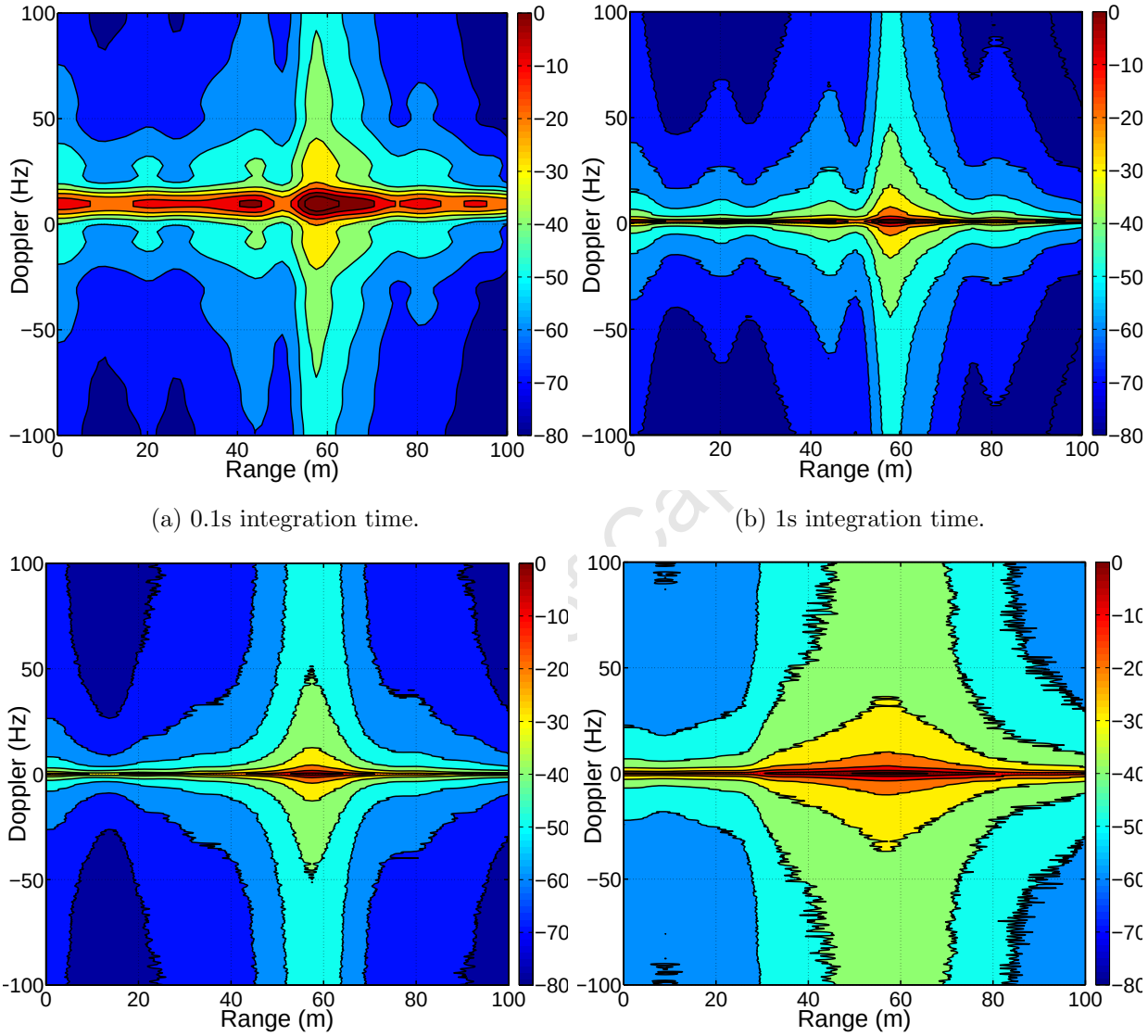

(a) 0.1s integration time.

(b) 1s integration time.

(c) 10s integration time.

(d) 100s integration time.

Figure A.2: Direct signal power spreading in range and Doppler versus integration time for measured NetRad phase noise

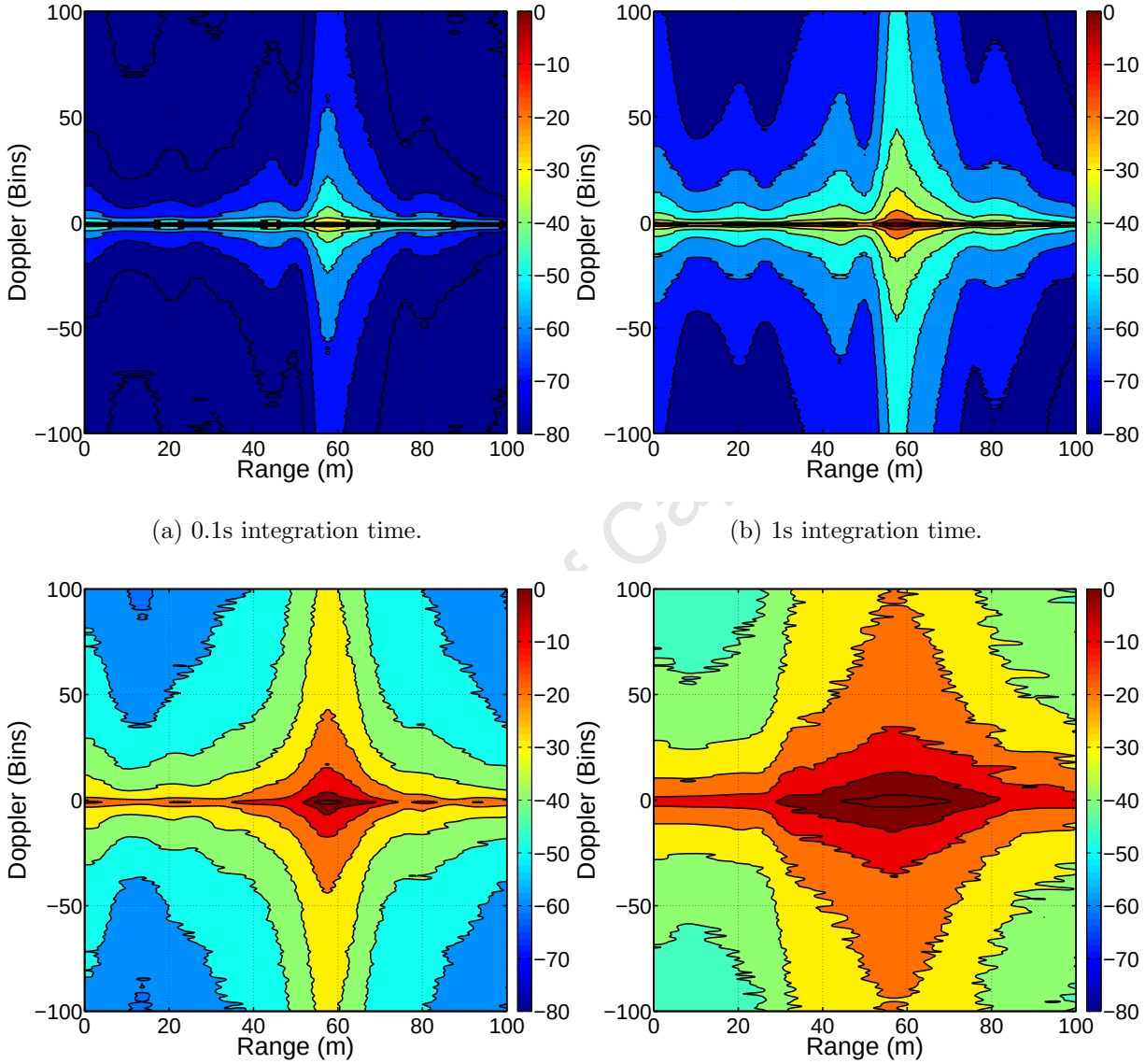

(a) 0.1s integration time.

(b) 1s integration time.

(c) 10s integration time.

(d) 100s integration time.

Figure A.3: Direct signal power spreading in range and Doppler bins

The mean of white Gaussian phase noise tends towards a constant with increased integration time. For integration times during which the phase noise is dominated by noise of this type, increasing the number of samples to be integrated reduces the spread of the received signal in Doppler. This effect is evident between the integration times of 0.1s (figure A.2(a)) and 1s (figure A.2(b)). For longer integration times, long-memory phase noise processes dominate and longer integration times no longer improve performance (figure A.2(c)). The means of these processes (where $\alpha \leq 1$) do not tend toward a constant, therefore longer integration times do not improve performance. For the longest integration times (figure A.2(d)), random walk FM dominates and performance deteriorates strongly with integration time.

Figure A.3 illustrates 100 Doppler bins (pixels) either side of zero for the same data as figure A.2. The figure clearly illustrates that increasing the number of Doppler bins per Hz of Doppler, and hence increasing the integration time, does not improve the detectability of targets positioned close to the transmitter in range and Doppler.

While the integration times presented in these results are much longer than typically used in pulse-Doppler systems, these results illustrate the challenges of achieving extremely high Doppler resolution in real systems, and the use of FERS in simulating the effects of phase noise of the performance of radar systems. Simulations of lengths on the order of many seconds clearly demonstrate the advantages of the multirate noise generation algorithm with dynamic pruning (see Section 3.6 on page 73), which preserves correlations and long-memory behaviour over long simulation times without requiring prohibitively large amounts of computing time.

A.3 Synthetic Aperture Radar (SAR)

Due to the integration of large numbers of pulses, SAR signal processing is highly resistant to additive white noise. The SNR improvement factor for a

typical SAR system is [190]:

$$\text{Improvement Factor} = \frac{\tau_i}{\tau_0}\frac{PRF\ L}{v}, \tag{A.1}$$

where τ_i and τ_0 are the uncompressed and compressed pulse lengths, PRF is the system pulse repetition frequency, L is the synthetic aperture length, and v is the velocity of the platform. SAR processing is similarly resistant to uncorrelated phase error, but where these errors are large they cause spreading of the effective beam, decrease the ratio between mainlobe and sidelobe energy, and increase the peak sidelobe level [190, 213].

Phase errors which are correlated between pulses ($\alpha < 2$) are not effectively cancelled out by integration in SAR processing, and therefore have a much larger effect on SAR performance than white Gaussian phase errors ($\alpha = 2$). It is therefore interesting to consider the effects of phase errors introduced by local oscillator phase noise, which show strong correlations between pulses in many radar oscillator designs.

Figure A.4 illustrates the effects of phase noise on the cross sections of a single target in two cases. In each case 5 runs are presented, showing the variation in performance between runs. Figure A.4(a) illustrates the effects of random walk phase modulation ($\alpha = 0$) at -40dBc/Hz at 10Hz — the peak sidelobe level and total sidelobe energy are significantly increased compared to the ideal response from the same system (figure 5.6 on page 113). The effects of flicker frequency modulation ($\alpha = -1$) at -60dBc/Hz at 10Hz are illustrated in figure A.4(b). Several effects of phase errors are evident in this image, including the displacement of the mainlobe from its expected position (beam canting), a large increase in sidelobe energy, and a significant increase in peak sidelobe level.

The large changes in performance between runs suggest that statistical tools are required to describe the effects of phase noise on the structure of SAR returns. Measurement of the properties of these effects using stochastic simulation is straightforward with the FERS simulator.

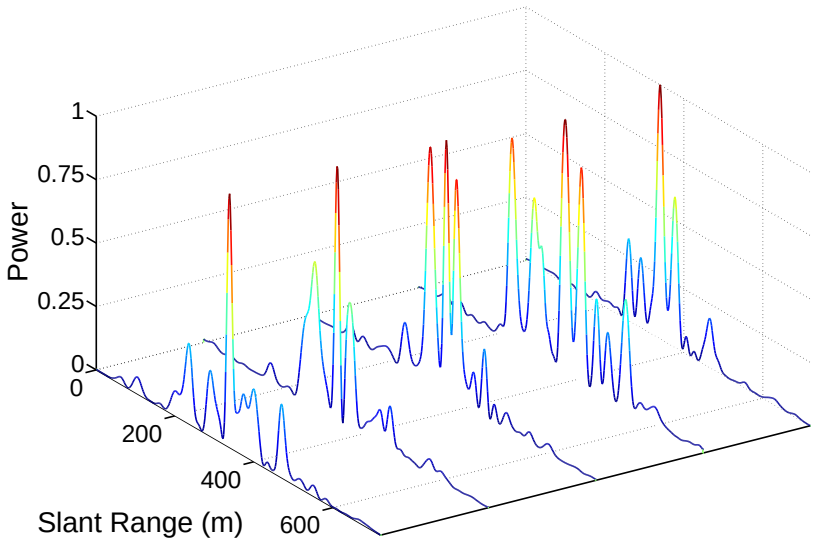

(a) -40dBc/Hz at 10Hz, $\alpha = 0$

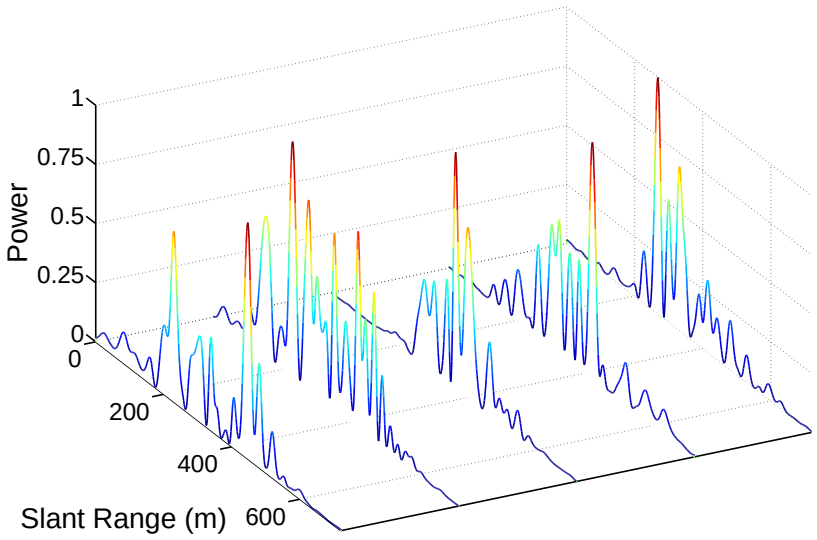

(b) -60dBc/Hz at 10Hz, $\alpha = -1$

Figure A.4: Cross sections of a single point in a SAR image

Equivalence of Phase Noise and Uncorrected Motion Errors in SAR

Expressing focused SAR processing as a weighted sum [190, 191]:

$$\sum_n S_n W_n e^{-j\phi_n}, \tag{A.2}$$

where S_n is the nth pulse, and W_n and ϕ_n are the nth weighting and phase correction factors, the effects of phase noise can be expressed as:

$$\sum_n S_n W_n e^{-j\phi_n} e^{-j\theta_n}, \tag{A.3}$$

$$= \sum_n S_n W_n e^{-j(\phi_n+\theta_n)} \tag{A.4}$$

where θ_n is the phase deviation due to local oscillator phase noise. From equation A.3, it can be observed that the effects of phase noise are equivalent to the effects of phase errors from other sources (such as uncorrected motion errors). The receiver is unable to differentiate between phase errors caused by motion, and phase errors caused by noise on its oscillators.

A phase deviation of θ_n radians is equal to a deviation of

$$\text{Path deviation} = \frac{\theta_n c}{2\pi f_0} \tag{A.5}$$

meters along the slant range direction, where f_0 is the system's centre frequency and c is the propagation speed in the medium.

A.3.1 Results of Stochastic Simulation

A key figure of merit for SAR systems is the integrated sidelobe ratio (ISLR), the ratio between the power in the mainlobe and the integrated power across all sidelobes. Because the ISLR changes between simulation runs — due to the stochastic nature of phase noise — it is necessary to consider the distribution of the ISLR over a large number of simulation runs.

For each simulator run, an image of a single target at a slant range of 8000m with an effective aperture length of 360m was simulated with FERS and processed with G2. The parameters of the simulated system are listed

Table A.1: Mean integrated sidelobe ratios (dB) versus noise amplitude and category (α)

Noise amplitude dBc/Hz at 10Hz	**Noise Category (α)**				
	2	**1**	**0**	**-1**	**-2**
-100					4.79
-90					-0.72
-80				5.13	-4.66
-70				1.47	-5.29
-60			5.23	-4.52	
-50			4.91	-7.6	
-40		5.23	-2.51		
-30		4.73	-5.54		
-20	5.18	-6.46			
-10	-7.13				

in Table 5.1 on page 111. Fifty runs were used for each combination of noise amplitude and noise category. Where a target was discernable from the majority of simulation runs, the mean and standard deviation of the ISLR was recorded. The simulation runs were collected using a GNU Octave script to call FERS, followed by a program to translate between FERS output and the format expected by G2, followed by the G2 SAR processor.

Tables A.1 and A.2 present the results of the simulations. Values have been omitted from the table where no target was discernable in the output image, and where there was no significant ISLR reduction due to phase noise. A histogram of the measured ISLR for $\alpha = 0$ and noise amplitude of -40dBc/Hz at 10Hz and 200 simulator runs is shown in figure A.5. The ISLR in this case is normally distributed, with a confidence of 0.71.

A strong correlation between the ISLR at a given noise amplitude and the noise category is evident. This strongly indicates that SAR performance is dependent on the power spectral density (PSD) of the local oscillator phase noise ($S_x(f)$ in Chapter 3).

As α decreases, the PSD of a phase noise sequence becomes more localized around the carrier, and by the Einstein-Wiener-Khinchin [111, 60] theorem and the localization property of the DFT [29], the autocorrelation function

Table A.2: Standard deviation of integrated sidelobe ratios (dB) versus noise amplitude and category (α)

Noise amplitude dBc/Hz at 10Hz	**Noise Category (α)**				
	2	**1**	**0**	**-1**	**-2**
-100					0.59
-90					3.85
-80				0.12	2.94
-70				2.88	2.74
-60			0.05	2.3	
-50			0.36	2.72	
-40		0.04	2.8		
-30		0.42	2.57		
-20	0.05	2.22			
-10	1.82				

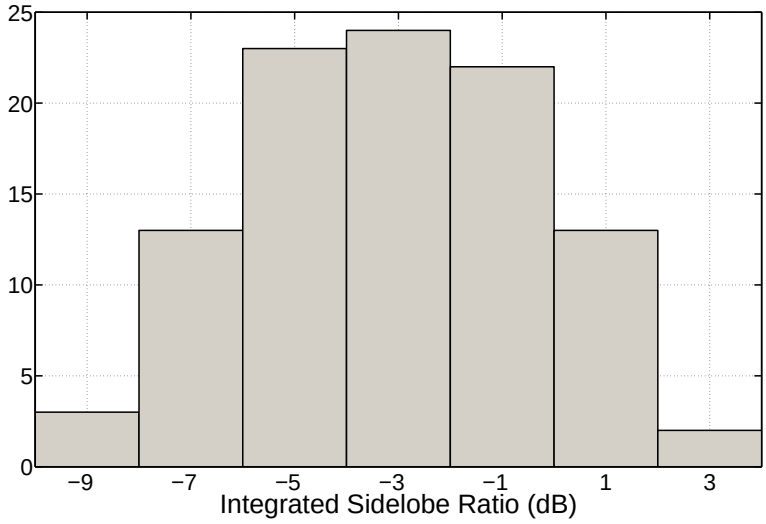

Figure A.5: Histogram of distribution of ISLR for noise amplitude -40dBc/Hz and $\alpha = 0$ (100 experiments)

of the noise becomes less localized. Correlation between the phase noise in adjacent pulses is therefore increased for decreasing α, and integration becomes less effective at cancelling out phase errors.

A.4 Conclusion

The phase noise simulation capabilities of the FERS simulator can be used with stochastic simulation approaches to explore the effects of phase noise on radar systems. In SAR, this approach has been used to demonstrate the dependence of ISLR on the shape of the PSD of phase noise, and highlight the importance of the specification of complete phase noise curves (or, equivalently, complete Allan variance [102, 103] or modified Allan variance [104] curves) for oscillators in radar systems. In pulse-Doppler radar, this approach has been used to demonstrate the limitation of Doppler resolution due to phase noise. While these qualitative conclusions are not new, the ability of the FERS to obtain quantitative predictions of radar performance in the presence of phase noise exceeds that of any simulator described in the literature.

FERS is a powerful tool, which allows the radar engineer to apply powerful techniques such as stochastic simulation to explore the radar system design space, both qualitatively and quantitatively.

Appendix B

Limitations of the Simulation Model

B.1 Introduction

This appendix examines the validity of two of the assumptions underlying the superposition model presented in Chapter 2. The assumption of the linearity of propagation of radar signals is examined in Section B.2, and discusses the extension of the model to include effects such as anisotropy and dispersion. Section B.3 examines the validity of the exclusion of multiscatter propagation paths from the environment model.

B.2 Linearity

The application of the principle of superposition to radar simulation requires that target interaction and propagation are linear in the sense that they must meet the requirements of homogeneity:

$$f(\alpha x) = \alpha f(x), \tag{B.1}$$

for constant scalar α, and additivity:

$$f(x + y) = f(x) + f(y). \tag{B.2}$$

The superposition model does not assume that the transmitter is linear, as any output that can be produced by a non-linear transmitter can be produced by a linear transmitter with the appropriate input signal. As expressed in equation 2.4 on page 13 the receiver model operates on the summed signal from all propagation paths, and hence can include non-linear effects without violating the validity of the superposition assumption. The only non-linear process included in the receiver model as described in Section 2.3.2 is quantization of the signal, but the simulator extension mechanism can be used to include simulation of other nonlinear effects (such as distortion introduced by the LNA).

For propagation, the superposition model assumes that the medium is linear. The electric field intensity $\mathbf{E}$ and electric flux density $\mathbf{D}$ are assumed to be related by:

$$\mathbf{D} = \epsilon \mathbf{E}, \tag{B.3}$$

where ϵ is the permittivity of the medium and is not dependent on $\mathbf{E}$ or $\mathbf{B}$. Similarly, the magnetic field density $\mathbf{B}$ and and magnetic field intensity $\mathbf{H}$ are related by:

$$\mathbf{B} = \mu \mathbf{H}, \tag{B.4}$$

where μ is the permeability of the medium and is not dependent on $\mathbf{E}$ or $\mathbf{B}$. The permittivity ϵ and permeability μ are included in the simulation model through the definition of the propagation speed in the medium c:

$$c = \frac{c_0}{\sqrt{\frac{\mu}{\mu_0}\frac{\epsilon}{\epsilon_0}}} \quad \text{ms}^{-1}, \tag{B.5}$$

where c_0 is the speed of light in a vacuum and μ_0 and ϵ_0 are the permeability and permittivity of free space, respectively. The superposition model does not require the permittivity ϵ and permeability μ to be constant or scalar — propagation effects such as anisotropy (where ϵ and μ are second rank tensors [25]) and dispersion (where ϵ and μ are functions of frequency) can be included in the model. These effects are not currently considered, but could be implemented in the current simulation architecture (see Section 6.2 on page 129).

For target interactions, it is assumed that the bistatic RCS (σ) of the target is constant at a pair of arrival and departure angles, and does not depend on the power density at the target.

B.3 Multiscatter

The environment model as described in Section 2.2 considers only direct (transmitter-receiver) and first order (transmitter-target-receiver) propagation paths. For a simulation with T transmitters, R receivers and S scatterers (targets), the total number of propagation paths considered is:

$$N = TR + TSR. \tag{B.6}$$

The number of responses is linear in T, S and R, and hence the simulation problem can be considered to run in linear time (see Section 4.2.5). The inclusion of multiscatter paths — where reflections from one target to others are included increases the number of paths to:

$$N = TR + \sum_{k=0}^{M-1} TS(S-1)^k R, \tag{B.7}$$

where paths containing a total of M targets are considered. The inclusion of these paths makes the environment model computationally equivalent to the radiosity algorithm [210, 211] used in computer graphics for global illumination calculations.

While the environment model, as described in Section 2.2, includes only direct and single target paths, it can be extended to any value of M (as defined in equation B.7). When $M > 1$, the simulation runtime becomes $O(S^M)$ — greatly increasing the required number of operations for large S. The extension of the model to utilise full global illumination provides scope for future work (see Section 6.2).

B.3.1 The Effects of Multiscatter

The bistatic radar equation (see Section 2.2.2 on page 23) can generalised to include multiscatter paths for n targets as follows. The power density at the first scatterer in a multiscatter path is:

$$S_1 = \frac{P_t G_t}{4\pi R_{t1}^2}, \tag{B.8}$$

where P_t is the transmitted power, G_t is the gain in the direction of the first scatterer, and R_{t1} is the range from the transmitter to the first scatterer. The power re-radiated in the direction of the second scatterer is:

$$P_{12} = \sigma_{12} S_1, \tag{B.9}$$

where σ_{12} is the bistatic RCS for the relevant angles, which causes the power density at the second scatterer of:

$$S_2 = \frac{\sigma_{12} S_1}{4\pi R_{12}^2}, \tag{B.10}$$

where R_{12} is the range for scatterer 1 to scatterer 2. The power density at the nth scatterer is therefore:

$$S_n = \left(\frac{P_t G_t}{4\pi R_{t1}^2}\right) \prod_{k=2}^{n} \frac{\sigma_{(k-1)(k)}}{4\pi R_{(k-1)(k)}^2}, \tag{B.11}$$

producing the power received by the receiver:

$$P_r = S_n \frac{\sigma_{nr}}{4\pi R_{nr}^2} \frac{G_r \lambda^2}{4\pi}, \tag{B.12}$$

where G_r is the gain of the receive antenna in the direction of the nth scatterer. The complete expression for the received power along a path with n targets is:

$$P_r = \left(\frac{1}{4\pi}\right)^{n+2} \frac{P_t G_t}{R_{t1}^2} \frac{G_r \lambda^2 \sigma_{nr}}{R_{nr}^2} \prod_{k=2}^{n} \frac{\sigma_{(k-1)(k)}}{R_{(k-1)(k)}^2}. \tag{B.13}$$

This formula for the radar equation assumes, as does the standard bistatic

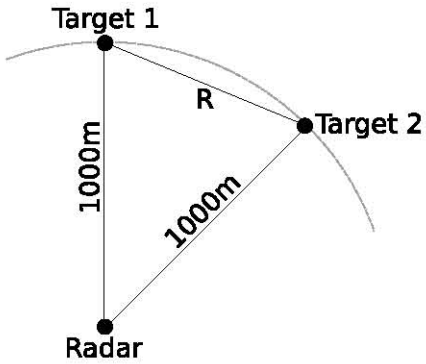

Figure B.1: Geometry of multiscatter example

radar equation, that all ranges are sufficiently large that far field antenna gain and RCS patterns can be used. For multiscatter environment where this does not hold for targets, the simulator requires the interactions to be modelled externally and encapsulated in the bistatic RCS of a single target.

Multiscatter paths can have a substantial effect in environments with large number of closely spaced targets, such as SAR [214]. In other typical radar scenarios, however, the effect of multiscatter can be considered to be small, and simulation with only the single target paths will not cause appreciable errors. Consider the example geometry in figure B.1, the ratio between the power received along the single target paths and the power received from the multiscatter path is large for all R where the far field assumption holds and equation B.13 is valid. For $R = 1$m, the single target returns are 28dB stronger than the multiscatter returns — and 68dB stronger at $R = 10$m.

References

[1] T. Balz, "Real-time SAR simulation on graphics processing units," in *EUSAR 2006: 6th European Conference on Synthetic Aperture Radar*, 2006.

[2] R. Lengenfelder, "The design and implementation of a radar simulator," Master's thesis, University of Cape Town, Sep. 1998.

[3] D. B. Leeson and G. F. Johnson, "Short-term stability for a doppler radar: Requirements, measurements and techniques," *Proceedings of the IEEE*, vol. 54, pp. 244–248, Feb. 1966.

[4] J. R. Vig, "Quartz crystal resonators and oscillators for frequency control and timing applications: A tutorial," U.S. Army Communications-Electronics Command, Jan. 2000.

[5] "A guide to understanding and characterizing timing jitter," Tektronix, Inc., http://www.tektronix.com/jitter/, Tech. Rep., 2003.

[6] M. Brooker and M. Inggs, "Efficient generation of f^{α} noise sequences for pulsed radar simulation," *Accepted for Publication, IEEE Transactions on Aerospace Electronic Systems*, 2008.

[7] J. Park, K. Muhammad, and K. Roy, "Efficient modeling of $1/f^{\alpha}$ noise using multirate process," *IEEE Transactions on Computer-Aided Design of Integrated Circuits and Systems*, vol. 25, no. 7, pp. 1247–1256, Jul. 2006.

[8] *Maxim DS4026 10MHz to 51.84MHz TCXO*, Dallas Semiconductor, 2007.

[9] J. A. Scheer, "Timing jitter effects," in *Coherent Radar Performance Estimation*, J. A. Scheer and J. L. Kurtz, Eds. Artech House, 1993, ch. 4.

[10] J. M. Horrell, "Range-doppler synthetic aperture radar processing at vhf frequencies," Ph.D. dissertation, University of Cape Town, May 1999.

[11] H. D. Griffiths, "Bistatic and multistatic radar," University College London, Tech. Rep., 2002.

[12] J. Meyer-Hilberg, "Pirdis: A new versatile tool for SAR/MTI systems simulation," in *EUSAR 2006: 6th European Conference on Synthetic Aperture Radar*, 2006.

[13] L. Sevgi and A. S. Tanal, "Surface wave HF radar simulator," in *IEEE Radar 1997*, 1997.

[14] R. R. Boothe, "A digital computer program for determining the performance of an aquisition radar through application of radar detection probability theory," U. S. Army Missile Command, Redstone Arsenal, Report RD-TR-64-2, Dec. 1964.

[15] P. J. Golda, "Software simulation of synthetic aperture radar," Master's thesis, University of Cape Town, 1997.

[16] G. Franceschetti, M. Migliaccio, D. Riccio, and G. Shirinzi, "SARAS: a synthetic aperture radar (SAR) raw signal simulator," *IEEE Transactions on Geoscience and Remote Sensing*, vol. 30, no. 1, pp. 110–123, Jan. 1992.

[17] G. Franceschetti, A. Iodice, D. Riccio, and G. Ruello, "A 2-D Fourier domain approach for spotlight SAR raw signal simulation of extended scenes," in *2002 IEEE Internation Geoscience and Remote Sensing Symposium*, 2002, pp. 853–855.

[18] C. Capsoni and M. D'Amicio, "A physically based radar simulator," *Journal of Atmospheric and Oceanic Technology*, vol. 15, no. 2, pp. 593–598, Apr. 1998.

[19] F. Xu and Y.-Q. Jin, "Imaging simulation of polarimetric sar for a comprehensive terrain scene using the mapping and projection algorithm," *IEEE Transactions on Geoscience and Remote Sensing*, vol. 44, no. 11, pp. 3219–3234, Nov. 2006.

[20] J. F. Nouvel, A. Herique, W. Kofman, and A. Safaeinili, "Marsis radar signal simulation," in *2003 IEEE International Geoscience and Remote Sensing Symposium, 2003. IGARSS '03. Proceedings.*, vol. 4, Jul. 2003, pp. 2756–2758.

[21] X. Xu and P. Huang, "A new RCS statistical model of radar targets," *IEEE Transactions on Aerospace and Electronic Systems*, vol. 33, no. 2, pp. 710–714, Apr. 1997.

[22] *ISO 9241-11:1998: Ergonomic requirements for office work with visual display terminals (VDTs) – Part 11: Guidance on usability.* International Organization for Standardization, 1998.

[23] *ISO/IEC 14882:2003: Programming languages – C++.* International Organization for Standardization, 2003.

[24] G. E. Moore, "Cramming more components onto integrated circuits," *Electronics*, vol. 38, no. 8, pp. 1–4, 1965.

[25] J. D. Jackson, *Classical Electrodynamics*, 3rd ed. Wiley, 1999.

[26] S. Kingsley and S. Quegan, *Understanding Radar Systems.* SciTech Publishing, 1999.

[27] J. G. Proakis and D. G. Manolakis, *Digital Signal Processing: Principles, Algorithms and Applications.* Prentice Hall, 1996.

[28] C. E. Shannon, "A mathematical theory of communication," *Bell System Technical Journal*, vol. 27, pp. 379–423,623–656, 1948.

[29] A. V. Oppenheim, R. W. Schafer, and J. R. Buck, *Discrete-Time Signal Processing*, 2nd ed. Prentice Hall, 1999.

[30] V. A. Kotelnikov, "On the transmission capacity of the ether and of cables in electrical communications," in *Proceedings of the first All-Union Conference on the technological reconstruction of the communications sector and the development of low-current engineering*, 1933, translation by C C Bissel and V E Katsnelson.

[31] B. M. Oliver, J. Pierce, and C. E. Shannon, "The philosophy of PCM," *Proceedings of the Institute of Radio Engineers*, vol. 36, pp. 1324–1331, Nov. 1948.

[32] W. R. Bennett, "Spectra of quantized signals," *Bell System Technical Journal*, vol. 27, pp. 446–472, 1948.

[33] R. M. Gray and D. L. Neuhoff, "Quantization," *IEEE Transactions on Information Theory*, vol. 44, no. 6, pp. 2325–2384, Oct. 1998.

[34] J. A. Scheer, "A/D conversion effects," in *Coherent Radar Performance Estimation*, J. A. Scheer and J. L. Kurtz, Eds. Artech House, 1993, ch. 5.

[35] J. D. Echard and M. L. Watt, "The quantization noise spectrum of a sinusoid on colored noise," *IEEE Transactions on Acoustics, Speech and Signal Processing*, vol. 39, no. 8, pp. 1780–1787, Aug. 1991.

[36] *IEEE Std 754-1984: Standard for Binary Floating-Point Arithmetic*. The Institute of Electrical and Electronics Engineers, Inc., 1985.

[37] F. Hartwig and A. Lacroix, "The properties of floating point single quantization including under- and overflow," in *Proceedings of the 1996 European Signal Processing Conference*, 1996.

[38] R. Dunay, I. Kollar, and B. Widrow, "Dithering for floating-point number representation," in *1st International Online Workshop on Dithering in Measurement*, Mar. 1998.

[39] W. S. Brown, "A simple but realistic model of floating-point computation," *ACM Transactions on Mathematical Software (TOMS)*, vol. 7, no. 4, pp. 445–480, Dec. 1981.

[40] D. Goldberg, "What every computer scientist should know about floating point," *ACM Computing Surveys*, vol. 23, no. 1, pp. 5–48, Mar. 1991.

[41] E. Hecht, *Optics*, 4th ed. Addison-Wesley, 2002.

[42] R. C. Jones, "New calculus for the treatment of optical systems," *Journal of the Optical Society of America*, vol. 31, pp. 488–493, 1941.

[43] ——, "A new calculus for the treatment of optical systems II: Proof of three general equivalence theorems," *Journal of the Optical Society of America*, vol. 31, pp. 493–, 1941.

[44] ——, "New calculus for the treatment of optical systems VIII: Electromagnetic theory," *Journal of the Optical Society of America*, vol. 46, pp. 126–, 1956.

[45] M. C. Jackson, "The geometry of bistatic radar systems," *IEE Proceedings, Part F*, vol. 133, pp. 604–612, Dec. 1986.

[46] "DoD world geodetic system 1984: Its definition and relationships with local geodetic systems," National Geospatial-Intelligence Agency, Tech. Rep. TR8350.2, Jun. 2004.

[47] V. S. Chernyak, *Fundamentals of Multisite Radar Systems*. Gordon and Breach Scientific Publishers, 1998.

[48] N. J. Willis, "Bistatic radar," in *Radar Handbook*, 2nd ed., M. I. Skolnik, Ed. McGraw-Hill, 1990, ch. 25.

[49] *ISO 31-5: Quantities and units: Electricity and Magnetism*. International Organization for Standardization, 1992.

[50] D. Barton, *Modern Radar System Analysis*. Artech House, Inc, 1988.

[51] M. I. Skolnik, *Introduction to Radar Systems*, 2nd ed. McGraw-Hill, 2001.

[52] P. Swerling, "Detection of fluctuating pulsed signals in the presence of noise," *Transactions of the IRE*, vol. IT-3, pp. 175–178, 1957.

[53] J. I. Marcum and P. Swerling, "Studies of target detection by pulsed radar," *IRE Transactions on Information Theory*, vol. IT-6, p. 2, Apr. 1960.

[54] P. Swerling, "Probability of detection for fluctuating targets," *IEEE Transactions on Information Theory*, vol. 6, no. 2, pp. 269–308, Apr. 1960.

[55] S. L. Johnston, "Target fluctuation models for radar system design and performance analysis: An overview of three papers," *IEEE Transactions on Aerospace and Electronic Systems*, vol. 33, no. 2, pp. 696–670, Apr. 1997.

[56] ——, "Target model pitfalls (illness, diagnosis and prescription)," *IEEE Transactions on Aerospace and Electronic Systems*, vol. 33, no. 2, pp. 715–720, Apr. 1997.

[57] P. Swerling, "Radar probability of detection for some additional fluctuating target cases," *IEEE Transactions on Aerospace and Electronic Systems*, vol. 33, no. 2, pp. 698–709, Apr. 1997.

[58] W. W. Weinstock, "Target cross section models for radar systems analysis," Ph.D. dissertation, University of Pennsylvania, 1956.

[59] D. A. Shnidman, "Expanded Swerling target models," *IEEE Transactions on Aerospace and Electronic Systems*, vol. 39, no. 3, pp. 1059–1069, Jul. 2003.

[60] P. Z. Peebles, *Probability, Random Variables and Random Signal Principles*, 4th ed. McGraw Hill, 2001.

[61] M. Abramowitz and I. A. Stegun, *The Handbook of Mathematical Functions*. Dover Publications, 1965.

[62] W. H. Press, S. A. Teukolsky, W. T. Vetterling, and B. P. Flannery, *Numerical Recipes in C: The Art of Scientific Computing*. Cambridge University Press, 1992.

[63] J. K. Jao and M. Elbaum, "First-order statistics of a non-Rayleigh fading singal and its detection," *Proceedings of the IEEE*, vol. 66, pp. 781–789, Jul. 1978.

[64] G. R. Heidbreder and R. L. Mitchell, "Detection probabilies for log-normally distributed signals," *IEEE Transactions on Aerospace and Electronic Systems*, vol. 3, pp. 5–13, Jan. 1967.

[65] G. E. Pollon, "Statistical parameters for scattering from randomly orientated arrays," *IEEE Transactions on Antennas and Propagation*, vol. 18, pp. 68–75, Jan. 1970.

[66] J. D. Wilson, "Probability of detecting aircraft targets," *IEEE Transactions on Aerospace Electronic Systems*, vol. 8, pp. 757–761, 1972.

[67] P. E. Hudson, "Passive multistatic radars in anti-stealth air defence," Master's thesis, Canadian Forces College, 2003. [Online]. Available: http://wps.cfc.forces.gc.ca/papers/csc/csc29/mds/hudson.pdf

[68] E. F. Knott, J. F. Shaeffer, and M. T. Tuley, *Radar Cross Section*, 2nd ed. Artech House, 1993.

[69] J. I. Glaser, "Some results in the bistatic radar cross section (RCS) of complex objects," *Proceedings of the IEEE*, vol. 77, no. 5, pp. 639–648, May 1989.

[70] R. E. Kell, "On the derivation of bistatic RCS from monostatic measurements," *Proceedings of the IEEE*, vol. 53, no. 8, pp. 983–987, Aug. 1965.

[71] M. W. Long, *Radar Reflectivity of Land and Sea*, 2nd ed. Artech House, Inc., 1983.

[72] J. H. Huynen, "Phenomenological theory of radar targets," in *Electromagnetic Scattering*, L. E. Uslenghi, Ed. Academic Press, New York, 1978.

[73] I. M. Yaglom, *Geometric Transformations I.* Random House, 1962.

[74] P. J. Mohr and B. N. Taylor, "CODATA recommended values of the fundamental physical constants: 2002," *Reviews of Modern Physics*, vol. 77, pp. 1–107, 2005.

[75] S. R. Doughty, "Development and performance evaluation of a multistatic radar system," Ph.D. dissertation, University College London, Jul. 2008.

[76] T. E. Derham, S. Doughty, K. Woodbridge, and C. J. Baker, "Design and evaluation of a low-cost multistatic netted radar system," *IET Radar, Sonar and Navigation*, vol. 1, no. 5, pp. 362–368, Oct. 2007.

[77] S. Doughty, K. Woodbridge, and C. Baker, "Characterisation of a multistatic radar system," in *Radar Conference, 2006. 3rd European*, 2006.

[78] S. R. Doughty, "Multistatic radar measurements and development," Master's thesis, University College London, Dec. 2005.

[79] Y. Paichard, J. Castelli, P. Dreuillet, and G. Bobillot, "HYCAM: A RCS measurement and analysis system for time-varying targets," in *Instrumentation and Measurement Technology Conference, 2006. IMTC 2006. Proceedings of the IEEE*, Apr. 2006.

[80] R. Buderi, *The invention that changed the world: the story of radar from war to peace.* Simon & Schuster, 1996.

[81] G. Brooker, "Long-range imaging radar for autonomous navigation," Ph.D. dissertation, University of Sydney, 2005.

[82] A. Celliers, "The design of a 94GHz high resolution coherent radar," Ph.D. dissertation, University of Cape Town, 1987.

[83] P. Horowitz and W. Hill, *The Art of Electronics*. Cambridge University Press, 1989.

[84] R. S. Raven, "Requirements on master oscillators for coherent radar," *Proceedings of the IEEE*, vol. 54, pp. 237–243, 1966.

[85] J. C. Kirk, "Bistatic SAR motion compensation," in *IEEE International Radar Conference*, 1985.

[86] C. J. Baker and A. L. Hume, "Netted radar sensing," *IEEE aerosp. electron. syst. mag.*, vol. 18, no. 2, pp. 3–6, Feb. 2003.

[87] A. L. Hume and C. J. Baker, "Netted radar sensing," in *Proceedings of the 2001 IEEE Radar Conference*, May 2001.

[88] E. J. Baghdady, R. N. Lincoln, and B. D. Nelin, "Short-term frequency stability: Characterization, theory and measurement," *Proceedings of the IEEE*, vol. 53, pp. 704–722, 1965.

[89] J. A. Barnes, A. R. Chi, L. S. Cutler, D. J. Healey, D. B. Leeson, T. E. McGunigal, J. A. Mullen, W. L. Smith, and R. L. Sydnor, "Characterization of frequency stability," National Bureau of Standards, Technical Note 394, Oct. 1970.

[90] ——, "Characterization of frequency stability," *IEEE Transactions on Instrumentation and Measurement*, vol. IM-20, pp. 105–120, May 1971.

[91] T. Walter, "Characterizing frequency stability: A continuous power-law model with discrete sampling," *IEEE Transactions on Instrumentation and Measurement*, vol. 43, no. 1, pp. 69–79, Feb. 1994.

[92] D. W. Allan, "Time and frequency (time-domain) characterization, estimation and prediction of precision clocks and oscillators," *IEEE Transactions on Ultrasonics, Ferroelectrics and Frequency Control*, vol. UFFC-34, no. 6, pp. 647–654, Nov. 1987.

[93] W. Davenport and W. Root, *Random Signals and Noise*. McGraw-Hill, 1958.

[94] L. S. Cutler and C. L. Searle, "Some aspects of the theory and measurement of frequency fluctuations in frequency standards," *Proceedings of the IEEE*, vol. 54, pp. 135–154, Feb. 1966.

[95] J. A. Barnes, "Atomic timekeeping and statistics of precision signal generators," *Proceedings of the IEEE*, vol. 54, pp. 207–220, Feb. 1966.

[96] *IEEE Std 1139-1999: IEEE standard definitions of physical quantities for fundamental frequency and time metrology - random instabilities*. The Institute of Electrical and Electronics Engineers, Inc., 1999.

[97] G. W. Ewell, "Stability and stable sources," in *Coherent Radar Performance Estimation*, J. A. Scheer and J. L. Kurtz, Eds. Artech House, 1993, ch. 2.

[98] *HF Ultra Low Noise OCXO*, Wenzel Associates, Inc., 2006.

[99] J. Bendat and A. Piersol, *Random Data: Analysis and Measurement Procedures*. Wiley-Interscience, 1986.

[100] G. Samorodnitsky, "Long range dependence," in *Encyclopedia of Actuarial Science*, J. L. Teugels and B. Sundt, Eds. John Wiley & Sons, Ltd., 2004, vol. 2, pp. 1033–1036.

[101] G. Lindgren, "Stationary processes," in *Encyclopedia of Actuarial Science*, J. L. Teugels and B. Sundt, Eds. John Wiley & Sons, Ltd., 2004, vol. 3, pp. 1589–1593.

[102] D. Howe, D. Allan, and J. Barnes, "Properties of signal sources and measurement methods," in *Thirty Fifth Annual Frequency Control Symposium*, 1981, pp. 669–716.

[103] J. A. Barnes, R. H. Jones, P. V. Tryon, and D. W. Allan, "Stochastic models for atomic clocks," in *NASA. Goddard Space Flight Center*

Proc. of the 14th Ann. Precise Time and Time Interval (PTTI) Appl. Planning Meeting, Feb. 1983.

[104] D. W. Allan and J. A. Barnes, "A modified 'Allan variance' with increased oscillator characterization ability," in *Thirty Fifth Annual Frequency Control Symposium*, 1981, pp. 470–475.

[105] D. A. Howe, "The total deviation approach to long-term characterization of frequency stability," *IEEE Transactions on Ultrasonics, Ferroelectrics, and Frequency Control*, vol. 47, pp. 1102–1109, 2000.

[106] C. A. Greenhall, D. A. Howe, and D. B. Percival, "Total variance, an estimator of long-term frequency stability," *IEEE Transactions on Ultrasonics, Ferroelectrics, and Frequency Control*, vol. 46, no. 5, pp. 1183–1191, Sep. 1999.

[107] C. A. Greenhall, "Spectral ambiguity of Allan variance," *IEEE Transactions on Instrumentation and Measurement*, vol. 47, no. 3, pp. 623–627, Jun. 1998.

[108] ITU-T, "Definitions and terminology for synchronization networks," International Telecommunication Union, Standard G.810, Aug. 1996.

[109] N. Roberts, "Phase noise and jitter — a primer for digital designers," Zarlink Semiconductor, Tech. Rep., 2003.

[110] W. Kester, "Converting oscillator phase noise to time jitter," Analog Devices, Application Note MT-008, 2005.

[111] A. Einstein, "Method for the determinination of the statistical values of observations concerning quantities subject to irregular fluctuations," *IEEE ASSP Magazine*, vol. 4, no. 4, p. 6, Oct. 1987.

[112] C. A. Greenhall, "FFT-based methods for simulating flicker FM," in *34th Annual Precise Time and Time Interval (PTTI) Meeting*, Dec. 2002, pp. 481–491.

[113] N. J. Kasdin, "Discrete simulation of colored noise and stochastic processes and 1/f power law noise generation," *Proceedings of the IEEE*, vol. 83, no. 5, pp. 802–827, May 1995.

[114] E. Milotti, "Exact numerical simulation of power-law noises," *Physical Review E*, vol. 72, no. 5, p. 056701, 2005.

[115] S. Plaszczynski, "Generating long streams of $1/f^{\alpha}$ noise," *Fluctuation and Noise Letters*, vol. 7, no. 1, pp. R1–R13, 2007.

[116] J. Nagler and J. Claussen, "$1/f^{a}$ spectra in elementry cellular automata and fractal signals," *Physical Review E*, vol. 71, p. 067103, 2005.

[117] J. C. Claussen, J. Nagler, and H. G. Schuster, "Sierpinski signal generates $1/f^{\alpha}$ spectra," *Physical Review E*, vol. 70, pp. 032 101–1, 2004.

[118] Y. Meyer, F. Sellan, and M. S. Taqqu, "Wavelets, generalized white noise and fractional integration: The synthesis of fractional brownian motion," *The Journal of Fourier Analysis and Applications*, vol. 5, no. 5, pp. 465–494, 1999.

[119] E. J. McCoy and A. T. Walden, "Wavelet analysis and synthesis of stationary long-memory processes," *Journal of Computational and Graphical Statistics*, vol. 5, no. 1, pp. 26–56, Mar. 1996.

[120] P. Flandrin, "Wavelet analysis and synthesis of fractional Brownian motion," *IEEE Transactions on Information Theory*, vol. 38, no. 2, pp. 910–917, Mar. 1992.

[121] J. R. M. Hosking, "Fractional differencing," *Biometrika*, vol. 68, no. 1, pp. 165–176, Apr. 1981.

[122] R. Whittle, "DSP generation of pink noise," http://www.firstpr.com.au/dsp/pink-noise/, Tech. Rep., 2007.

[123] B. Friedlander and B. Porat, "The modified Yule-Walker method of ARMA spectral estimation," *IEEE Transactions on Aerospace and Electronic Systems*, vol. AES-20, no. 2, pp. 158–173, Mar. 1984.

[124] I. W. Selesnick, M. Lang, and C. S. Burrus, "Magnitude squared design of recursive filters with the chebyshevnorm using a constrained rational Remez algorithm," in *Sixth IEEE Digital Signal Processing Workshop*, 1994.

[125] A. Rodriguez and S. G. Johnson, "Efficient generation of correlated random numbers using chebyshev-optimal magnitude-only IIR filters," Mar. 2007, eprint arXiv:physics/0703152.

[126] P. Thajchayapong and P. Rayner, "Recursive digital filter design by linear programming," *IEEE Transactions on Audio and Electroacoustics*, vol. 21, no. 2, pp. 107–112, Apr. 1973.

[127] L. R. Rabiner, N. Y. Graham, and H. D. Helms, "Linear programming design of IIR digital filters with arbitrary magnitude function," *IEEE Transactions on Acoustics, Speech, And Signal Processing*, vol. 22, no. 2, pp. 117–123, Apr. 1974.

[128] D. E. Dudgeon, "Recursive filter design using differential correction," *IEEE Transactions on Acoustics, Speech, and Signal Processing*, vol. 22, no. 6, pp. 443–448, Dec. 1974.

[129] I. Barrodale, M. Powell, and F. Roberts, "The differential correction algorithm for rational l_∞ approximation," *SIAM Journal of Numerical Analysis*, vol. 9, pp. 493–504, 1972.

[130] X. Zhang, K. Suzuki, and T. Yoshikawa, "Complex chebyshev approximation for IIR digital filters based on eigenvalue problem," *IEEE Transactions on Circuits and Systems II*, vol. 47, no. 12, pp. 1429–1436, Dec. 2000.

[131] X. Zhang and H. Iwakura, "Design of IIR digital filters based on eigenvalue problem," *IEEE Transactions on Signal Processing*, vol. 44, no. 6, pp. 1325–1333, Jun. 1996.

[132] P. P. Vaidyanathan, *Multirate Systems and Filter Banks*. Prentice Hall, 1992.

[133] R. Crochiere and L. Rabiner, *Multirate Digital Signal Processing*. Prentice-Hall, 1983.

[134] R. W. Hamming, *Digital Filters*, 3rd ed. Dover Publications, Inc., 1999.

[135] T. W. Parks and C. S. Burrus, *Digital Filter Design*. Wiley, New York, 1987.

[136] M. A. Lombardi, "Fundamentals of time and frequency," in *The Mechatronics Handbook*, R. H. Bishop, Ed. CRC Press, 2002, ch. 17.

[137] W. J. Riley and C. A. Greenhall, "Power law noise identification using the lag 1 autocorrelation," in *18th European Frequency and Time Forum*, 2004.

[138] R. T. Austin, A. W. England, and G. H. Wakefield, "Special problems in the estimation of power-law spectra as applied to topographical modeling," *IEEE Transactions on Geoscience and Remote Sensing*, vol. 32, no. 4, pp. 928–939, Jul. 1994.

[139] J. Capon, "High-resolution frequency-wavenumber spectrum analysis," *Proceedings of the IEEE*, vol. 57, pp. 1408–1418, 1969.

[140] P. D. Welch, "The use of the fast Fourier transform for the estimation of power spectra: A method base on time averaging over short, modified periodograms," *IEEE Transactions on Audio and Electroacoustics*, vol. AU-15, pp. 70–73, Jun. 1967.

[141] S. M. Kay, *Modern Spectral Estimation*. Prentice Hall, 1988.

[142] B. B. Mandelbrot and J. W. V. Ness, "Fractional brownian motions, fractional noises and applications," *SIAM Review*, vol. 10, no. 4, pp. 422–436, Oct. 1968.

[143] J. Weidendorfer, M. Kowarschik, and C. Trinitis, "A tool suite for simulation based analysis of memory access behavior," in *Proceedings*

of the 4th International Conference on Computational Science (ICCS 2004), Jun. 2004.

[144] W. V. Shrader and V. Gregers-Hansen, "MTI radar," in *Radar Handbook*, 2nd ed., M. I. Skolnik, Ed. McGraw-Hill, 1990, ch. 15.

[145] R. R. Kerr, "MTI systems," in *Coherent Radar Performance Estimation*, J. A. Scheer and J. L. Kurtz, Eds. Artech House, 1993, ch. 8.

[146] J. A. Scheer, "Introduction to coherent radar systems," in *Coherent Radar Performance Estimation*, J. A. Scheer and J. L. Kurtz, Eds. Artech House, 1993, ch. 1.

[147] J. A. Scheer and J. L. Kurtz, Eds., *Coherent Radar Performance Estimation*. Artech House, 1993.

[148] F. G. Stremler, *Introduction to Communication Systems*, 3rd ed. Addison Wesley, 1992.

[149] M. L. Belcher and G. V. Morris, "Pulsed doppler radar," in *Coherent Radar Performance Estimation*, J. A. Scheer and J. L. Kurtz, Eds. Artech House, 1993, ch. 9.

[150] J. Steensgaard-Madsen, "High-performance data converters," Ph.D. dissertation, The Technical University of Denmark, 1999.

[151] P. Smith, "Little known characteristics of phase noise," Analog Devices, Application Note AN-741, 2004.

[152] GNU, "The GNU General Public Licence," http://www.gnu.org/licenses/gpl.html, June 1991.

[153] G. van Rossum, *Python Reference Manual*, 2nd ed., Python Software Foundation, http://docs.python.org/ref/ref.html, Feb. 2008.

[154] B. Stroustrup, *The C++ Programming Language*, 3rd ed. Addison-Wesley, 1997.

[155] S. Meyers, *Effective C++*, 3rd ed. Addison-Wesley, 2005.

[156] "Boost C++ libraries," http://www.boost.org/.

[157] "The computer language benchmarks game," http://shootout.alioth.debian.org/, accessed March 2008.

[158] "Tiobe programming community index for March 2008," TIOBE Software, http://www.tiobe.com/index.php/content/paperinfo/tpci/index.html, Tech. Rep., Mar. 2008, accessed March 2008.

[159] H. E. Hinnant, B. Dawes, L. Crowl, J. Garland, and A. Williams, "Multi-threading library for standard C++," ISO JTC1/SC22/WG21 - The C++ Standards Committee, http://www.open-std.org/jtc1/sc22/wg21/docs/papers/2007/n2320.html, Tech. Rep. N2320, Jun. 2007.

[160] N. M. Josuttis, *The C++ Standard Library: A Tutorial and Reference*. Addison-Wesley, 1999.

[161] S. Meyers, *Effective STL*. Addison-Wesley, 2001.

[162] *SD15 2.4GHz Parabolic antenna*, Stella Doradus Ireland Ltd., data Sheet.

[163] E. Dijkstra, "Over sienpalen (EWD 74) (Dutch)," http://www.cs.utexas.edu/users/EWD/ewd00xx/EWD74.PDF.

[164] A. B. Downey, *The Little Book of Semaphores*. Green Tea Press, 2008.

[165] N. Nethercote and J. Seward, "Valgrind: A framework for heavyweight dynamic binary instrumentation," in *Proceedings of ACM SIGPLAN 2007 Conference on Programming Language Design and Implementation*, Jun. 2007.

[166] N. Nethercote, "Dynamic binary analysis and instrumentation," Ph.D. dissertation, University of Cambridge, Nov. 2004.

[167] A. S. Tanenbaum, *Structured Computer Organization*, 4th ed. Prentice Hall, 1999.

[168] A. H. Karp and H. P. Flatt, "Measuring parallel processor performance," *Communications of the ACM*, vol. 33, no. 5, pp. 539–543, May 1990.

[169] J. Dean and S. Ghemawat, "Mapreduce: Simplified data processing on large clusters," in *OSDI'04: Sixth Symposium on Operating System Design and Implementation,*, 2004, pp. 137–150.

[170] G. E. Révész, *Lambda Calculus, Combinators, and Functional Programming*. Cambridge University Press, 1988.

[171] G. Michaelson, *An Introduction to Functional Programming through Lambda Calculus*. Addison-Wesley, 1989.

[172] J. Dean and S. Ghemawat, "Mapreduce: Simplified data processing on large clusters," *Communications of the ACM*, vol. 51, no. 1, pp. 107–113, Jan. 2008.

[173] C. Ranger, R. Raghuraman, A. Penmetsa, G. Bradski, and C. Kozyrakis, "Evaluating mapreduce for multi-core and multiprocessor systems," in *High Performance Computer Architecture, 2007. HPCA 2007. IEEE 13th International Symposium on*, 2007, pp. 13–24.

[174] M. D. Linderman, J. D. Collins, H. Wang, and T. H. Meng, "Merge: a programming model for heterogeneous multi-core systems," in *Proceedings of the 13th international conference on Architectural support for programming languages and operating systems*, 2008, pp. 287–296.

[175] T. I. Laakso, V. Vlimki, M. Karjalainen, and U. K. Laine, "Splitting the unit delay - tools for fractional delay filter design," *IEEE Signal Processing Magazine*, vol. 13, no. 1, pp. 30–60, Jan. 1996.

[176] V. Valimaki and T. I. Laakso, "Fractional delay filters — design and applications," in *Theory and Applications of Nonuniform Sampling*, F. Marvasti, Ed. Kluwer, 2000.

[177] L. R. Rabiner and B. Gold, *Theory and Application of Digital Signal Processing*. Prentice-Hall, 1975.

[178] V. Valimaki and T. I. Laakso, "Principles of fractional delay filters," in *IEEE International Conference on Acoustics, Speech and Signal Processing*. IEEE, Jun. 2000.

[179] A. Yardim, G. Cain, and P. Henry, "Optimal two-term offset windowing for fractional delay," *Electronics Letters*, vol. 32, no. 6, pp. 526–527, Mar. 1996.

[180] G. Cain, A. Yardim, and P. Henry, "New FIR fractional delayors for effective signal interpolation," in *Proc. DSP'94 ESA Workshop on DSP for Space Applications*, Sep. 1994, pp. 42–49.

[181] ——, "Offset windowing for FIR fractional-sample delay," in *Proc. ICASSP'95*, May 1995, pp. 1276–1279.

[182] J. O. Smith and P. Gossett, "A flexible sampling-rate conversion method," in *Proceedings of the International Conference on Acoustics, Speech, and Signal Processing*, vol. 2, Mar. 1984, pp. 19.4.1–19.4.2.

[183] J. O. Smith, *Digital Audio Resampling Home Page*. http://www-ccrma.stanford.edu/~jos/resample/, Jan. 2002.

[184] J. F. Kaiser, "Using the I_0 sinh window function," *IEEE Transactions on Circuits and Systems*, vol. 22, pp. 20–23, 1974.

[185] J. Kaiser and R. Schafer, "On the use of the i_0-sinh window for spectrum analysis," *IEEE Transactions on Acoustics, Speech, and Signal Processing*, vol. 28, no. 1, pp. 105–107, Feb. 1980.

[186] J. F. Kaiser, "Digital filters," in *System Analysis by Digital Computer*, F. F. Kuo and J. F. Kaiser, Eds. Wiley, 1966, pp. 218–285.

[187] D. Slepian, H. O. Pollack, and H. J. Landau, "Prolate spheroidal wave functions, Fourier analysis and uncertainty," *Bell Systems Technical Journal*, vol. 40, pp. 43–63, Jan. 1961.

[188] C. W. Farrow, "A continuously variable digital delay element," in *Circuits and Systems, 1988., IEEE International Symposium on*, vol. 3, Jun. 1988, pp. 2641–2645.

[189] J. Radatz, Ed., *IEEE Standard dictionary of electrical and electronics terms*, 6th ed. Institute of Electrical and Electronics Engineers, 1997.

[190] L. J. Cutrona, "Synthetic aperture radar," in *Radar Handbook*, 2nd ed., M. I. Skolnik, Ed. McGraw-Hill, 1990, ch. 15.

[191] J. C. Curlander and R. N. McDonough, *Synthetic Aperture Radar: Systems and Signal Processing*. Wiley, 1991.

[192] M. R. Inggs, "First results from the South African VHF imaging radar," in *Proceedings of the 3rd IMACS/IEEEE International Multiconference on Circuits, Systems, Communications and Computers*, Jul. 1999.

[193] M. R. Inggs, J. M. Horrell, A. Knight, and P. G. Koeppen, "iSAR: A multispectral polarimetric airborne SAR system," in *Proceedings of the 1994 Internation Geoscience and Remote Sensing Symposium*, vol. 4, Aug. 1994, pp. 2237–2239.

[194] R. T. Lord, "Aspects of stepped-frequency processing for low-frequency SAR systems," Ph.D. dissertation, University of Cape Town, Feb. 2000.

[195] H. D. Griffiths and C. J. Baker, "Passive coherent location radar systems. part 1: Performance prediction," *IEE Proceedings on Radar, Sonar and Navigation*, vol. 152, pp. 153–159, 2005.

[196] P. E. Howland, D. Maksimiuk, and G. Reitsma, "Fm radio based bistatic radar," *IEEE Proceedings on Radar, Sonar and Navigation*, vol. 152, pp. 107–115, 2005.

[197] J. Baniak, G. Baker, A. Cunningham, and L. Martin, "Silent sentry passive surveillance," *Aviation week and space technology*, Jun. 1999.

[198] Z. Jiabing, T. Liang, and H. Yi, "Adaptive beamforming passive radar based on fm radio transmitter," in *CIE '06 International Conference on Radar*, Oct. 2006, pp. 1–4.

[199] J. D. Sahr and F. D. Lind, "The manastash ridge radar: A passive bistatic radar for upper atmospheric radio science," *Radio Science*, vol. 32, no. 6, pp. 2345–2358, 1997.

[200] P. E. Howland, "Target tracking using television-based bistatic radar," *IEE Proceedings on Radar, Sonar and Navigation*, vol. 146, no. 3, pp. 166–174, 1999.

[201] H. D. Griffiths and N. R. Long, "Television-based bistatic radar," *IEE Proceedings, Part F*, vol. 133, no. 7, pp. 649–657, Dec. 1986.

[202] H. Sun, D. K. P. Tan, and Y. Lu, "Design and implementation of an experimental gsm based passive radar," in *Proceedings of the IEEE International Radar Conference*, 2003, pp. 418–422.

[203] H. D. Griffiths, C. J. Baker, J. Baubert, N. Kitchen, and M. Treagust, "Bistatic radar using satellite-borne illuminators," in *Proceedings of the IEEE International Radar Conference*, 2002.

[204] C. J. Baker, H. D. Griffiths, and I. Papoutsis, "Passive coherent location radar systems. part 2: Waveform properties," *IEE Proceedings on Radar, Sonar and Navigation*, vol. 152, no. 3, pp. 160–168, Jun. 2005.

[205] T. Derham, S. Doughty, K. Woodbridge, and C. Baker, "Realisation and evaluation of a low cost netted radar system," in *Radar, 2006. CIE '06. International Conference on*, 2006.

[206] *Piezotite Ultrasonic Sensor MA Series*, muRata.

[207] J. B. Allen and L. R. Rabiner, "A unified approach to short-time Fourier analysis and synthesis," *Proceedings of the IEEE*, vol. 65, pp. 1558–1564, Nov. 1977.

[208] W. L. Patterson, "Advanced refractive effects prediction system (AREPS)," in *Radar Conference, 2007 IEEE*, 2007.

[209] ——, "Advanced refractive effects prediction system (AREPS)," Space and Naval Warfare Systems Center, San Diego, Research paper A242434, Aug. 2001.

[210] P. Dutre, K. Bala, and P. Bekaert, *Advanced Global Illumination*. A K Peters Ltd., 2006.

[211] M. Pharr and G. Humphreys, *Physically Based Rendering : From Theory to Implementation*. Morgan Kaufmann, 2004.

[212] U. Jakobus, *User's Guide To FEKO*, EM Software & Systems-SA (Pty) Ltd.

[213] C. A. Greene and R. T. Moller, "The effect of normally distributed random phase errors on synthetic array gain patterns," *IRE Transactions*, vol. MIL-6, pp. 119–121, Apr. 1962.

[214] D. L. Evans, T. G. Farr, J. P. Ford, T. W. Thompson, and C. L. Werner, "Multipolarization radar images for geologic mapping and vegetation discrimination," *IEEE Transactions on Geoscience and Remote Sensing*, vol. GE-24, no. 2, pp. 246–257, Mar. 1986.